CHARACTERIZING LOW ENERGY ELECTRON-INDUCED REACTIONS WITH THIN FILMS, ADSORBATES, AND GAS PHASE MOLECULES

by
Michael Barclay

A dissertation submitted to Johns Hopkins University in conformity with the requirements for the degree of Doctor of Philosophy

Baltimore, MD
January 2019

Abstract

Low energy electrons play an important role in the creation and modification of nanoscale thin films. The ability to characterize the lateral effects of these reactions is a necessary technique in the nanoscale fields of tribology and lithography. Of particular interest is the ability to discern the difference between sp^2 and sp^3-hybridized carbon. In nanoscale thin films, differences in the ratios between these two allotropes has been shown to drastically change the physical properties of the films they inhabit. However, due to their similarities, both allotropes can be somewhat difficult to distinguish, especially in nanoscale thin films. To this end, low energy electrons were used to deposit and modify sp^3-like carbon into a more graphitic sp^2-like carbon species. X-ray photoelectron spectroscopy (XPS) and Spectroscopic Ellipsometry (SE), were then used to interrogate and spatially map the resulting changes. The electron-induced transformations produced measurable changes to the C 1s peak profiles (XPS) and the dielectric functions (SE) of the carbon films. The films were then successfully characterized as a function of electron dose using (i), a linear combination of the individual components obtained in XPS, and (ii), a Bruggeman effective medium approximation of the SE film response for both types of carbon species. Both techniques were able to show similar results regarding both lateral film composition and thickness. Further changes to the films' dimensions and structure were induced using atomic hydrogen etching. Both characterization techniques were able to track the conversion of sp^2-like carbon back into sp^3-like carbon species in addition to providing etching rates for the films.

The holy grail of nanoscale film fabrication is the ability to control the chemical composition of the resulting film. While low energy electrons have been shown to induce a variety of reactions, dissociation of a molecule through electron attachment (DEA) is of considerable interest. The resonant nature of the electron attachment process allows for DEA to have high cross

sections and be bond specific. This opens a wide range of possibilities regarding the control of nanoscale thin films. To this end, the efficacy of this approach was studied with regard to carbon nanomembrane fabrication. Due to biphenyl's success as a CNM precursor, 2-iodobiphenyl (2-I-BPh), 2-bromobiphenyl (2-Br-BPh), and 2-chlorobiphenyl (2-Cl-BPh) were subjected to gas phase studies to probe their sensitivity to DEA interactions. High DEA cross sections were observed at 0 eV for 2-I-BPh as compared to the other halogenated biphenyl compounds. The efficacy of these findings was then tested by monitoring the effects of electrons on thiolated versions of these compounds. The results showed that the iodized compound formed cross-linkages at a faster rate than the other halogenated species and non-halogenated biphenyl thiol control. Further gas phase studies on 2-I-BPh, 2-Br-BPh, and 2-Cl-BPh focused on the DI pathways of all three molecules. These results showed that all three molecules showed similar fragmentation patterns. The appearance energies of the dominant fragments were identified from the ion-yields of all three compounds. By comparing hessian thermochemical calculations to the observed appearance energies of these dominant fragments, several DI fragmentation pathways were identified and shown to be consistent for all three compounds.

Lastly, electron beam induced deposition is a fabrication technique capable of creating complex three-dimensional nano-structures through the decomposition and deposition of transiently adsorbed precursors. In general, the composition of these resulting structures is strongly dependent on the precursors used in the deposition process. As a result, understanding the kinetics behind this process is essential to designing an ideal precursor. To this end the effects of 500 eV electrons on several iron carbonyl precursors ($Fe(CO)_5$, $Fe_2(CO)_9$, and $Fe_3(CO)_{12}$) were studied. In general, their results showed that the electron induced deposition of these species is a two-step mechanism that begins with the creation of a partially decarbonylated species through CO emission

and ends with the electron stimulated decomposition of the remaining CO species to produce a metal (in this case iron) oxide and graphitic carbon. A kinetic model was fit to data obtained for $Fe(CO)_5$ showing that the production of partially decarbonylated iron species proceeds at a much faster rate than the electron decomposition, $k_1 = 0.004147\ s^{-1}$ and $k_2 = 0.000068\ s^{-1}$ respectively. Comparing the different iron carbonyl species showed that while the rates of decomposition are precursor dependent (about an order of magnitude faster for $Fe_2(CO)_9$ and $Fe_3(CO)_{12}$), the overall CO loss is effectively similar for all three compounds. Annealing experiments, performed on $Fe(CO)_5$ and $Fe_3(CO)_{12}$ showed that the partially decarbonylated species of both compounds were particularly sensitive to thermal reactions at room temperature. The implications of these results for EBID conditions were postulated, indicating that the susceptibility of partially decarbonylated species to thermal reactions at room temperature is suspected to allow the creation of high purity deposits in situations where the electron dose is sufficiently small.

Advisor: D. Howard Fairbrother

Preface

I would first like to thank my advisor, Prof. Howard Fairbrother for his guidance and leadership. He has helped me hone my skills and turn me into the scientist that I am today. I would like to thank Dr. Shannon Hill who taught me the value of data analysis and made me the programmer I am today. I would like to thank Oddur Ingólfsson for his hospitality and guidance. I would also like to thank Boris Steinberg for always having the right tool for the right job. I would especially like to thank Dr. Kevin Wepasnick who has served as a friend and mentor. His insults have kept me grounded and our long scientific debates have been invaluable.

I would also like to thank the past and current Fairbrother group members for their time and help in various forms: Dr. Justin Gorham, Dr. David Goodwin, Dr. Samantha Rosenberg, Dr. Julie Bitter, Dr. Miranda Gallagher, Dr. Ronald Lankone, Dr. Rachel Thorman, Dr. Julie Spencer, Dr. Dave Durkin and Benjamin Frank

I would like to thank my friends and family for their support, and patience. I would lastly like to thank, Helen Nieman for putting up with a poor, scruffy-looking, graduate student.

Table of Contents

List of Tables

List of Figures

Chapter 1

Characterizing Changes in Thin Films Due to Interactions with Low Energy Electrons in a Vacuum

1. 1. Introduction

The interaction between high-energy radiation (e.g., γ-rays, x-rays, UV-photons, electrons, and ion beams) and matter is known to produce large numbers of low-energy electrons[1]. In general, the energy distribution of these secondary electrons is such that most typically have energies below 10 eV. Inelastic collisions between these electrons and atoms / molecules have been shown to produce energetic species which stimulate a wide number of radiation-induced chemical reactions[2-8]. Low energy electrons have been shown to contribute to DNA damage through the "direct effect"[9]. Studies of these low energy electron have shown that they have applications that go beyond radiation chemistry, impacting the fields of environmental science, astrochemistry, tribology, biology, lithography, and much more[10-14].

While these electrons and their effects are ubiquitous, one of the more promising avenues for low electron study has to do with their use in nanofabrication and the production of ultra-thin films. Focused electron beams have been shown to decompose transiently adsorbed precursor molecules into nanosized structures through a process known as electron beam induced deposition (EBID)[15]. Due to the high interaction cross section of electrons, a vast library of precursor molecules can be utilized, varying the chemical composition of these films and allowing for numerous potential applications[15]. Low energy electrons have been shown to induce cross-linking of specific aromatic self-assembled monolayers (SAMs) to produce carbon nanomembranes (CNMs)[14, 16-18]. These two-dimensional molecular sheets boast a high mechanical strength and thermal stability along with various other properties which can be tailored depending on the molecular composition and structure of the assembled molecular layers[19-21]. As such, these membranes have great potential for a wide variety of applications[20].

Both low energy electron CNM fabrication and EBID have shown a strong ability to control the physical dimensions of the material being produced. However, the holy grail in nanofabrication techniques is the ability to control composition as well as structure. While both techniques have shown a good deal of control in this arena, there are still limitations. For example, EBID structures often contain large amounts of organic contamination depending on the precursor used in the deposition process. The goal of this chapter is to illuminate the effects low energy electrons have on thin films, adsorbates, and gas phase molecules. The goal of this thesis, however, is to use this information to firstly provide methodologies with which these effects can be characterized and secondly probe ways to harness and control these effects improving upon the effectiveness of modern nanofabrication techniques.

1. 2. Electron Interactions: Bond Rupture and Fragmentation

In general, electronic interactions with molecules, especially surfaces, can be complex. For this reason, the effects of electron-induced bond rupture are often studied with respect to gas phase interactions. In theory, these electron-molecule interactions will be similar whether the molecule is in gas phase or adsorbed on a surface.

Electron-induced molecular dissociation can proceed through one of three initial steps: electron impact ionization; electron impact excitation; and electron attachment to form a transient negative ion (TNI)[6]. Depending on the initiation pathway, dissociation will result in either resonant scattering through electron attachment (ion yield curves will show a discreet maxima at specific energies) or direct, non-resonant scattering (ion yield curves will show a smoothly increasing curve after a threshold energy) through electron impact ionization or excitation[6]. A discussion of these processes is given below.

Electron Impact Ionization:

For a generic AB molecule, electron impact ionization is characterized by the following equation.

$$AB + e^- \rightarrow AB^{(‡)+} + 2e^- \quad (1.1)$$

In this case "(‡)" denotes a vibrationally and/or electronically excited molecule. This type of ionization occurs when an electron imparts enough of its energy (usually in the form of a collision) to a molecule. If the energy imparted is greater than the ionization energy of the molecule, at least one or more electrons will leave the molecule resulting in an excited state, ionized molecule. Typically this happens over the time scale of ~10^{-6} s[22]. This interval is too short for the nuclei to adjust to changes in electron state, making this a vertical ionization process and subject to the Frank-Condon principle. Relaxation for this ionized and excited state parent molecule most commonly occurs through fragmentation. This process is known as dissociative ionization (DI) and can be characterized accordingly.

$$AB^{(‡)+} \rightarrow A^{(‡)+} + B^{(‡)} \quad (1.2)$$

The total ionization cross section, and equivalently the total ion yield, will generally start above a thermochemical threshold value (the ionization potential of the molecule, usually between 7 – 15 eV) and smoothly increase with electron energy until it reaches a plateau or maximum (~70 – 100 eV). This is exemplified in the DI total ion yield curves in Figure 3.4. The thermochemical threshold (E_{th}) for the formation of positive ion fragments in DI can be written as the following equation where BDE(AB) is the bond dissociation energy of AB and IE(A) is the ionization energy of A.

$$E_{th}(A^+) = BDE(AB) + IE(A) \quad (1.3)$$

Practically speaking, for ion fragments produced through DI, the onset of the ion yield curve corresponds to the energy needed to ionize the corresponding molecular fragment[23]. This can make DI a particularly useful tool in approximating the ionization energy of various molecules and molecular fragments.

Electron Impact Excitation

Electron impact excitation occurs at incident electron energies above the excitation threshold (~6 eV for small organic molecules) and produces a neutral molecule in an excited state[6, 24]. Unlike photon excitation, electron excitation is a non-resonant process and occurs on the same short time scales as electron impact ionization[24]. The process, is summarized in the following equation.

$$AB + e^- \rightarrow AB^{(\ddagger)} + e^- \quad (1.4)$$

After excitation, three dominant channels exist for the excited neutral molecule. It can emit a photon and/or undergo non-radiative deactivation through interactions with neighboring molecules.

$$AB^{(\ddagger)} \rightarrow AB + Energy \quad (1.5)$$

The molecule can also dissociate into two neutral radicals, known as neutral dissociation (ND).

$$AB^{(\ddagger)} \rightarrow A^{(\ddagger)} + B^{(\ddagger)} \quad (1.6)$$

ND will only occur if the initial electronic excitation energy is greater than the bond dissociation of the molecule. In general, ND is active at low electron energies and is more efficient for larger molecules with high densities of excited states. Additionally, since no charged fragments

are produced in ND, it is often difficult to detect. The third relaxation pathway that exists is through dissociation to create an ion pair, known as dipolar dissociation (DD).

$AB^{(\ddagger)} \rightarrow A^{(\ddagger)+} + B^{(\ddagger)-}$ (1.7)

In general, DD proceeds similarly to ND except the coulombic interactions between the positively and negatively charged fragments must be overcome. Consequently, the thermochemical threshold for DD is higher than ND and can be expressed in the following equation, where EA corresponds to the electron affinity of the anionic fragment.

$E_{th}(A^+ + B^-) = BDE(AB) + IE(A) - EA(B)$ (1.8)

Electron Attachment

Electron attachment is a resonant process that occurs at low energy (below 15 eV) and can be described accordingly.

$AB + e^- \rightarrow AB^{(\ddagger)-}$ (1.9)

In general, this involves the temporary occupation of the lowest unoccupied molecular orbital (LUMO) by the incoming electron. This orbital is usually antibonding in nature, which will induce bond stress as the anionic molecule relaxes. TNI formation is considered resonant due to the restricted range of acceptable energies for the incoming electron. This restricted range is limited by the Frank-Condon principle and the transition probability (P_{trans}) is proportional to the Frank-Condon factor which is given by the overlap of the ground state wave function and the excited anionic state wave function[25, 26].

$(P_{trans}) \propto |\langle \psi^0 | \phi^* \rangle|^2$ (1.10)

While the range of acceptable energies for TNI formation is relatively small, the cross sections for this type of process are relatively high with respect to other electron interactions. This

is likely due to the resonant nature of the process. The ion yields / cross sections of this resonant process are exemplified in Figure 3.1. In general, upon electron capture, the TNI will relax its excited electronic state by transferring this energy to kinetic energy of its nuclei A and B. The stability of the TNI during this internuclear exchange will determine its eventual relaxation pathway. The three dominant pathways of relaxation are autodetachment (AD), dissociation (DEA), or stabilization through intramolecular vibrational energy redistribution (IVR). Autodetachment is the most prevalent relaxation pathway and occurs when the attached electron is re-emitted.

$AB^{(\ddagger)-} \rightarrow AB^{(\ddagger)} + e^{-}$ (1.11)

The AD electron has the option of scattering both elastically or inelastically. If it scatters inelastically, the energy, imparted to the molecular system, will result in a vibrational / electronic excited state. Measurement of the AD's energy using electron energy loss spectroscopy (EELS) can provide information about a molecule's electronic states and vibrational modes. AD occurs when the lifetime of TNI is short (less than the vibrational period of the nuclei, ~10^{-14} s) and can happen at any point until the potential energy surfaces cross at the critical internuclear distance (r_c)[27].

At very low energies, if a molecule of sufficient size has a positive electron affinity and sufficient vibrational degrees of freedom, a corresponding TNI can relax through intramolecular vibrational energy redistribution (IVR), forming a metastable anion[25].

$AB^{(\ddagger)-} \rightarrow AB^{-}$ (1.12)

Lastly, relaxation can occur through dissociation of the TNI, also known as dissociative electron attachment (DEA). As discussed earlier, the electron attachment is usually to an anti-bonding state where relaxation results in the lengthening of the AB bond length. If the TNI does

not have any viable alternatives and r(A-B) stretches beyond r_c and dissociation and the formation of a negative ion fragment and a neutral radical counterpart[26].

$$AB^{(\ddagger)-} \rightarrow A^{(\ddagger)-} + B^{(\ddagger)} \quad (1.13)$$

In order to induce a single bond rupture in DEA the electron affinity of the charge-retaining molecular fragment (A) must exceed the respective bond dissociation energy (BDE(AB));

$$E_{th}(A^-) = BDE(AB) - EA(A) \quad (1.14)$$

It is worth noting that often times, the measured threshold energy (known as appearance energy) is larger than the actual thermochemical threshold. This is attributed to the behavior of resonances which can be observed above their respective energetic thresholds. The excess energy, in these situations, comes from the molecule's vibrational / electronic excitation state or kinetic energy[25].

1. 3. Thin Film Growth and Etching in a Vacuum

Thin films have been proven to noticeably affect the physical properties of the materials on which they reside. Both the composition and the thickness of these films play a large role in their resulting properties. This section will explore several different ways films can be grown and etched away in a vacuum.

Electron Beam Induced Deposition:

One of the more important mechanisms of film growth is through the deposition of adsorbed molecules in the presence of energetic species such as electrons[6, 28-30]. This phenomenon occurs predominantly in low pressure vacuum environments, when surfaces are exposed to both volatile molecules and electrons simultaneously. In these situations interactions between the

electrons and transiently adsorbed species on the surface of a material or substrate cause deposits to form[6]. This type of deposition is often unwanted such as: the co-deposition and accumulation of radioactive fuel on the walls of tokamak fusion reactors; diminishing response in various electron multipliers; and reduction in beam quality / stability in UV synchrotrons[31, 32]. Film deposition, mediated by these same energetic species, has also been used for positive effects. Currently, electron beam induced deposition (EBID) is being used in the repair of extreme ultraviolet light lithography masks, the production of custom tips for scanning tunneling / atomic force microscopes, and as a method for fabricating hall sensors[15, 29, 33, 34].

The electron beam-induced deposition process is schematically represented in Figure 1.1. It is generally accepted that the deposition process is driven by low energy, secondary electrons produced when a high energy, principal electron beam interacts with the substrate. The low energy electrons interact with transiently adsorbed molecules on the surface of the substrate causing these molecules to decompose into both non-volatile and volatile components. The resulting volatile fragments are pumped off while the non-volatile fragments are incorporated into the deposit.

Electron-Induced Carbon Nanomembrane Fabrication:

Carbon nanomembranes (CNMs) are free-standing films with thicknesses of only a few nanometers[19] . These two-dimensional molecular sheets boast a high mechanical strength and thermal stability along with various other properties which can be tailored depending on the molecular composition and structure of the assembled molecular layers[19-21]. One method of CNM fabrication involves the use of electrons to induce cross-linking of specific aromatic self-assembled monolayers (SAMs)[14, 16-18].

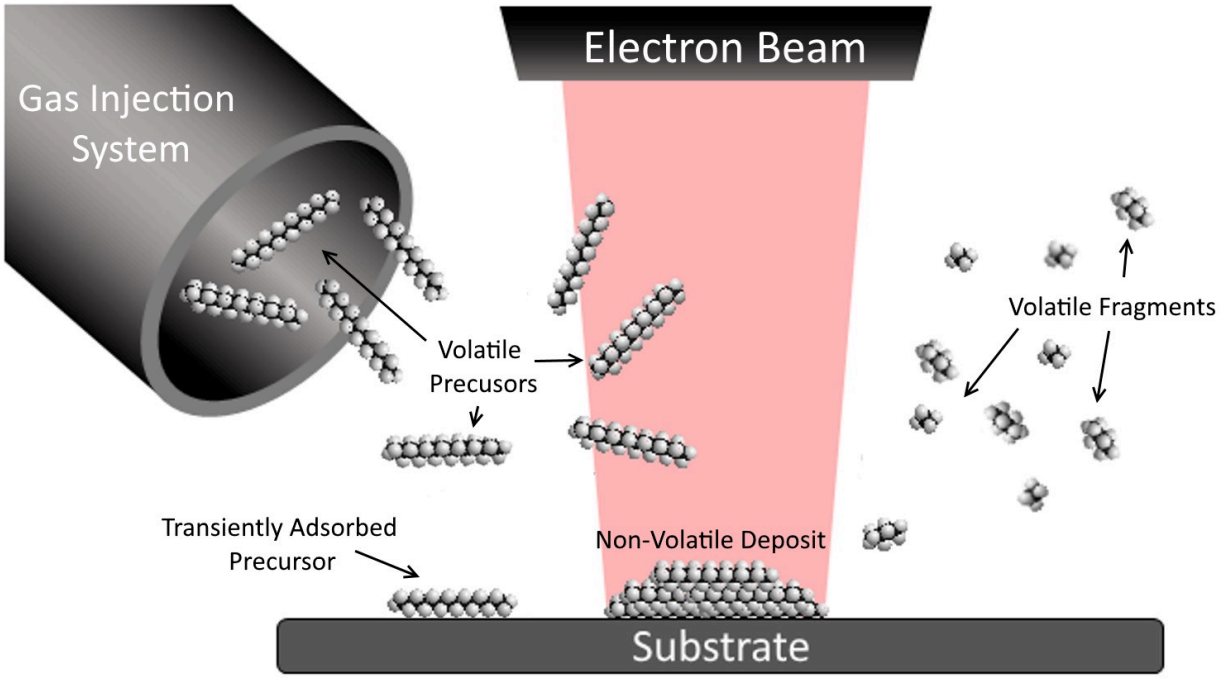

Figure 1. 1: Schematic of the EBID process showing the gas injection of a volatile precursor and the electron beam used to decompose the transiently adsorbed precursor into non-volatile deposit and volatile fragments.

It is generally thought that, for typical aromatic monomers of SAMs cross-linking occurs through electron-induced C-H and C-C bond cleavage in the monomers[8]. The resulting reactive radical site, generated through bond cleavage, induces a cross-link with neighboring SAM monomers. Propagation of this effect across the film's surface results in a laterally cross-linked monomolecular film (nanomembrane). While this cross-linking can be initiated directly through the primary (high energy) electron interaction, it is generally thought that backscattered and secondary electrons play a more dominant and direct role in the bond cleavage step[35-38].

Ion Etching:

Ion etching or milling is highly-developed technology, prolific in nanofabrication and vacuum communities[39, 40]. It has been used, with great effect, for surface cleaning, material ablation, and even the milling of precise three-dimensional nanostructures. The process by which it works is known as sputtering. Ion etching statrs with the creation of charged ions in the sputter source, commonly through the electron-impact of a high molecular weight molecule or atom such as argon. The charged ions are then accelerated from the source to a target to be ablated. When a beam of energetic ions collides with atoms on the surface of a solid, energy and momentum are transferred from the particles to the lattice[40]. As long as the energy transferred exceeds the chemical binding energy or momentum is imparted away from the surface, material and atoms will be removed.

The details behind this many-body interaction are complex but there are some generalities. There is a threshold for the sputtering process with an onset of between 5-40 eV depending on the solid and relating to the sublimation heat of the material, its crystallographic orientation, and the mass of the incident ion[40]. At energies below 1 keV only the first few nanometers of the surface

will be involved in sputtering making it relatively uniform. However, at energies higher than a few keV, surface-layer damage becomes noticeable[40]. Additionally, while it can be applied to etch any surface, different elements etch at different rates which can result in preferential sputtering. While ion etching has been used in precise applications, it is generally considered very damaging for atomically smooth surfaces due to its violent nature.

Atomic Hydrogen Etching:

Due to the prolific nature of carbonaceous films, many techniques have been developed to mitigate or remove these contaminative films. A particularly useful approach to remove carbonaceous films, without damaging the underlying substrate, is through the use of atomic hydrogen. Such etching has been used to great effect in cleaning surfaces that would be otherwise damaged or destroyed using other contamination removal methods like ion sputtering or chemical etching[41, 42]. In general, this process works by using atomic hydrogen's innate reactivity to create volatile species that desorb from the surface and are pumped away.

When exposed to atomic hydrogen, carbonaceous films first undergo hydrogenation. Atomic hydrogen exposure of sp- and sp^2-hybridized CH groups leads to the formation of sp^3-hybridized CH_x (x=2,3) groups and so on[43]. Eventually this hydrogenation leads to erosion of the adsorbed film via the desorption of volatile C_xH_y molecules, such as methane and ethane[43]. While this technique can readily clean contaminated surfaces of hydrocarbons without damaging them, it is mostly limited to the cleaning of carbonaceous materials, with a few exceptions. Additionally, in comparison to other etching techniques, the etch rate of this technique is relatively slow.

1. 4. Analytical Techniques

In order to track the effect electrons have on thin films and their creation, multiple techniques must be utilized. This section explores the different analytical techniques, both surface and gas phase, that can be utilized in order to map and characterize the changes induced by electrons.

X-ray Photoelectron Spectroscopy:

X-ray photoelectron spectroscopy (XPS), also known as electron spectroscopy for chemical analysis (ESCA) is one of the more powerful and common chemical-analytical techniques[44]. In this technique, a surface is irradiated with x-rays causing the emission of electrons produced by both the photoelectric and Auger effect. Electrons emitted by the photoelectron process have a kinetic energy (E_K) that depends on the energy of the photon ($h\nu$), the binding energy of the atomic orbital from which the electron originates (E_B), and the work function of the spectrometer (ϕ)[44]. This relationship is summarized in the following equation and Figure 1.2.

$$E_B = h\nu - E_K - \phi \quad (1.15)$$

In the case of XPS, Auger electron emission is primarily initiated by the creation of an ion with an inner shell vacancy induced by x-ray bombardment[45] (see Figure 1.3). The kinetic energy of an Auger electron is equal to the energy difference between the singly ionized state and the double ionized final state. For an arbitrary ABC transition in an atom, the Auger electron kinetic energy (E_{ABC}) is given by the difference in the binding energies of the energy levels A, B, and C[46]:

$$E_{ABC} = E_A - E_B - E_C^* - \phi \quad (1.16)$$

where ϕ is the work function of the spectrometer and E^* is the binding energy of a level in the presence of a core hole and greater than the binding energy of the same level in a neutral atom[45].

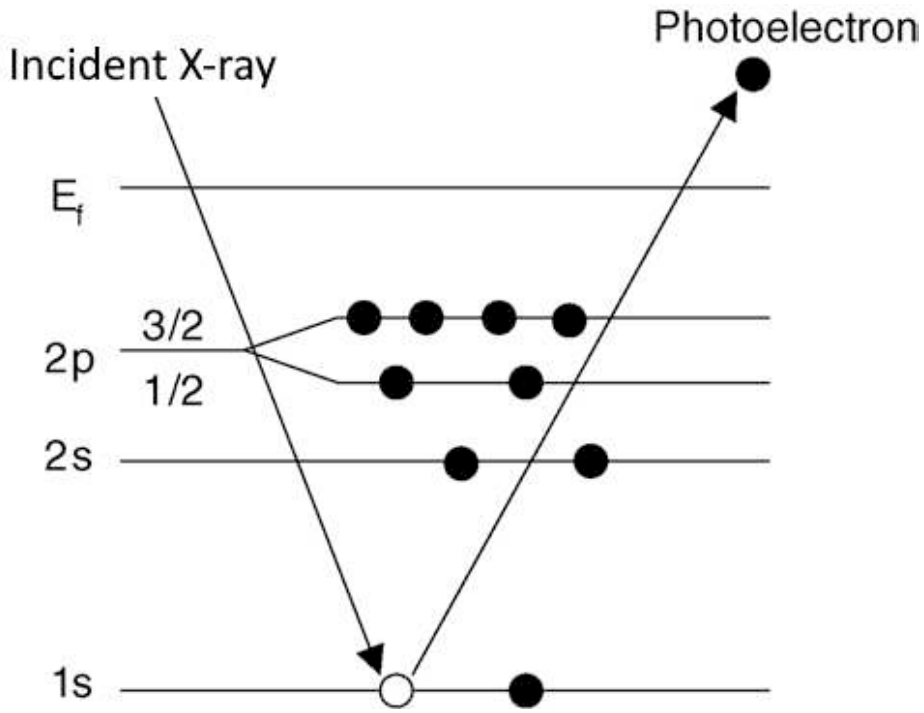

Figure 1. 2: Schematic of the emission process of photoelectrons excited by X-rays[6].

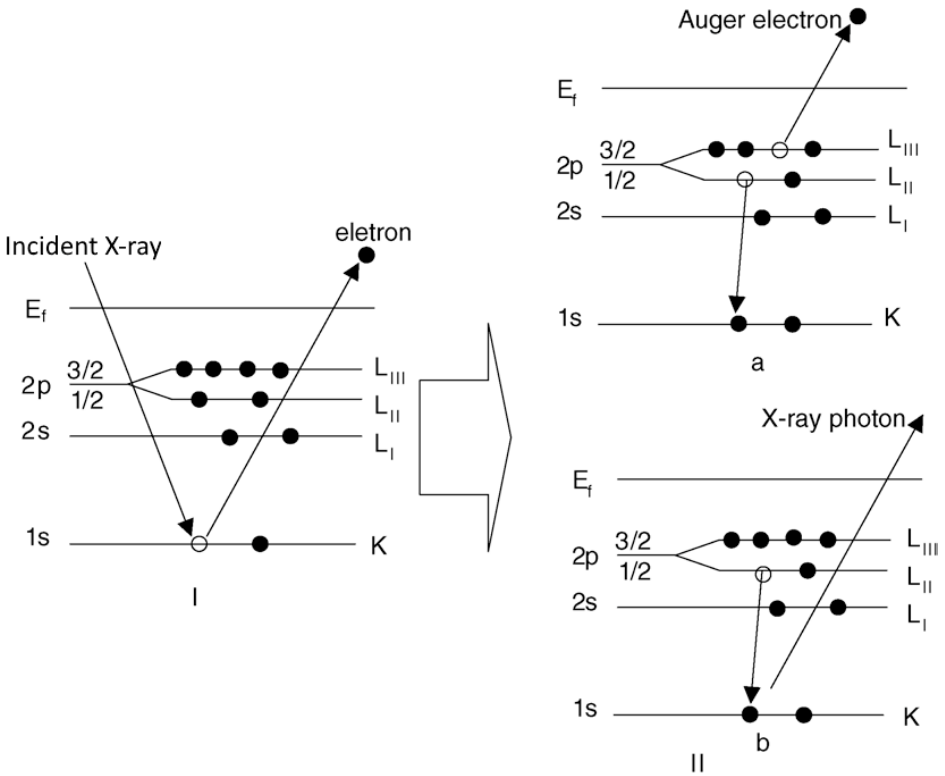

Figure 1. 3: Schematic of the Auger emission process. (IIa) $KL_{II}L_{III}$ transition or simply a KLL transition and x-ray fluorescence (II-b)[6].

Because each element has a unique set of binding energies, both the Auger and photoelectric emissions from XPS can be used to identify and determine the concentration of the elements within the escape depth of the corresponding photoelectrons, at the surface of the material (<30 nm)[45, 47]. Additionally, variations in the elemental binding energies (chemical shifts) can result due to differences in the surrounding elements and the nature of their bonds. The corollary is that these chemical shifts can be used to identify the chemical state of the materials being analyzed[48]. The surface sensitive nature of the technique also allows for the determination of film thickness.

In addition to composition, speciation, and thickness, advancements in modern XPS instrumentation have given this technique the capacity to laterally map differences in surface composition and bonding. Lateral surface composition can be determined using two different techniques, parallel imaging or chemical mapping[49]. Parallel imaging collects the signal intensity of a specific kinetic energy across a two-dimensional field of view. Scans at various kinetic energies allows for the acquisition of chemical spectra for each individual pixel. While its lateral resolution (on the order of 1-10um) is much improved over chemical mapping (on the order of 50-100um), it's requirement of a high pass energy results in a relatively low spectral resolution. Chemical mapping, however, utilizes a low pass energy and collects signal from a single tightly analyzed spot (~55um in diameter). Using a precision stage, scans are taken at various locations along the sample. At the sacrifice of lateral resolution, chemical mapping gives improved spectral resolution. It is worth noting that depending on the material and scan window, scans times for XPS imaging and chemical mapping can be prohibitively long. A high-resolution chemical map can take upwards of several minutes per pixel resulting in a total scan time of several hours or days depending on the region of interest.

XPS however, does have some drawbacks. XPS cannot directly measure hydrogen. This somewhat limits its usefulness when applied to organic materials. Additionally high energy ionizing radiation can induce chemical and structural changes to susceptible films. Consequently, sample damage may be of concern. While most solid materials such as metals and ceramics are generally stable under x-ray irradiation, certain polymers and soft biological specimens are mutable[6].

Spectroscopic Ellipsometry:

Spectroscopic ellipsometry (SE) is a non-destructive optical technique which is particularly useful for thin film analysis. In ellipsometry, (see Figure 1.4) a sample is illuminated by a beam of polarized light. The change in polarization state of the incident beam, induced by reflection from or transmission through the sample is measured and characterized by the ellipsometric psi (ψ) and delta (Δ) parameters defined in the following equation[50-54].

$$\tan(\psi) \cdot e^{i\Delta} = \rho = \frac{r_p}{r_s} \quad (1.17)$$

In this equation, rho (ρ) is the ratio of reflectivity for p-polarized light (r_p) divided by the reflectivity for s-polarized light (r_s). The corollary of this equation is that the ellipsometric parameters of psi and delta simply report ρ, a complex number, in polar form with $\tan(\psi)$ corresponding to the magnitude of the reflectivity ratio and Δ being the phase. This allows ellipsometry to have better precision, sensitivity, and information when compared to simple intensity-based reflection or transmission spectroscopies[54, 55]. In spectroscopic ellipsometry, psi and delta are acquired as a function of wavelength greatly increasing the information content in the data set[50]. This enables SE to determine multiple sample properties, such as film thickness, surface roughness, and optical constants, simultaneously[51, 54, 56, 57]. Due to the numerous factors .

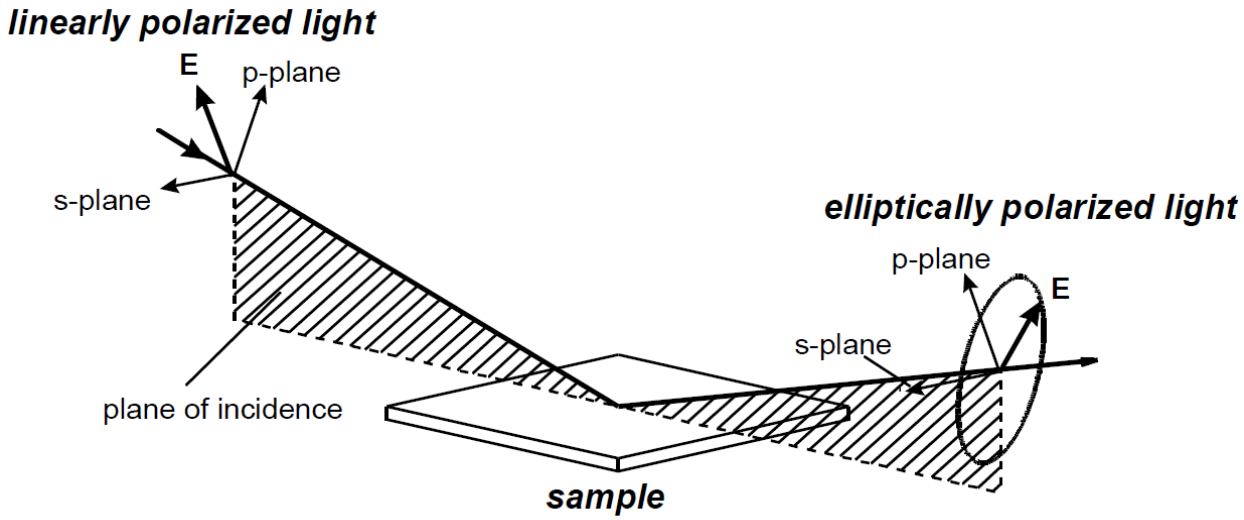

Figure 1. 4: Interaction of polarized light with a sample[48].

influencing the physical parameters obtained by SE measurements, often a model must be used to extract useful information from the SE Data. This makes this technique only as accurate as the model used to parameterize the results[53, 55]. Modeling of SE data starts by selecting an appropriate number of layers or phases. For bulk samples, without surface oxides, roughness, or adsorbed/deposited thin films, the optical constants of a material can be directly determined from the ellipsometric data. The following equation can be used to transform psi and delta into the material optical constants n and k (or equivalently, the complex dielectric functions values ε_1 and ε_2)[50].

$$\langle\varepsilon\rangle = \langle\varepsilon_1\rangle + i\langle\varepsilon_2\rangle = \langle\tilde{n}\rangle^2 = (\langle n\rangle + i\langle k\rangle)^2 = sin(\phi)^2 \cdot \left[1 + tan(\phi)^2 * \left(\frac{1-\rho}{1+\rho}\right)^2\right] \quad (1.18)$$

Here, ϕ is the angle of incidence and ρ is the ratio of reflectivity defined earlier in Equation 1.3. This equation, however, is only valid if all the aforementioned assumptions are met and since this is rarely the case, the brackets ("< >") are used to denote that these are pseudo optical constants. For most thin film analysis, a standard three-phase (air, substrate, and film) model is sufficient. In this model, each phase consists of a set of optical (n,k) or dielectric (ε_1, ε_2) functions with the addition of a thickness parameter that applies to the thin film phase[50, 51, 53]. The optical functions for air, (most) substrates, and even some thin films are well known and have tabulated data associated with them. However, for materials with unknown dielectric functions, a parameterizable model must be used, dictated by material being analyzed. Common models include the Cauchy, Tauc-Lorentz, and the B-Spline and their relative strengths, weaknesses, and formulations are outlined elsewhere the associated layer[55, 57].

Using a precision stage, SE instrumentation can laterally map materials and thin films by limiting the analysis area and taking measurements at a series of locations. While tabulated data and models like the Tauc-Lorentz and B-spline can parameterize a wide array of substances, they

are less useful when describing heterogeneous anisotropic films where the optical properties may vary across a surface. In situations like these, the Bruggeman effective medium approximation (BEMA) can be employed[58]. The Bruggeman approximation is designed to give a symmetric description of the effective dielectric constant of multi-component materials. BEMA assumes that each constituent material retains its original dielectric response[59, 60]. If the optical properties for the individual constituents are known, the overall material can be parameterized using a combination of the components.

Electron Impact Mass Spectrometry:

Mass spectrometry (MS) is a technique used to analyze the composition and concentration of gaseous species in a vacuum. This analysis starts by ionizing the gaseous molecules to make them susceptible to electric and magnetic fields. From there, the ionized molecules are extracted into a variable electric and/or magnetic field (usually a quadrupole) where they are separated according to their mass to charge ratio (m/z) and sent toward a detector to measure the total ion yield.

Most electron impact sources utilize 70 eV electrons to produce ionic fragments. The relatively high impact energy of these sources usually results in an extensive and unique fragmentation which can be used to decipher the structure of the parent molecule. However, more precise impact instrumentation such as a trochoidal electron monochromator, can be utilized to impact molecules with electrons of specific energies ranging from 0-70 eV. This level of control can greatly improve the analysis capabilities of the instrument allowing it to study the effects of electrons on various molecules[61].

1. 5. References

1. Kaplan, I. G., The track structure in condensed matter. *Nuclear Instruments and Methods in Physics Research Section B: Beam Interactions with Materials and Atoms* **1995,** *105* (1), 8-13.
2. Seah, M. P., Slow electron scattering from metals: I. The emission of true secondary electrons. *Surface Science* **1969,** *17* (1), 132-160.
3. Henderson, M. A.; Ramsier, R. D.; Yates, J. T., Low-energy electron induced decomposition of Fe(CO)5 adsorbed on Ag(111). *Surface Science* **1991,** *259* (1), 173-182.
4. Silinskas, M.; Grigonis, A., Low energy post-growth irradiation of amorphous hydrogenated carbon (a-C:H) films. *Diamond and Related Materials* **2002,** *11* (3), 1026-1030.
5. Li, Z.; Zheng, Y.; Cloutier, P.; Sanche, L.; Wagner, J. R., Low Energy Electron Induced DNA Damage: Effects of Terminal Phosphate and Base Moieties on the Distribution of Damage. *Journal of the American Chemical Society* **2008,** *130* (17), 5612-5613.
6. Arumainayagam, C. R.; Lee, H.-L.; Nelson, R. B.; Haines, D. R.; Gunawardane, R. P., Low-energy electron-induced reactions in condensed matter. *Surface Science Reports* **2010,** *65* (1), 1-44.
7. Landheer, K.; Rosenberg, S. G.; Bernau, L.; Swiderek, P.; Utke, I.; Hagen, C. W.; Fairbrother, D. H., Low-Energy Electron-Induced Decomposition and Reactions of Adsorbed Tetrakis(trifluorophosphine)platinum [Pt(PF3)4]. *The Journal of Physical Chemistry C* **2011,** *115* (35), 17452-17463.
8. Amiaud, L.; Houplin, J.; Bourdier, M.; Humblot, V.; Azria, R.; Pradier, C. M.; Lafosse, A., Low-energy electron induced resonant loss of aromaticity: consequences on cross-linking in terphenylthiol SAMs. *Physical Chemistry Chemical Physics* **2014,** *16* (3), 1050-1059.
9. Yokoya, A.; Shikazono, N.; Fujii, K.; Urushibara, A.; Akamatsu, K.; Watanabe, R., DNA damage induced by the direct effect of radiation. *Radiation Physics and Chemistry* **2008,** *77* (10), 1280-1285.
10. Madey, T. E.; Johnson, R. E.; Orlando, T. M., Far-out surface science: radiation-induced surface processes in the solar system. *Surface Science* **2002,** *500* (1), 838-858.
11. Lu, W.; Komvopoulos, K., Nanotribological and Nanomechanical Properties of Ultrathin Amorphous Carbon Films Synthesized by Radio Frequency Sputtering. *Journal of Tribology* **2000,** *123* (3), 641-650.
12. Hans , W. P. K.; Johannes, K.; Michael, R.; Markus, W.; Gerold, D.; Kam , L. L., Characterization and Application of Materials Grown by Electron-Beam-Induced Deposition. *Japanese Journal of Applied Physics* **1994,** *33* (12S), 7099.
13. Zhou, Z.; Zhao, X. S.; Zeng, X. T., Surface patterning with carbon thin films by nanosphere lithography. *Surface and Coatings Technology* **2005,** *198* (1), 178-183.
14. Turchanin, A.; Tinazli, A.; El-Desawy, M.; Großmann, H.; Schnietz, M.; Solak, H. H.; Tampé, R.; Gölzhäuser, A., Molecular Self-Assembly, Chemical Lithography, and Biochemical Tweezers: A Path for the Fabrication of Functional Nanometer-Scale Protein Arrays. *Advanced Materials* **2008,** *20* (3), 471-477.
15. Utke, I.; Hoffmann, P.; Melngailis, J., Gas-assisted focused electron beam and ion beam processing and fabrication. *Journal of Vacuum Science & Technology B: Microelectronics and Nanometer Structures Processing, Measurement, and Phenomena* **2008,** *26* (4), 1197-1276.
16. Beyer, A.; Godt, A.; Amin, I.; Nottbohm, C. T.; Schmidt, C.; Zhao, J.; Gölzhäuser, A., Fully cross-linked and chemically patterned self-assembled monolayers. *Physical Chemistry Chemical Physics* **2008,** *10* (48), 7233-7238.
17. Kankate, L.; Aguf, A.; Großmann, H.; Schnietz, M.; Tampé, R.; Turchanin, A.; Gölzhäuser, A., Vapor Phase Exchange of Self-Assembled Monolayers for Engineering of Biofunctional Surfaces. *Langmuir* **2017,** *33* (15), 3847-3854.

18. Schnietz, M.; Turchanin, A.; Nottbohm, C. T.; Beyer, A.; Solak, H. H.; Hinze, P.; Weimann, T.; Gölzhäuser, A., Chemically Functionalized Carbon Nanosieves with 1-nm Thickness. *Small* **2009,** *5* (23), 2651-2655.
19. Angelova, P.; Vieker, H.; Weber, N.-E.; Matei, D.; Reimer, O.; Meier, I.; Kurasch, S.; Biskupek, J.; Lorbach, D.; Wunderlich, K.; Chen, L.; Terfort, A.; Klapper, M.; Müllen, K.; Kaiser, U.; Gölzhäuser, A.; Turchanin, A., A Universal Scheme to Convert Aromatic Molecular Monolayers into Functional Carbon Nanomembranes. *ACS Nano* **2013,** *7* (8), 6489-6497.
20. Turchanin, A.; Gölzhäuser, A., Carbon Nanomembranes. *Advanced Materials* **2016,** *28* (29), 6075-6103.
21. Eck, W.; Küller, A.; Grunze, M.; Völkel, B.; Gölzhäuser, A., Freestanding Nanosheets from Crosslinked Biphenyl Self-Assembled Monolayers. *Advanced Materials* **2005,** *17* (21), 2583-2587.
22. Märk, T. D., 3 - Ionization of Molecules by Electron Impact. In *Electron–Molecule Interactions and their Applications*, Christophorou, L. G., Ed. Academic Press: 1984; pp 251-334.
23. Zipf, E. C., 4 - Dissociation of Molecules by Electron Impact. In *Electron–Molecule Interactions and their Applications*, Christophorou, L. G., Ed. Academic Press: 1984; pp 335-401.
24. Trajmar, S.; Cartwright, D. C., 2 - Excitation of Molecules by Electron Impact. In *Electron–Molecule Interactions and their Applications*, Christophorou, L. G., Ed. Academic Press: 1984; pp 155-249.
25. Hasted, J. B.; Mathur, D., 5 - Electron–Molecule Resonances. In *Electron–Molecule Interactions and their Applications*, Christophorou, L. G., Ed. Academic Press: 1984; pp 403-475.
26. Christophorou, L. G.; McCorkle, D. L.; Christodoulides, A. A., 6 - Electron Attachment Processes. In *Electron–Molecule Interactions and their Applications*, Christophorou, L. G., Ed. Academic Press: 1984; pp 477-617.
27. Champion, R. L.; Doverspike, L. D., 7 - Electron Detachment Processes. In *Electron–Molecule Interactions and their Applications*, Christophorou, L. G., Ed. Academic Press: 1984; pp 619-681.
28. Shuji, K.; Hideaki, T.; Katsumi, M., Microfabrication of diamond films by localized electron beam chemical vapour deposition. *Semiconductor Science and Technology* **2002,** *17* (10), 1096.
29. Utke, I.; Hoffmann, P.; Dwir, B.; Leifer, K.; Kapon, E.; Doppelt, P., Focused electron beam induced deposition of gold. *Journal of Vacuum Science & Technology B: Microelectronics and Nanometer Structures Processing, Measurement, and Phenomena* **2000,** *18* (6), 3168-3171.
30. Koops, H. W. P.; Schössler, C.; Kaya, A.; Weber, M., Conductive dots, wires, and supertips for field electron emitters produced by electron-beam induced deposition on samples having increased temperature. *Journal of Vacuum Science & Technology B: Microelectronics and Nanometer Structures Processing, Measurement, and Phenomena* **1996,** *14* (6), 4105-4109.
31. Budaev, V. P.; Khimchenko, L. N., Fractal growth of deposited films in tokamaks. *Physica A: Statistical Mechanics and its Applications* **2007,** *382* (2), 359-377.
32. Jacob, W., Surface reactions during growth and erosion of hydrocarbon films. *Thin Solid Films* **1998,** *326* (1), 1-42.
33. Gonzalez, C. M.; Slingenbergh, W.; Timilsina, R.; Noh, J.-H.; Stanford, M. G.; Lewis, B. B.; Klein, K. L.; Liang, T.; Fowlkes, J. D.; Rack, P. D. In *Evaluation of mask repair strategies via focused electron, helium, and neon beam induced processing for EUV applications*, SPIE Advanced Lithography, SPIE: 2014; p 7.
34. Utke, I.; Dwir, B.; Leifer, K.; Cicoira, F.; Doppelt, P.; Hoffmann, P.; Kapon, E., Electron beam induced deposition of metallic tips and wires for microelectronics applications. *Microelectronic Engineering* **2000,** *53* (1), 261-264.
35. Turchanin, A.; Schnietz, M.; El-Desawy, M.; Solak, H. H.; David, C.; Gölzhäuser, A., Fabrication of Molecular Nanotemplates in Self-Assembled Monolayers by Extreme-Ultraviolet-Induced Chemical Lithography. *Small* **2007,** *3* (12), 2114-2119.

36. Zhang, X.; Vieker, H.; Beyer, A.; Gölzhäuser, A., Fabrication of carbon nanomembranes by helium ion beam lithography. *Beilstein Journal of Nanotechnology* **2014,** *5*, 188-194.
37. Turchanin, A.; Beyer, A.; Nottbohm, C. T.; Zhang, X.; Stosch, R.; Sologubenko, A.; Mayer, J.; Hinze, P.; Weimann, T.; Gölzhäuser, A., One Nanometer Thin Carbon Nanosheets with Tunable Conductivity and Stiffness. *Advanced Materials* **2009,** *21* (12), 1233-1237.
38. Schaefer, J.; Hoelzl, J., A contribution to the dependence of secondary electron emission from the work function and fermi energy. *Thin Solid Films* **1972,** *13* (1), 81-86.
39. Vickerman, J. C.; Gilmore, I., *Surface Analysis: The Principal Techniques*. Wiley: 2009.
40. Glöersen, P. G., Ion−beam etching. *Journal of Vacuum Science and Technology* **1975,** *12* (1), 28-35.
41. B. Hill, S.; Faradzhev, N.; Richter, L.; Grantham, S.; Tarrio, C.; Lucatorto, T.; Yulin, S.; Schürmann, M.; Nesterenko, V.; Feigl, T., *Optics contamination studies in support of high-throughput EUV lithography tools*. 2011; Vol. 7969.
42. Grantham, S.; Tarrio, C.; B. Hill, S.; Richter, L.; Lucatorto, T.; van Dijk, J.; Kaya, C.; Harned, N.; Hoefnagels, R.; Silova, M.; Steinhoff, J., *The NIST EUV facility for advanced photoresist qualification using the witness-sample test*. 2011; Vol. 7969.
43. Biener, J.; Schubert, U. A.; Schenk, A.; Winter, B.; Lutterloh, C.; Küppers, J., A surface reaction with atoms: Hydrogenation of sp- and sp2-hybridized carbon by thermal H(D) atoms. *The Journal of Chemical Physics* **1993,** *99* (4), 3125-3128.
44. Matthew, J., Surface analysis by Auger and x-ray photoelectron spectroscopy. D. Briggs and J. T. Grant (eds). IMPublications, Chichester, UK and SurfaceSpectra, Manchester, UK, 2003. 900 pp., ISBN 1-901019-04-7, 900 pp. *Surface and Interface Analysis* **2004,** *36* (13), 1647-1647.
45. Chu, P. K.; Li, L., Characterization of amorphous and nanocrystalline carbon films. *Materials Chemistry and Physics* **2006,** *96* (2), 253-277.
46. Childs, K. D.; Carlson, B. A.; LaVanier, L. A.; Hedberg, C. L., *Handbook of auger electron spectroscopy : a book of reference data for identification and interpretation in auger electron spectroscopy*. 3rd ed. ed.; Eden Prairie (Minn.) : Physical electronics: 1995.
47. Zemek, J.; Hucek, S.; Jablonski, A.; Tilinin, I. S., Photoelectron escape depth. *Journal of Electron Spectroscopy and Related Phenomena* **1995,** *76*, 443-447.
48. Briggs, D., Handbook of X-ray Photoelectron Spectroscopy C. D. Wanger, W. M. Riggs, L. E. Davis, J. F. Moulder and G. E.Muilenberg Perkin-Elmer Corp., Physical Electronics Division, Eden Prairie, Minnesota, USA, 1979. 190 pp. $195. *Surface and Interface Analysis* **1981,** *3* (4), v-v.
49. Barlow, A. J.; Popescu, S.; Artyushkova, K.; Scott, O.; Sano, N.; Hedley, J.; Cumpson, P. J., Chemically specific identification of carbon in XPS imaging using Multivariate Auger Feature Imaging (MAFI). *Carbon* **2016,** *107*, 190-197.
50. *Complete Ease™ Software Manual*. J. A. Woolam Co., Inc. : 2011; Vol. Verson 4.63.
51. Fujiwara, H., *Spectroscopic Ellipsometry: Principles and Applications*. Wiley: 2007.
52. Irene, E. A., Applications of spectroscopic ellipsometry to microelectronics. *Thin Solid Films* **1993,** *233* (1), 96-111.
53. Jellison, G. E.; Merkulov, V. I.; Puretzky, A. A.; Geohegan, D. B.; Eres, G.; Lowndes, D. H.; Caughman, J. B., Characterization of thin-film amorphous semiconductors using spectroscopic ellipsometry. *Thin Solid Films* **2000,** *377-378*, 68-73.
54. Tompkins, H. G.; Hilfiker, J. N., *Spectroscopic Ellipsometry: Practical Application to Thin Film Characterization*. Momentum Press: 2015.
55. Weber, J. W.; Hansen, T. A. R.; Sanden, M. C. M. v. d.; Engeln, R., B-spline parametrization of the dielectric function applied to spectroscopic ellipsometry on amorphous carbon. *Journal of Applied Physics* **2009,** *106* (12), 123503.

56. Himcinschi, C.; Meyer, N.; Hartmann, S.; Gersdorff, M.; Friedrich, M.; Johannes, H.-H.; Kowalsky, W.; Schwambera, M.; Strauch, G.; Heuken, M.; Zahn, D. R. T., Spectroscopic ellipsometric characterization of organic films obtained via organic vapor phase deposition. *Applied Physics A* **2005,** *80* (3), 551-555.
57. Johs, B.; Hale, J. S., Dielectric function representation by B-splines. *physica status solidi (a)* **2008,** *205* (4), 715-719.
58. Logothetidis, S., Hydrogen-free amorphous carbon films approaching diamond prepared by magnetron sputtering. *Applied Physics Letters* **1996,** *69* (2), 158-160.
59. Hodgkinson, I. J.; Wu, Q. h., *Birefringent Thin Films and Polarizing Elements*.
60. Aspnes, D. E., Optical properties of thin films. *Thin Solid Films* **1982,** *89* (3), 249-262.
61. Bjarnason, E. H.; Ómarsson, B.; Engmann, S.; Ómarsson, F. H.; Ingólfsson, O., Dissociative electron attachment to titatinum tetrachloride and titanium tetraisopropoxide. *The European Physical Journal D* **2014,** *68* (5), 121.

Chapter 2

Use of X-ray Photoelectron Spectroscopy and Spectroscopic Ellipsometry to Characterize Carbonaceous Films Modified by Electrons and Hydrogen Atoms

2. 1. Introduction

Carbonaceous thin films can serve as useful coatings but are also often an unwanted source of surface contamination. As ultrathin films, they have proven effective in reducing friction/wear in tribology, and also as coatings to prevent substrate corrosion[1]. In addition, carbonaceous thin films have been shown to be effective in the assembly of super capacitors, lithium ion batteries, catalytic systems, and in lithography[2-5]. As contaminants, carbonaceous ultrathin films are ubiquitous and can be formed in numerous ways such as atmospheric exposure and as remnants of surface treatments. In extreme UV light lithography, projection optics reflectivity losses caused by nanometer-thick carbonaceous films degrades performance below production requirements[6].

One of the more important mechanisms of carbonaceous film growth is through deposition of adsorbed molecules in the presence of energetic species (ions, electrons and ionizing radiation)[7-10]. This phenomenon occurs predominantly in low pressure vacuum environments, when surfaces are exposed to hydrocarbons and ionizing radiation simultaneously. In these situations interactions between the energetic species and transiently adsorbed hydrocarbons on the surface of a material or substrate causes deposits to form[7]. This type of deposition is often unwanted such as: the co-deposition and accumulation of radioactive fuel on the walls of tokamak fusion reactors; diminishing response in various electron multipliers; and reduction in beam quality / stability in UV synchrotrons[11-12]. In electron imaging these deposits can obscure images, convolute spectra, and create problems for techniques such as: energy dispersive spectroscopy (EDAX); secondary electron microscopy (SEM); and transmission electron microscopy (TEM)[13].

The detailed effects of electrons on condensed matter has been well studied[7, 14-17]. Interactions between high-energy radiation and matter produces numerous, non-thermal, low-energy, secondary electrons. Inelastic collisions of these electrons with molecules and atoms are

considered the primary driving force behind electron stimulated decomposition and deposition. In the case of organic molecules, low energy electron induced dissociation preferentially breaks C-H bonds compared to C-C bonds resulting in the formation of strong carbon bonds with the surface and additional C-C bonds within the film[18-19]. For example, electron induced modification of alkanethiol SAMs results in pronounced desorption of hydrogen and carbon containing fragments as well as the appearance of C-C/C=C crosslinks[20]. Generally, electron exposure results in the dehydrogenation and reordering of the network structure into an amorphous and increasingly graphitic carbonaceous film[18-19, 21].

Several techniques have been developed to mitigate or remove contaminative carbonaceous films. Hydrogen atoms (AH) have been used with great effect in cleaning surfaces that would otherwise be damaged or destroyed by other contamination removal methods like ion sputtering or chemical etching[22-23]. The erosion of carbonaceous films by AH begins with hydrogenation of the film. Studies using high-resolution electron energy loss spectroscopy show that AH converts sp- and sp^2-hybridized CH groups to sp^3-hybridized CH_x (x = 2,3) groups[24]. Further AH exposure eventually leads to the erosion of the adsorbed film through the desorption of volatile C_xH_y molecules, such as methane and ethane[24].

Consequently, it is important to be able to identify the content and spatial distribution of different types of carbon in carbonaceous films. For example, the ratio of sp^2 to sp^3 hybridization has been shown to correlate with many physical properties[17, 25-26]. Hydrogenated carbon films rich in sp^3 hybridized carbon have been shown to exhibit large band gaps, while graphitic films (sp^2) have been shown to be more conductive[25-26]. In addition, sp^2/sp^3 hybridization ratios have been strongly linked to hardness, and even optical properties[16-17, 25-26]. A wide assortment of analytical techniques have been used to differentiate between different forms of carbon including EELS,

Auger, x-ray photoelectron spectroscopy (XPS), Raman, and spectroscopic ellipsometry (SE)[17, 25, 27-32]. XPS is particularly well suited to probe nanometer thick carbonaceous films due to its ability to determine film thickness and the chemical composition of the film (except for hydrogen). Additionally, changes in the core level binding energies as well as the shape of the spectral envelope can sometimes be used to distinguish between different chemical states. In the case of carbon, an XPS instrument with sufficient precision and energy resolution can distinguish between the subtle differences in the C 1s photoelectron peak for sp^2 and sp^3 hybridized carbon in graphite, low-density polyethylene, and diamond[33-35]. Moreover, using internal reference spectra, the ratio of sp^3/sp^2 carbon atoms can be determined by appropriate peakfitting of the corresponding C 1s peakshapes[28].

In addition to composition, speciation, and thickness, advancements in modern XPS instrumentation have given this technique the capacity to laterally map differences in surface composition and bonding. One approach is chemical mapping where signal is collected from a single tightly analyzed spot (~55 μm in diameter), then repeated at various locations[33]. With a precision stage and analyzer chemical mapping can provide lateral resolutions on the order of 50-100 μm, and a spectral resolution that can, in principle, map lateral changes in sp^2 vs sp^3-hybridization. It is worth noting that depending on the material and scan window, scans times for this type of XPS imaging can be prohibitively long. A high-resolution chemical map can take upwards of several minutes per pixel resulting in a total scan time of several hours or days depending on the region of interest.

Optical spectroscopies, which rely on the absorption, transmission, or reflection of photons, can be viewed as somewhat complementary analysis tools to XPS in carbon film characterization. Optical methods also offer the potential for rapid, nondestructive film characterization[36-38]. An

especially useful optical technique for thin film analysis is spectroscopic ellipsometry (SE), which measures the change in polarization of light upon reflection, recording the complex reflectance ratio, p, of the material. SE is sensitive to many thin film properties including film thickness, surface roughness, and optical properties (measured as a function of wavelength)[39-40]. Due to the numerous factors influencing the physical parameters obtained by SE measurements, an appropriate model must be used to extract useful information from SE data. Consequently, the physical parameters of a thin film that can be obtained from SE, such as the index of refraction and/or thickness are only as accurate as the model used to parameterize the results[25, 39-40].

Modeling SE data starts by selecting an appropriate number of layers or phases. For most carbonaceous thin film analysis, a standard three-phase (air, substrate, and film) model is sufficient. Each phase consists of a set of optical (n,k) or dielectric (ε_1, ε_2) functions that must be determined[26, 41-42]. In the case of ambient air and (most) substrates these optical functions are well known and have tabulated data associated with them. For materials with unknown dielectric functions (i.e. the carbonaceous film), a parameterizable model must be used. Two useful models, regarding amorphous carbon thin films, are the B-spline and Tauc-Lorentz models. The B-spline model uses a series of basis-splines to describe the total spline curve representing the dielectric function of the associated layer[39, 43]. The B-spline model is, however, a purely mathematical construct. It can, if improperly utilized, produce unrealistic results. However, as illustrated by Weber et al., a physical result for the parameterized complex dielectric function can be obtained by forcing ε_2 to be positive and using a Kramers-Kronig transform (of the B-Spline approximated ε_2) to predict ε_1[39, 43]. Under these constraints, use of the B-Spline method can be accurate in modeling the dielectric function of films (or substrates) where little to no information is known[39]. In contrast, the Tauc-Lorentz model is physics-based and has been developed and proven to

parameterize the dielectric function of amorphous materials with a degree of accuracy limited by the instrument itself[26, 39, 42, 44-45]. Studies by Jellison et al. have shown that many of the fitted parameters of the Tauc-Lorentz model can be correlated with other measured quantities of the material, such as band gap and the ratio of sp^3 to sp^2 hybridized carbon[26, 46]. Although the Tauc-Lorentz and B-spline models can parameterize a wide array of substances, they are less useful when describing heterogeneous anisotropic films where the optical properties of a film vary across the surface. In the context of carbonaceous films, this includes films containing various mixtures of different carbon species. In situations like these, the Bruggeman effective medium approximation (BEMA) can be employed[47]. The Bruggeman approximation is designed to give a symmetric description of the effective dielectric constant of multi-component materials. BEMA assumes that each constituent material retains its original dielectric response[48-49]. If the optical properties for the individual constituents are known, the overall material can be parameterized using a combination of the components. The Bruggeman effective medium approximation has been extensively used to approximate the dielectric response of inhomogeneous films for the microelectronics industry[50].

In this paper we employ XPS and SE to characterize nanometer thick carbon films created by electron beam induced deposition of tetradecane. Selected areas of these films were exposed to additional electron irradiation, altering their chemical and structural properties and creating deposits with different forms of carbon. These deposits were examined using the chemical mapping function of XPS and an imaging spectroscopic ellipsometer. XPS peakfitting techniques used to measure sp^2/sp^3 hybridization, normally applied to isotropic films, were applied to anisotropic films to monitor structural composition in different regions of the films. These results

were compared to SE data obtained from the same films. Both techniques were also used to monitor AH modification and etching of amorphous carbon films with different sp^2/sp^3 ratios.

2. 2. Experimental

Deposition / Post-deposition Exposure Chamber:

A customized UHV system, pumped by a combination of ion and turbomolecular pumps was constructed to enable deposition and subsequent post-deposition electron irradiation of deposits formed by tetradecane (see Figure 2.1). The electron beam from a Perkin-Elmer 10-155 Cylindrical-Auger Electron Optics System[1] was chosen due to its flux stability as well as its relatively large beam profile which allowed depositions to be sufficiently large enough (~3.0 mm in diameter) to create detailed maps using XPS[2]. The nude ion gauge and mass spectrometer (SRS RGA 200) were attached to flanges ~6" below the electron gun and sample stage. This removed them from the direct line of sight of the sample and eliminated stray electron irradiation and heating effects at the sample. The electron gun and camera (ThorLabs DCC1645c camera coupled to a modified MVL6X12Z optical system) were orientated such that the camera had a full view of the sample and was not eclipsed by the electron source. The camera was utilized to monitor the electron beam's profile and provide a targeting system to ensure that the electron beam could be positioned accurately on the substrates. A customized sample stage (Figure 2.2) was mounted to a manipulator arm that allowed for three-dimensional translation and rotation of the stage inside the chamber. To remove any residual gasses left over from the electron-

[1] The CMA on the Perkin-Elmer 10-155 Cylindrical-Auger Electron Optics System was not functional preventing in-situ Auger measurements.

[2] Commercial products are identified to specify the experimental conditions. This identification does not imply that the products are endorsed or recommended by the National Institute of Standards and Technology or that they are necessarily the most suitable for the purposes described.

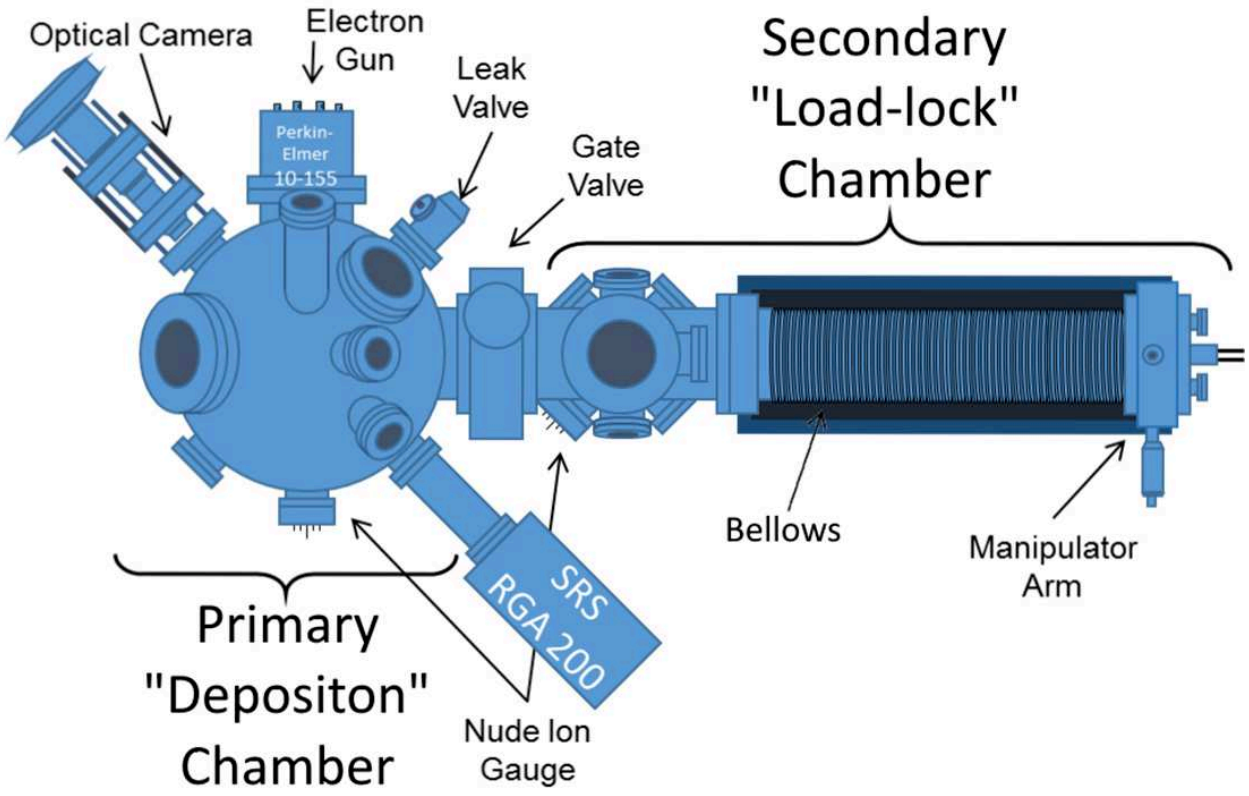

Figure 2. 1: Diagram of the chamber used for Electron Beam Deposition and Post-Deposition Modification of Carbonaceous Films.

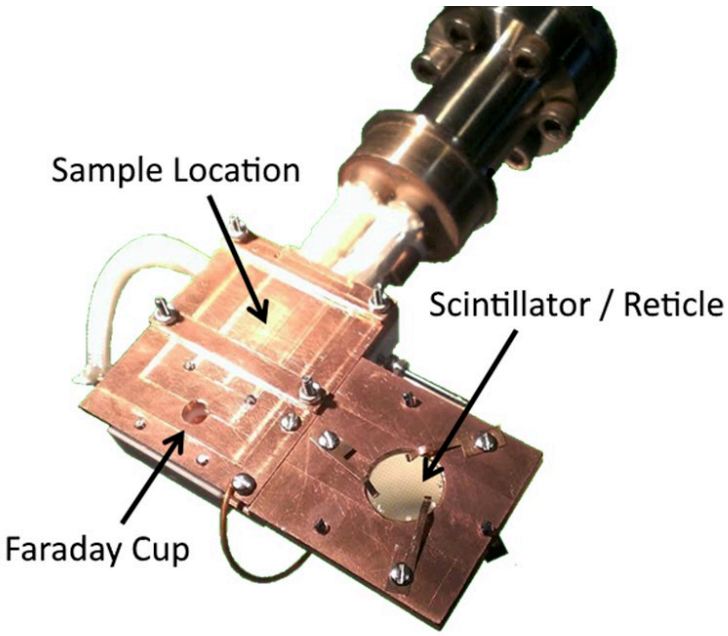

Figure 2. 2: Custom fabricated sample stage featuring an Al coated, Ce: YAG scintillator and faraday cup used to characterize and monitor the electron beam.

beam-induced deposition step, the primary chamber required a thorough bake-out / cleaning step. During this phase, the manipulator arm was retracted into a secondary chamber, allowing for the safe, in-situ, storage for the newly deposited samples. All in all, this allowed the main analysis chamber to maintain a base pressure < 1 x 10^{-9} Torr prior to deposition and during additional electron exposure.

Beam Calibration:

To calibrate and monitor the spatial profile of the electron beam, a custom sample stage, Figure 2.2, was fabricated. This stage was mounted onto the copper leads of a 1.33" CF flange combination Type K thermocouple / power feedthrough (Kurt J Lesker Company). The stage featured a faraday cup as well as an Al coated, Ce: YAG scintillator mounted on top of a 21 mm Diameter Contact Reticle, Metric Index Square Scale from Edmund Optics. The stage was fabricated such that the surface of the scintillator and the faraday cup all resided in the same plane as the deposition surface. The camera optical system was utilized in conjunction with the scintillator and reticle to calibrate the beam size, determine beam profile, and accurately position depositions on the Au coated, silicon samples. Example images of the electron beam profile, as illuminated by the scintillator, can be found in Figure 2.3. The faraday cup was utilized to calibrate the beam intensity and monitor flux stability. A Keithley 485 picoammeter was employed to measure the current incident on the faraday cup and the sample. A Type K thermocouple was utilized to monitor temperature throughout the experiment.

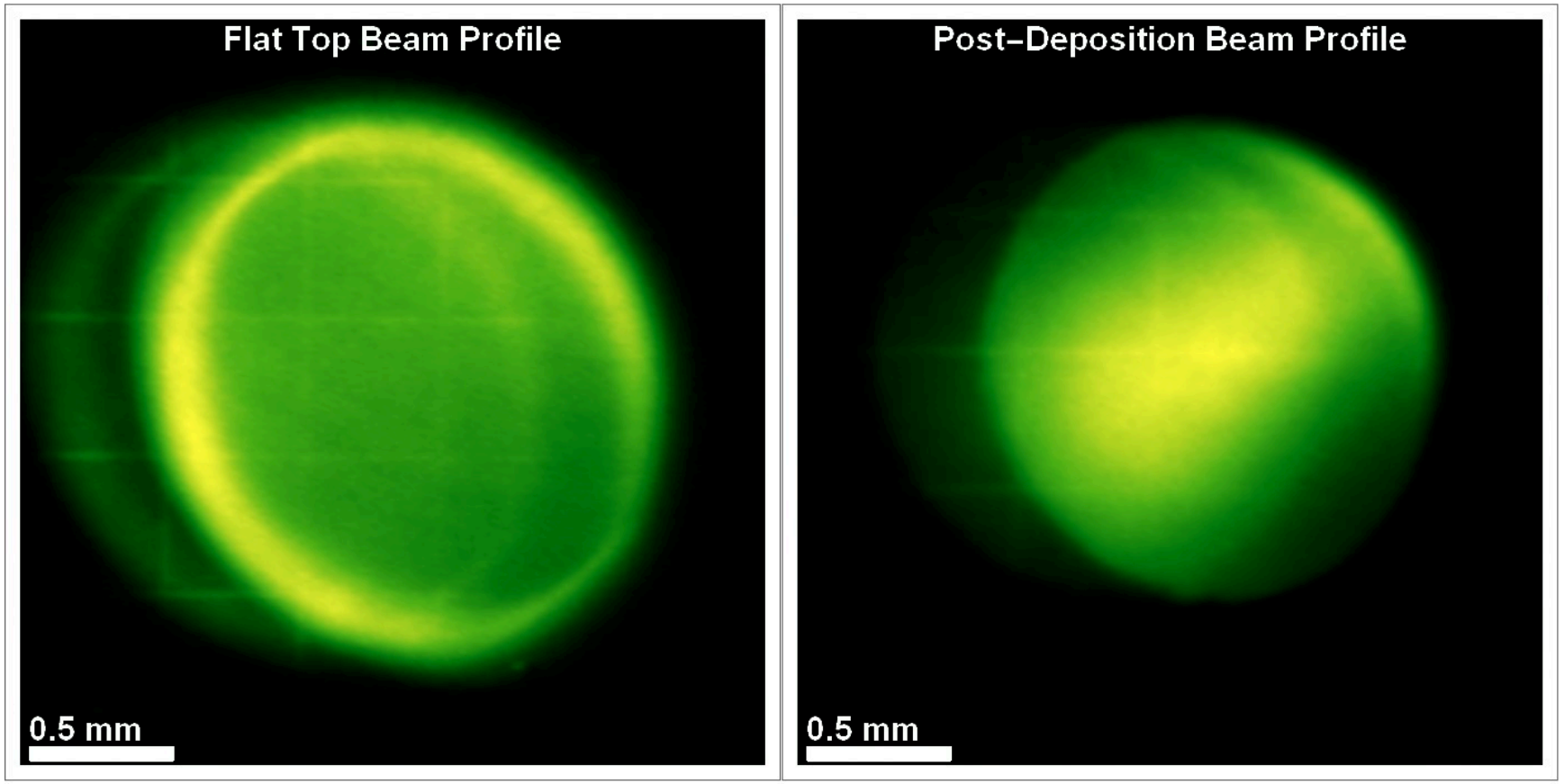

Figure 2. 3: Examples of the electron beam intensity distributions measured by the scintillator for the beams used to deposit tetradecane (left) and expose deposits to additional electron irradiation (right).

Film Deposition:

Film deposition was accomplished by dosing tetradecane into the customized UHV chamber while a gold coated silicon wafer was exposed to 2 KeV electrons generated by an electron gun. Tetradecane was chosen due to its volatility and because it (along with other hydrocarbons) is a common contaminant found in vacuum chambers[13, 22, 51]. Tetradecane was attached to a gas manifold and introduced into the chamber through a UHV leak valve. During deposition, the partial pressure of Tetradecane was measured using the most intense fragment (57 m/z) and was held at a constant pressure (3.0×10^{-6} torr)[3]. The partial pressures of residual gasses such as O_2 and H_2O were also monitored during deposition and remained $\leq 10^{-8}$ Torr.

Carbonaceous deposits were created on the gold coated silicon wafers that were mounted onto the custom sample stage shown in Figure 2.2 that also contained an Al coated, Ce: YAG scintillator used to calibrate the electron beam (see Beam Calibration section) and a Faraday cup to determine beam intensity/flux. A primary electron energy of 2 KeV was chosen as this value was sufficient to, (a) overcome the energy threshold of the scintillator and, (b) generate numerous low energy (< 100 eV) secondary electrons responsible for the deposition process.

During film deposition and post-deposition modification the trajectory of the electron beam was orthogonal to the plane of the substrate surface. A series of four deposits were made on each substrate. Each deposit was created by simultaneously exposing the sample to both electrons and tetradecane for about 45 minutes. For each set of depositions, the beam profile was adjusted to be as flat and uniform as possible across a ~3 mm diameter area, as monitored by the scintillator. Limitations of the electron gun prevented a truly flat profile and often resulted in a ring of higher

[3] The partial pressures of all gasses in the chamber were monitored by an attached RGA. See Deposition / Post-deposition Exposure Chamber section in SI for details.

intensity at the perimeter of the beam area. An example deposition beam profile, as imaged by the scintillator, reticle, and camera, can be found in Figure 2.3 (left panel). A single beam intensity of 22μA, as measured by the faraday cup, was utilized for all depositions and post deposition experiments. The substrate temperature remained at 24°C throughout electron exposure as determined by an attached K type thermocouple. The average thickness of the resulting deposits within a given sample set (four) was the same. However, the thickness between samples prepared on different substrates varied from ≈ 5.0 nm to ≈ 7.0 nm, thicknesses suitable for analysis by both SE and XPS.

Post-Deposition Modification:

After the initial deposits were made, the sample stage was retracted into the secondary chamber while the primary chamber was baked for several days to remove any latent tetradecane from the system. After bake-out, the cleanliness of the chamber was checked using an attached RGA. The only detectable gases in the deposition chamber were that of hydrogen and nitrogen/carbon monoxide ($< 1 \times 10^{-9}$ torr). The partial pressures of other gasses such as O_2, H_2O and tetradecane were below the detection limit of the RGA ($< 10^{-10}$ Torr). An additional measure of chamber cleanliness was determined by exposing a previously unexposed area of the substrate to the electron beam for 100 hours to create a "background" deposit. Calibration experiments indicated carbonaceous growth greater than ~2 nm could be visibly discerned by the attached camera. The absence of any visible evidence of a "background" deposit was therefore used as a qualitative indication that the partial pressure of tetradecane had been sufficiently reduced by the bake-out. It is worth noting that in the cases where the "background" deposit was visually identifiable (e.g. the deposit marked by an "x" in Figures 2.6 and 2.9), the chamber bake-out was

continued and the “background” test repeated until no visual evidence of a “background” deposit was observed.

After a bakeout sufficient to eliminate all residual tetradecane from the chamber, samples were exposed to post-deposition irradiation. In these experiments, the size of the electron beam was reduced to a diameter of ~1.5 mm, to comfortably fit inside the ~3 mm diameter deposits. In contrast to the flat top beam profile used to deposit films, the smaller beam used for post deposition film modification exhibited a gaussian-like intensity distribution when examined by the scintillator. An example of the post-deposition beam profile, as imaged by the scintillator, reticle, and camera, can be found in Figure 2.3 (right panel). An attached optical camera was used to position the post-deposition beam inside the deposits. Three of the four initial deposits were exposed to varying doses of the electron beam.

After deposition and post-deposition electron modification, the Au coated silicon substrate was removed from the UHV chamber and deposits were characterized ex-situ using X-ray photoelectron spectroscopy (XPS) and spectroscopic ellipsometry (SE). Following characterization, each set of carbon deposits were also cleaned using a purpose-built hydrogen atom cleaning system. In brief, the hydrogen atom cleaning system functioned by passing hydrogen gas across a hot filament positioned perpendicularly to and about 1-2 inches from the substrate. It has been shown that the rate of hydrogen atoms cleaning of carbonaceous films is strongly dependent on substrate temperature[52-53]. Consequently, throughout the AH cleaning process the substrate temperature was monitored closely. In our experiments the substrate temperature remained at 24°C. Following well defined exposures to the AH source, XPS analysis was performed. At the end of the AH cleaning, samples were also analyzed using SE.

XPS Characterization of Deposited Carbon:

Deposits were analyzed using a Kratos Axis Ultra scanning X-ray photoelectron spectrometer with a DLD detector and a monochromatized Al Kα source (1486.6 eV) operated at 300 W. The detection angle was set to be normal to the substrate. The location of the deposits was determined using an attached camera and confirmed in XPS by the increase in the C 1s signal and the corresponding decrease in Au 4f signal. Each deposit was characterized by two different XPS maps obtained using the chemical mapping method described in the introduction. The first XPS map was a succession of Au 4f region scans taken at a series of lateral positions across the deposit; 400 scans were taken at 200 μm intervals across a 4.0 mm x 4.0 mm area. Each scan was obtained using a probe size ≈ 250 μm in diameter, a pass energy of 160 eV, and a dwell time of about 200 ms per eV/step. The attenuation of the Au 4f peak area provided a measure of carbon thickness, d_c, in the deposits as compared to the trace levels of adventitious carbon located in areas of the sample not exposed to the electron beam. d_c was determined using Equation (1) where I and I_0 are the Au 4f photoemission signals inside and outside of the deposit respectively; λ is the effective attenuation length (EAL) of Au 4f electrons through tetradecane deposits[54]. An EAL of 2.7 nm was used based on the NIST Standard Reference database 82[55].

$$d_c = \lambda \cdot \ln\left({}^{I_0}/_{I}\right) \quad (2.1)$$

Au 4f XPS film thickness scans were taken after deposition, again after additional exposure to electrons and also at select intervals after well-defined exposures to AH.

For the second XPS map, a series of C 1s region scans were acquired at a series of lateral positions across each deposit; 1024 scans were taken at 100 μm intervals across a 3.2 mm x 3.2 mm area. Each scan was obtained using a probe size ≈ 125 μm in diameter, a pass energy of 20 eV, and a dwell time of about 700ms per eV/step. Each C 1s region scan required about a minute

of acquisition time resulting in maps that required a cumulative scan time of (> 5) hours per map[4]. As a result, these high-resolution scans were time intensive. Consequently, the number of these high-resolution C 1s map scans were limited and only taken prior to AH exposure and again after completion of the AH cleaning process.

SE Characterization of Deposited Carbon

Deposits were analyzed using a fixed angle J.A Woolam M-2000F spectroscopic ellipsometer. Each scan was taken at a fixed angle (65°) with a spot size of about 25 μm x 60 μm. Due to the fast acquisition time (on the order of milliseconds per spot), scans were taken at 100 μm intervals across an 8.0 mm v 8.0 mm area which encompassed all depositions on the surface of the wafer. Data analysis and parameterization was performed using CompleteEase software. While the ellipsometer had a functional range between 1.24 and 5.1 eV (~ 193 and 1000 nm), deadzones in the spectrometer resulted in aberrant spikes in the ellipsometry data around 1.40 and 1.50 eV (see Figure 2.7). To eliminate the effect of these deadzones, data fitting and analysis was limited to a range of 1.51 - 5.10 eV.

2. 3. Results and Discussion

XPS Characterization of Deposited Films:

As described in the experimental section, a series of four identical deposits were created. XPS thickness maps indicated < 10 % variation in thickness between the four deposits (± 0.6 nm

[4] XPS spectra taken from an as-deposited and additionally dosed carbon deposit were statistically the same as those measured after several hours (>48 hours) of x-ray exposure. This ensured the deposits were invariant to the X-Ray source used to probe the samples.

variance in samples averaging ≈ 6.0 nm). Moreover, there was no difference in the thickness maps between deposits that received no additional electron dose (as-deposited) and those that received as much as 100 hours of additional electron dose, as shown in the XPS thickness maps in the left-hand column of Figure 2.10. Thus, no measurable carbon was added or removed from the deposits as a result of the post-deposition electron exposure. The lack of deviation in XPS thickness profiles also demonstrates that the inelastic mean free path of the Au 4f electrons is insensitive to any structural changes induced by the incident electrons. Most importantly, any differences in film properties observed by SE and C 1s XPS analysis can be attributed solely to the effects of electron induced modification.

To understand the chemical and structural effects of additional electron irradiation, C 1s XPS maps were taken of both as-deposited films and films exposed to additional (post-deposition) electron irradiation. The insert in the left-hand panel of Figure 2.4 shows the XPS thickness map of a deposit after the central region (white dashed circle) was exposed to 28 hours of post-deposition electron irradiation. Analysis of the C 1s XPS data for this deposit revealed that three different and distinct C 1s spectral envelopes were present, each located within specific regions. Outside the deposit (Region A) a small, somewhat symmetrical, C 1s XPS signal was observed with a binding energy of about 285.2 eV. An averaged C 1s profile acquired in this region is shown in the left panel of Figure 2.4 (green). This background carbon species can be attributed to the presence of adventitious carbon as well as residual carbon from the polymer used to protect the Au-coated surface during the dicing process. Within the deposit, in areas not exposed to additional electron irradiation, a different C 1s profile was observed with a peak centered around 285.0 eV (as-deposited, Region B), whose intensity scaled with film thickness. This peak exhibited a narrower but slightly more asymmetric spectral profile as compared to the background carbon and

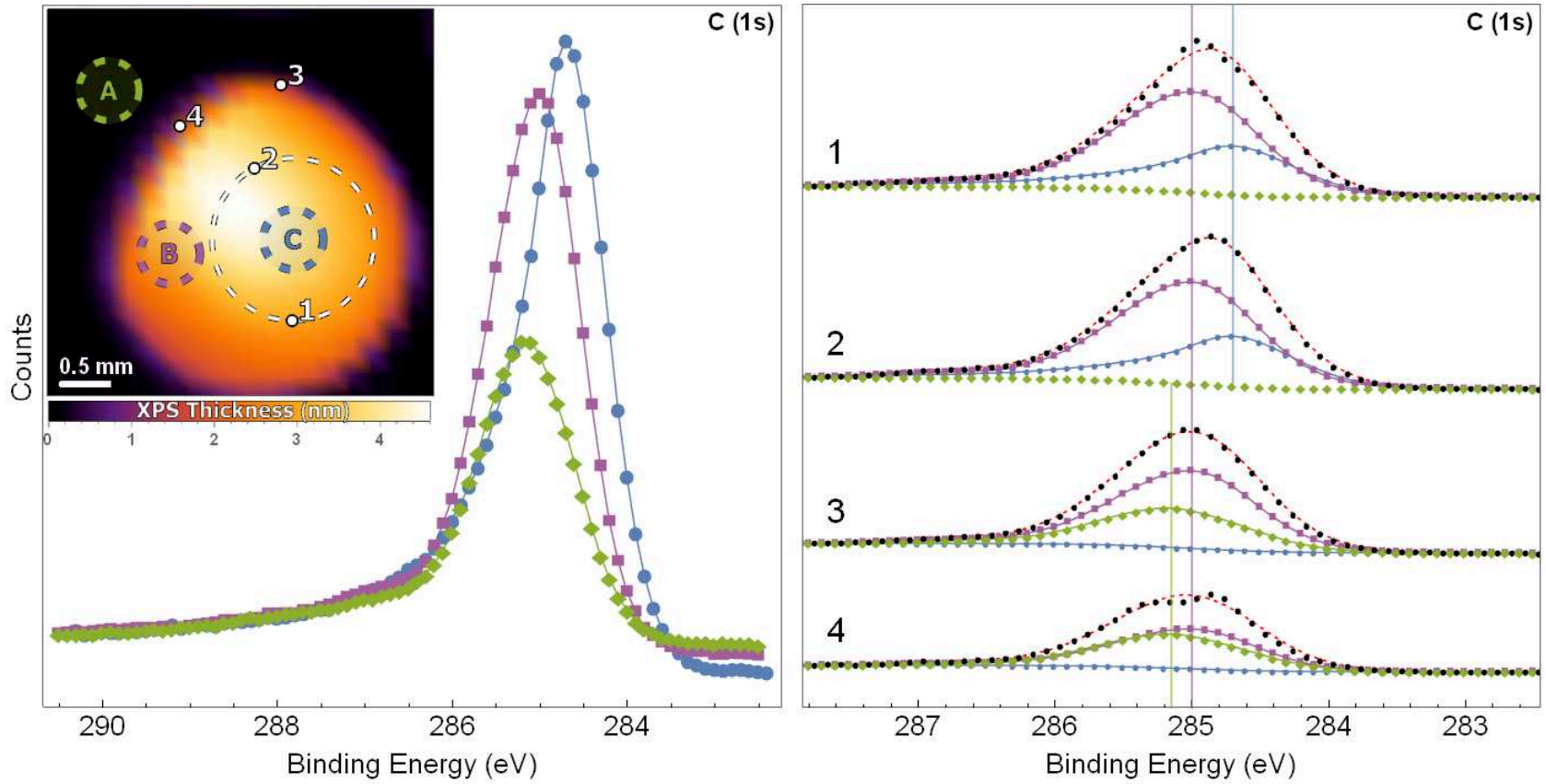

Figure 2. 4: (Inset, left panel) XPS thickness map of a deposit where the central region (white dashed circle) has been exposed to 28 hours of additional electron irradiation. Three different C 1s XPS profiles were identified in and around the deposit and marked accordingly; carbon contamination, found outside of the deposit (A, green), as-deposited tetradecane, located within the deposit (B, purple) and additionally electron irradiated (graphitized) carbon located within the additionally dosed region of the deposit (C, blue). (Left panel) Averaged C 1s spectra acquired from scans taken within each of the three regions (A, B, and C) identified in the inset as dashed circles. (Right Panel) Four example C 1s spectra (black dots) acquired at the four white numbered locations (1-4) shown in the inset, along with the corresponding fits using the three components shown in the left-hand panel. Each of the four numbered locations represents an interfacial region (e.g. between the deposit and the background region) where there are measurable contributions to the C 1s envelope from two of the components identified in the left-hand panel. The red dotted line represents the fitted linear combination of components A, B, C.

was attributed to the as-deposited carbon created during the deposition of tetradecane. Both the peak position and asymmetric profile are consistent with high resolution XPS scans of hydrogenated, sp^3 hybridized, amorphous carbon films observed by Lascovich et al.[33-34, 56-57] Spectra from Region B were averaged, and the results are shown in purple (left panel, Figure 2.4). Examination of the C 1s XPS spectra within regions of the deposit exposed to additional electron irradiation (Region C) revealed the presence of a third C 1s envelope, characterized by an asymmetric peakshape centered around 284.7 eV. Both the observed peakshape and peak position are consistent with sp^2 hybridized graphene and/or graphitic carbon species deposited onto metal surfaces[28, 33-34, 57]. Spectra from Region C were averaged; and the results are shown in Blue (left panel, Figure 2.4).

Using CasaXPS©, C 1s spectral envelopes were peakfit by means of a linear combination of the three components (background, as-deposited, and graphitized). While the relative intensities of each component were allowed to vary, both peak position and FWHM were fixed. This effectively determined the relative contribution of each carbon component at any point inside or outside the deposition region. Examples of the resulting spectral peakfitting, in locations where more than one type of carbon species was observed, can be found in the right-hand panel in Figure 2.4. For example, at the interface between additionally dosed and as-deposited regions, the C 1s profiles (#1 and #2 in Figure 2.4) could be well fit by a linear combination of as-deposited and graphitized carbon.

The spatially resolved contribution that the three different carbon species, identified in Figure 2.4, make to the C 1s envelopes of different deposits are shown in Figure 2.5. Darker and violet shades correspond to near zero intensities while white corresponds to the highest observed intensities. For a tetradecane deposit not exposed to any additional electron irradiation (top row,

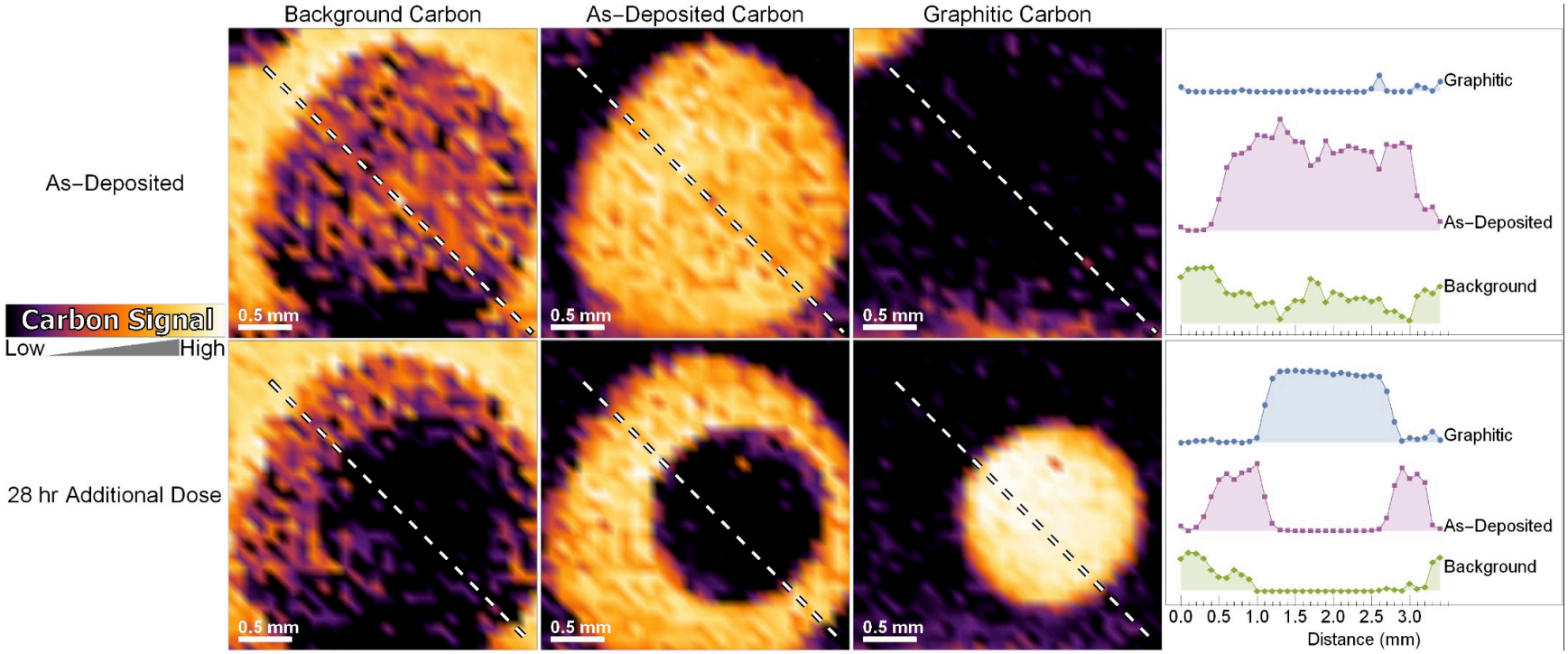

Figure 2. 5: Two-dimensional maps showing the relative contribution of the three C 1s components (background, as-deposited and graphitized carbon) for an as-deposited film (top row) and a film where the central portion has been exposed to an additional 28 hours of electron irradiation (bottom row). (Right column) Representative line profiles showing the relative intensity of background, as-deposited and graphitized carbon across the deposit, demarcated by a dashed white line.

Figure 2.5), regions outside the deposit exclusively contain background carbon while the deposit itself contains only as-deposited carbon. There is no contribution from the graphitized carbon. In a film exposed to 28 hours of electron irradiation following deposition (bottom row, Figure 2.5), background carbon, once again, is exclusively detected outside of the deposit. In the areas of the deposit not subject to additional electron irradiation, as-deposited tetradecane was detected. In contrast to the unexposed deposit, however, the center of the deposit (area exposed to additional electron irradiation) has been completely transformed into graphitized carbon. The relative concentration of these three-carbon species across the two deposits is shown more quantitatively by the representative line scans through the deposits which plot the relative percentage of each carbon species (background, as-deposited and graphitized).

SE Characterization of Deposited Films:

SE analysis of both as-deposited and additionally dosed films began by analyzing the raw values of psi and delta, measured at various wavelengths. When compared to results obtained from XPS, it became apparent that the both psi and delta were influenced by the overall film thickness and electron exposure. In general, it appeared that delta variations mostly correlated with overall film thickness (as determined by XPS), while psi variations tended to correlate closely with regions exposed to large doses of electrons. Examples of these psi and delta maps are found in Figure 2.6. This comparison demonstrated that spatial maps plotting the raw values of delta could be used as fiduciary markers to unify the XPS and SE coordinate systems. In practical terms, maps of delta values, measured at 1.24 eV (~1000 nm), and the corresponding XPS thickness maps were superimposed on top of one another. Their relative X/Y coordinates were adjusted until the two

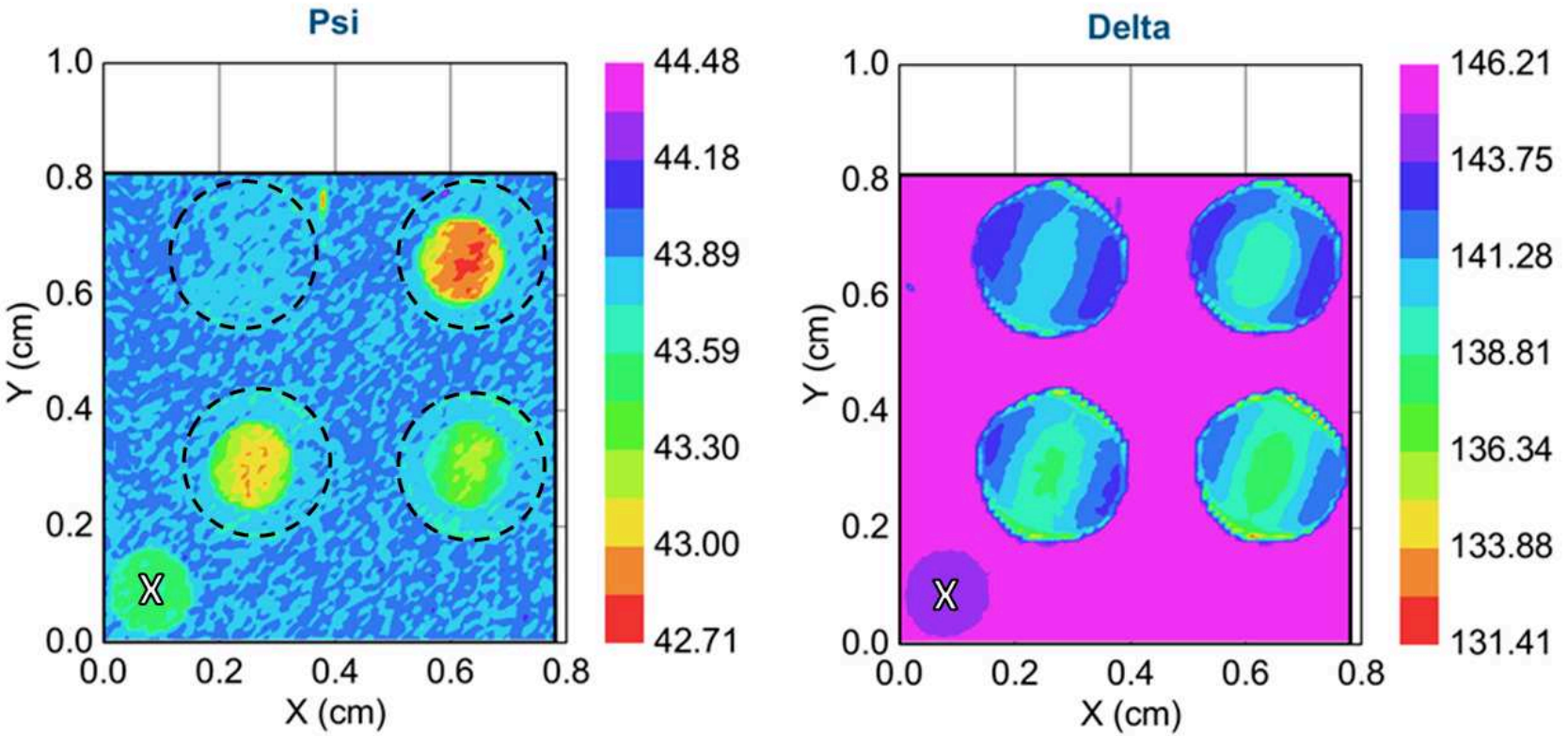

Figure 2. 6: Lateral maps plotting the Psi (left) and Delta (right) angles measured by scanning ellipsometry (SE), at an energy of 1.24 eV, for 4 amorphous carbon deposits; as-deposited tetradecane (top left), and deposits subsequently exposed to 1 hour, 21 hours, and 100 hours of additional electron exposure (bottom right, bottom left, and top right deposits, respectively). A black dashed line represents the anticipated location of deposits based on the beam profile. The deposit featured in the bottom left corner, demarcated by an "x", corresponds to a background deposit used to calibrate chamber cleanliness before post-deposition electron irradiation was conducted (See Experimental section for more details).

images overlapped, enabling XPS and SE data acquired from the same deposit to be directly compared.

XPS C 1s analysis revealed that the as-deposited tetradecane film was composed exclusively of sp^3-like, hydrogenated, carbon while the additionally dosed regions of the deposit exposed to 100 hours of additional electron irradiation was composed exclusively of graphitized sp^2-like carbon. To determine whether these different forms of carbon exhibit different optical/dielectric properties, three locations of identical thickness (as measured by XPS) were characterized by SE and plotted in Figure 2.7. Since film thickness is the same for all three locations, differences in psi and delta reflect differences in the optical properties of the deposits. Two of the locations (shown in red and purple) were taken from within as-deposited regions while the third (blue) was taken from a point that had been exposed to an additional 100 hours of electron irradiation. As expected, the two locations corresponding to as-deposited carbon show identical variations in psi and delta as a function of wavelength. However, these functional variations are measurably different in the location exposed to additional electron irradiation. Consequently, it can be inferred that electron irradiation changes the optical/dielectric properties of as-deposited films due to graphitization.

For SE to determine film thickness as well as the distribution of as-deposited and graphitized carbon within a deposit, it is necessary to model the SE data. The three-phase model, described in the introduction, was used to model the carbonaceous films[25, 39-40, 42]. To predict film thickness, the three-phase model requires accurate optical / dielectric functions for both the substrate and the film. The optical response of the Au-Si wafer (which included the background/contaminating carbon layer (< 1 nm) to reduce complexity of the model) was obtained using SE measurements taken at 30 different locations outside the area where deposition occurred.

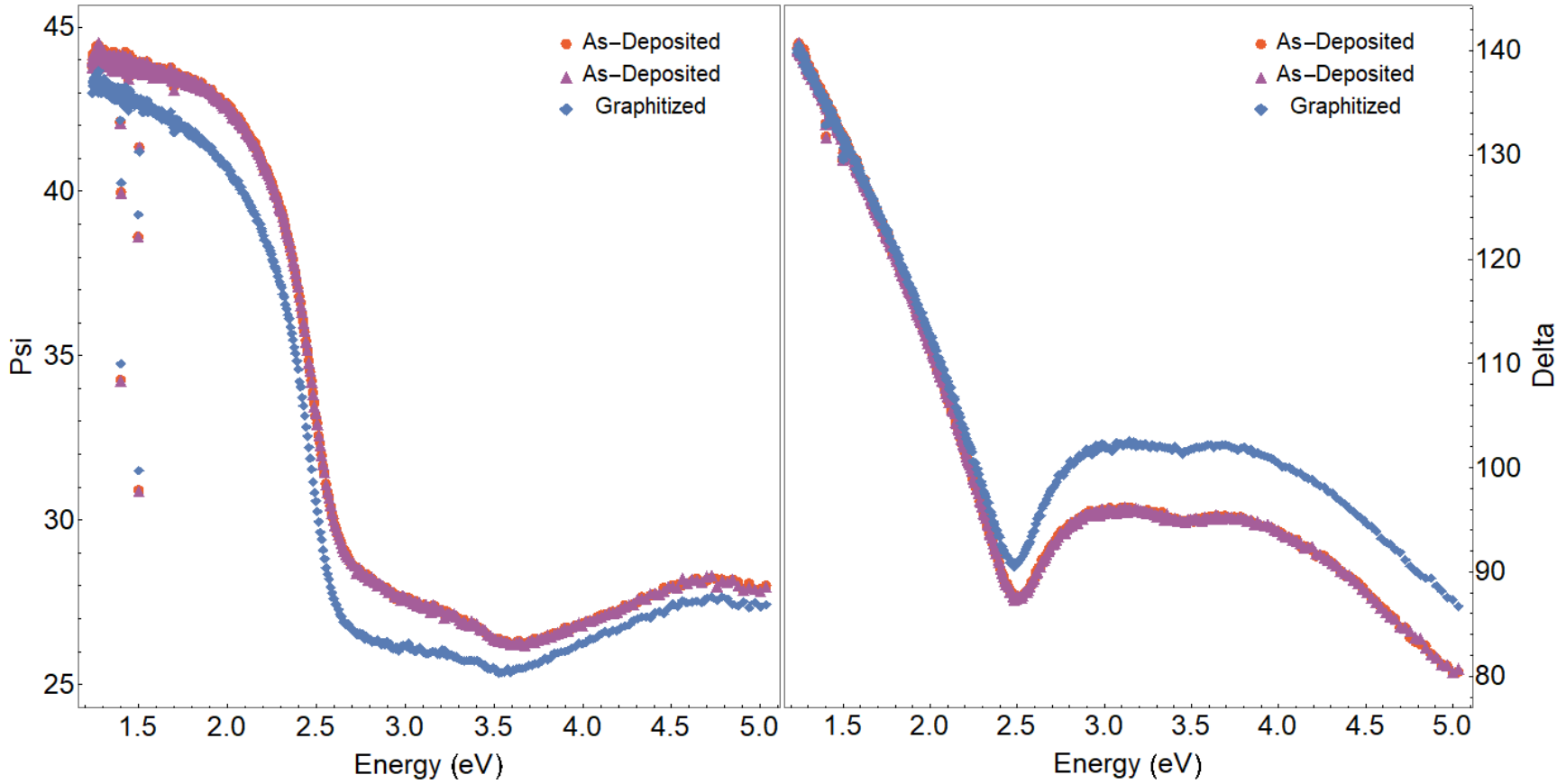

Figure 2. 7: (Left) psi and delta (right) values measured by SE and plotted as a function of energy for three different locations within a deposit with identical thickness (the latter determined by XPS). The red (circle) and purple (triangle) plots correspond to SE data taken from within as-deposited carbon regions while the blue (diamond) represents data taken from within a graphitized carbon region.

In CompleteEase™, this was performed by fitting a common B-spline curve to approximate the average optical response of the substrate from all 30 locations. The "goodness of the fit" was monitored using the "mean squared error" (χ^2). The mathematical details of this parameter can be found in the CompleteEase™ manual but, in essence, it sums (over all wavelengths) the differences between the measured and model predicted ellipsometry data (psi and delta)[41]. While an ideal model fit should provide a χ^2 equal to one, the best model fits for experimental datasets are generally higher. A $\chi^2 < 10$ is generally considered acceptable[41]. For the B-Spline fit to the substrate, an χ^2 of about 3.9 was found.

Although accurate optical / dielectric functions can readily be obtained for the substrate, for the ultrathin (< 10 nm) carbonaceous films under investigation in this study, it becomes increasingly difficult to separate the changes in psi and delta due to film thickness and those due to the dielectric functions of the film[48-49]. This can be explained, in part, by the significantly weaker signal from the film compared to the substrate. In chemically homogenous regions of deposits where there is a singular type of carbon (as determined by XPS), the dielectric parameters can, however, still be extracted/parameterized by assuming that the optical/dielectric parameters will remain constant while thickness changes. Under these circumstances, any changes in SE are determined by changes in film thickness. Consequently, the invariant optical/dielectric parameters and variable thickness values that provide the best fit to the SE data can be determined.

To this end, 30 locations were chosen within an as-deposited tetradecane deposit. Two different models were used to parameterize the dielectric functions of the as-deposited film, the Tauc-Lorentz and B-Spline. The multi-sample analysis feature in CompleteEase, (in conjunction with the experimentally determined dielectric coefficients for the substrate) was used to provide a simultaneous calculation of thickness (at each point) and determine (using either the Tauc-Lorentz

or B-spline model) a common set of dielectric functions for the as-deposited carbon[41]. To avoid unrealistic results with the B-spline model, both $\varepsilon_2 > 0$ and Kramers-Kronig consistency was enforced. The resulting χ^2 values were 3.9 and 3.4 for the Tauc-Lorentz and B-spline model, respectively. Using the same approach, 30 locations within the deposit that received 100 hours additional electron exposure were utilized to simultaneously determine both thickness (at each location) and dielectric functions for graphitized carbon. The χ^2's for the Tauc-Lorentz and B-Spline parametrization were 4.1 and 3.8, respectively.

Comparison of Film Thicknesses Determined by XPS and SE:

Film thicknesses, calculated by the multi-sample SE analysis described earlier, were compared to the corresponding thicknesses determined by XPS. Results from this analysis for both SE models (Tauc-Lorentz and B-Spline) and each type of carbon (as-deposited sp^3 and graphitized sp^2) are shown in Figure 2.8. Regardless of the type of carbon or model used, it is apparent that there is a linear correlation between XPS and SE predicted thicknesses. Moreover, the slopes for all these plots are close to unity, indicating a high degree of linear correlation. Both B-spline and TL models give relatively similar slopes for the same type of carbon, for as-deposited sp^3-like carbon (1.25 as compared to 1.21) and for graphitized carbon (0.89 as compared to 0.95). The slight deviations from unity are likely due to an inaccurate approximation of thickness by either technique. In the case of XPS, deviations can be the result of an inaccurate EAL. In the case of SE, deviations can be the result of an inaccurate approximation of the optical constants. The y-intercepts are the result of an offset calibration factor that deals with how thickness is calculated with respect to each technique. In general, Figure 2.8 highlights the good linear correlation between XPS and SE derived thickness values, suggesting that either method can be used to

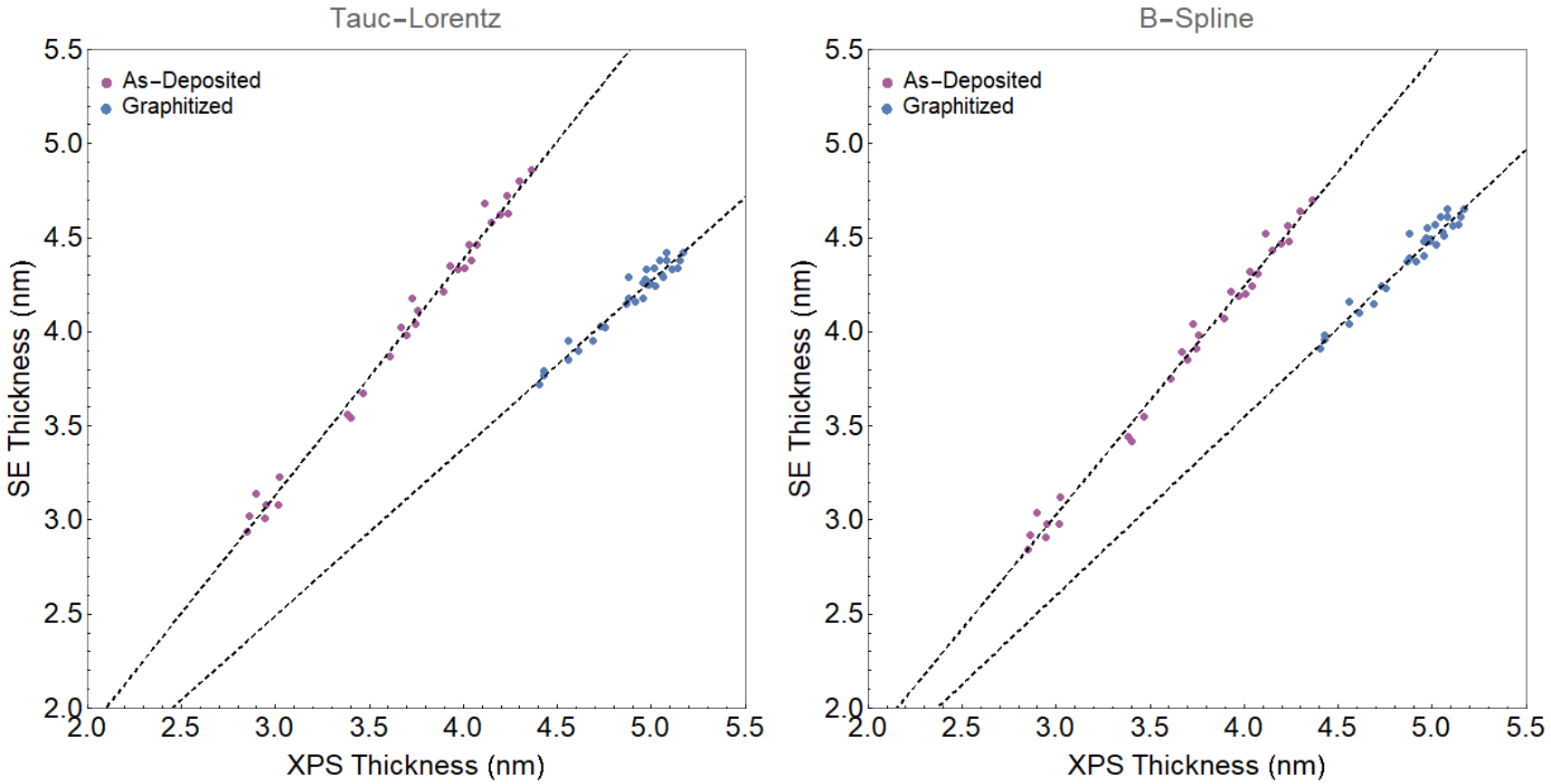

Figure 2. 8: (Left) correlation plot, pairing the film thicknesses determined by XPS (x-axis) and predicted by the Tauc-Lorentz SE model for as-deposited (purple) and graphitized (blue) carbon (SE data plotted on the y-axis). A linear fit gives a slope of 1.25 and 0.89 for as-deposited and graphitic carbon, respectively. (Right) Correlation plot, pairing the film thicknesses determined by XPS (x-axis) and predicted by the B-Spline SE model for as-deposited (blue) and graphitic (orange) carbon (SE data plotted on the y-axis). A linear fit gives a slope of 1.21 and 0.95 for as-deposited and graphitic carbon, respectively.

determine film thicknesses in nanometer scale carbonaceous films with a high degree of accuracy (error < ≈ 10 %). It is worth noting that, due to the ultra-thin nature of the films examined here, identification of the homogeneous regions, where each distinct form of carbon resides, is required for competent SE analysis. Consequently, XPS analysis provides an essential component that greatly improves the confidence with which SE analysis can be performed

Probing the electron induced transformations of carbon in more heterogeneous deposits:

Using the dielectric functions for as-deposited and graphitic carbon, an SE model can be constructed to account for more heterogeneous deposits where the extent of additional electron irradiation was insufficient to convert all of the as-deposited carbon to graphitized carbon. Experimentally, this insufficient exposure corresponds to deposits exposed to 1 hour and 21 hours of electron irradiation. For these more complex, heterogeneous films, the Bruggeman effective medium approximation (BEMA) was utilized to approximate the cumulative optical response of the film layer in the three-phase model. The independently derived dielectric functions for as-deposited and graphitized carbon, as determined by the B-spline model, were utilized to construct a two carbon BEMA model[47]. The optical parameters derived from the B-spline model were used due to the slightly better fit to the experimentally determined SE data (lower χ^2) as compared to the TL model. Using the two carbon BEMA model to approximate the optical coefficients of the film layer, the measured SE data was fit with the three-phase model to determine both thickness and the percent of graphitized carbon for both as-deposited and additionally dosed films. The χ^2 (MSE) values, plotted as a function of position (See Figure 2.9), were observed to be nearly constant (≈ 3.8) throughout the deposits, indicating a good fit for all variations in film thickness and composition.

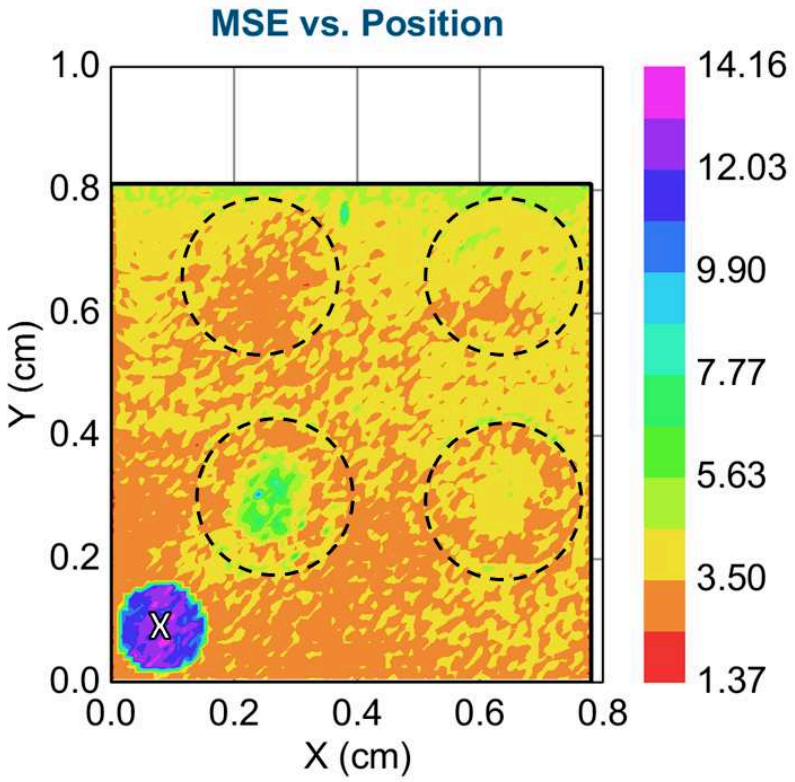

Figure 2. 9: Lateral SE map plotting the MSE ($\chi 2$) for the Bruggeman EMA model fits applied to a substrate with 4 amorphous carbon deposits; as-deposited tetradecane (top left), and deposits exposed to 1 hour, 21 hours, and 100 hours of additional electron exposure (bottom right, bottom left, and top right deposits, respectively). A black dashed line represents the anticipated location of deposits based on the beam profile. The deposit featured in the bottom left corner, demarcated by an "x", corresponds to a background deposit used to calibrate chamber cleanliness (See Experimental section for more details).

A comparison of the thickness maps acquired by XPS and SE for deposits exposed to varying degrees of post-deposition electron irradiation (1 hour, 21 hours, and 100 hours) is shown in Figure 2.10. The left-hand column shows the thickness maps obtained from XPS, while the middle column shows the thickness maps obtained from the SE BEMA model. Line profiles comparing the film thicknesses derived from these two experimental methods can be found in the graphs featured in the right column. In general, the two carbon BEMA model results in a good agreement between film thicknesses determined by SE and XPS (compare the blue circles and orange triangles) for all deposits. The modest disagreement observed in the center of the 100-hour line profile (Figure 2.10, bottom right) correlates with the additionally electron dosed region of the deposit and is a consequence of the B-Spline model's underestimation (compared to XPS) of graphitic carbon thicknesses. It should be noted that the lateral resolution for the XPS thickness maps was about ± 0.2 mm, much larger than their SE counterparts (± 0.05 mm). To enable direct comparison of SE and XPS thickness maps, the SE thickness maps were averaged across a ± (0.2 x 0.2) mm^2 area to mimic the resolution of the XPS data. (Examples of SE thickness maps before and after spatial averaging can be seen in Figure 2.11).

The effect that varying the dose of post deposition electron irradiation has on the distribution of as-deposited and graphitized carbon within deposits was also evaluated by SE and compared to XPS, the latter determined using the deconvolution method described in the XPS characterization section (2.1). To this end, the sp^2/sp^3 distribution of deposits that were exposed to 1 hour, 21 hours, and 100 hours of additional electron irradiation were compared. Results of this analysis by XPS and SE are shown in Figure 2.12. As the additional electron dose increases, the extent of graphitization (conversion of as-deposited tetradecane to graphitic carbon) is seen to increase systematically. In the density plots for graphitic carbon, this manifests itself as an

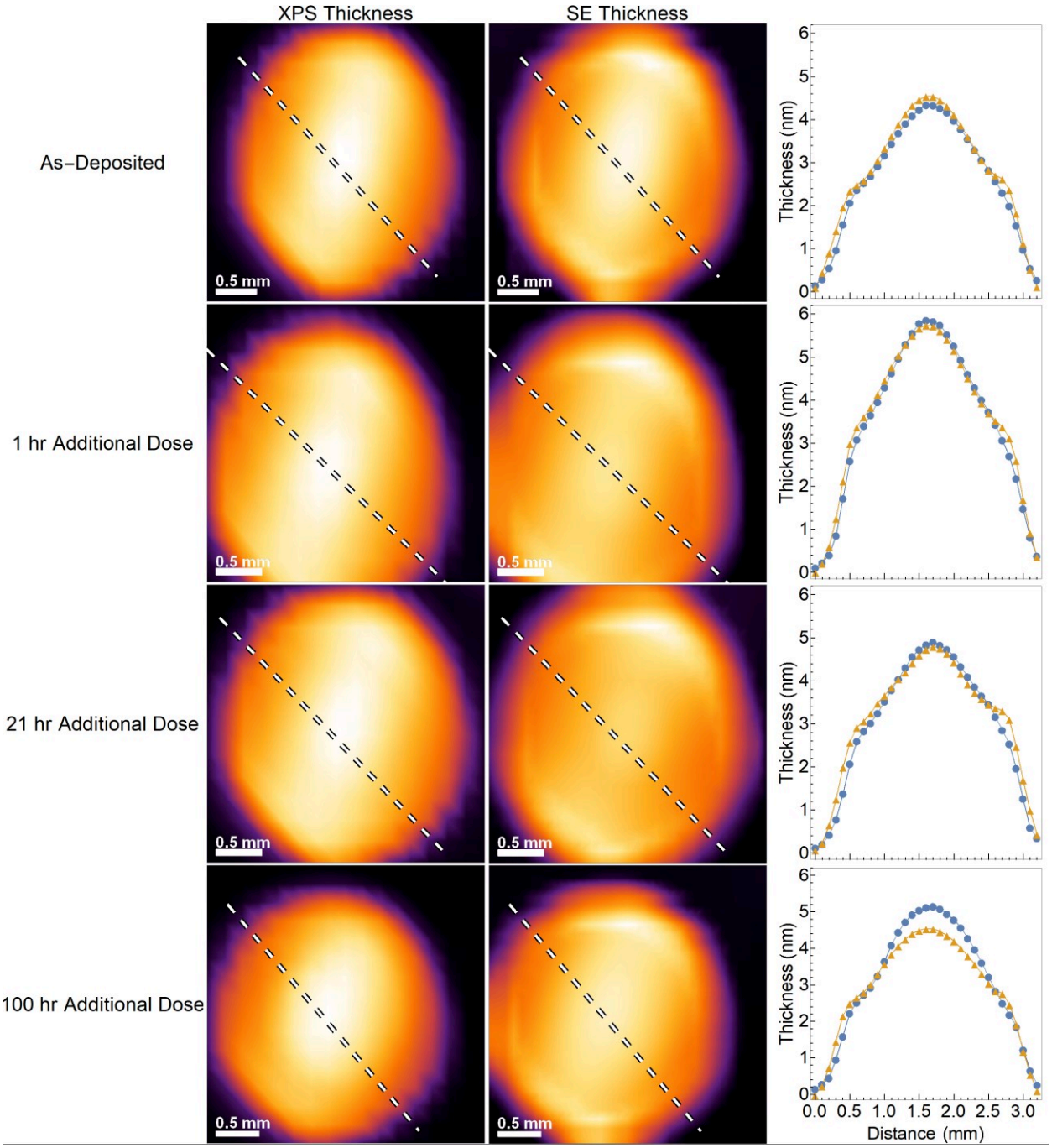

Figure 2. 10: XPS (left column) and BEMA SE (middle column) 2-dimensional thickness plots for both as-deposited films and films exposed to additional electron irradiation (see text for details). Line profiles across the corresponding deposits are plotted on the right with blue circles corresponding to the XPS thickness and orange triangles corresponding to SE thicknesses obtained using the BEMA model. The location of the line scan taken from each thickness plot is shown by the white dashed line.

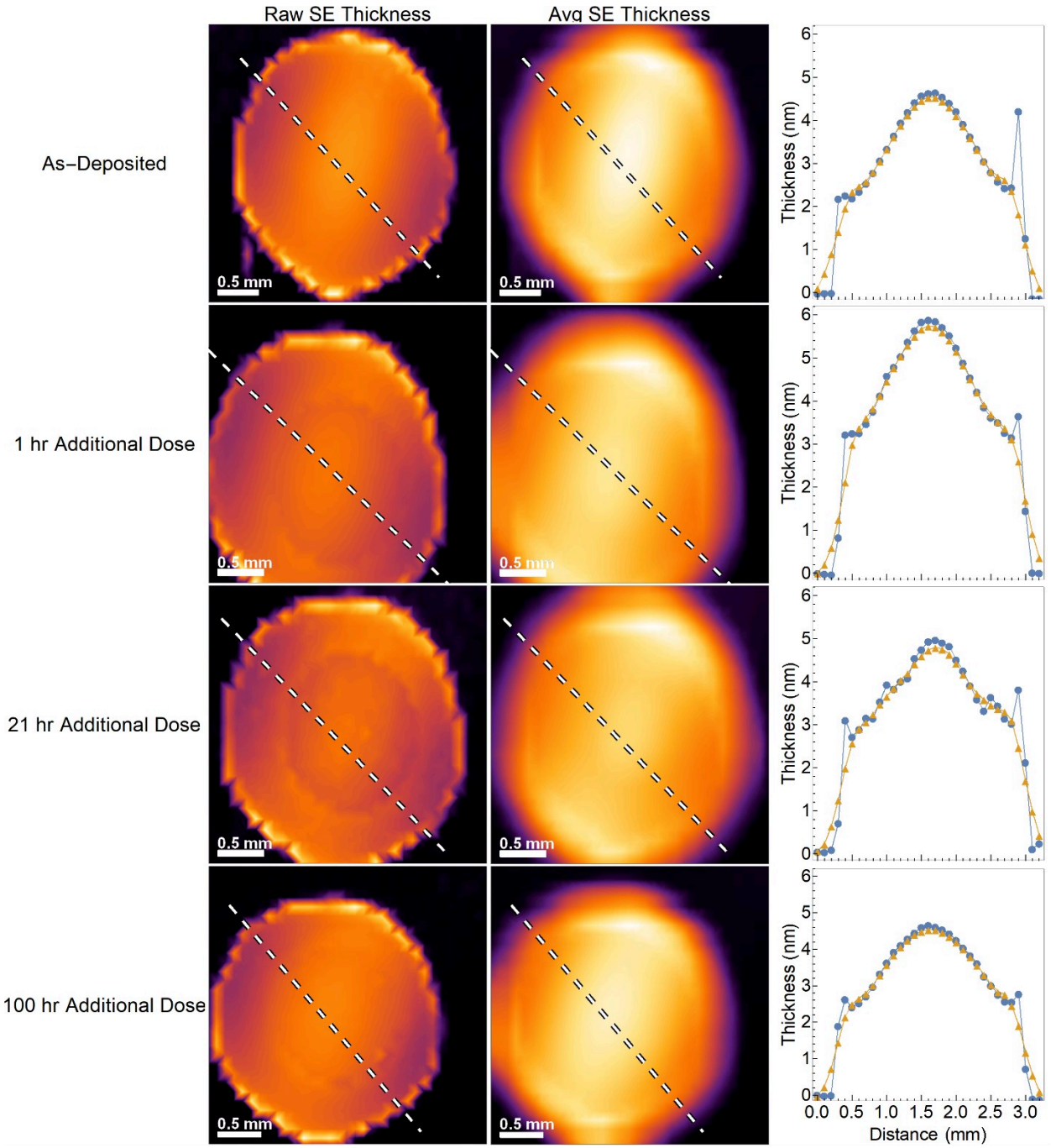

Figure 2. 11: Two-dimensional thickness plots determined from Bruggeman EMA SE analysis before (left column) and after (middle column) spatial averaging. Each column represents results obtained for as-deposited films (top column) and films exposed to additional electron irradiation (see text for details). Line profiles across the corresponding deposits are plotted on the right with blue circles corresponding to the BEMA SE thickness plots before spatial averaging and orange triangles corresponding to BEMA SE thickness plots after spatial averaging. The location of the line scan taken from each thickness plot is shown by the white dashed line.

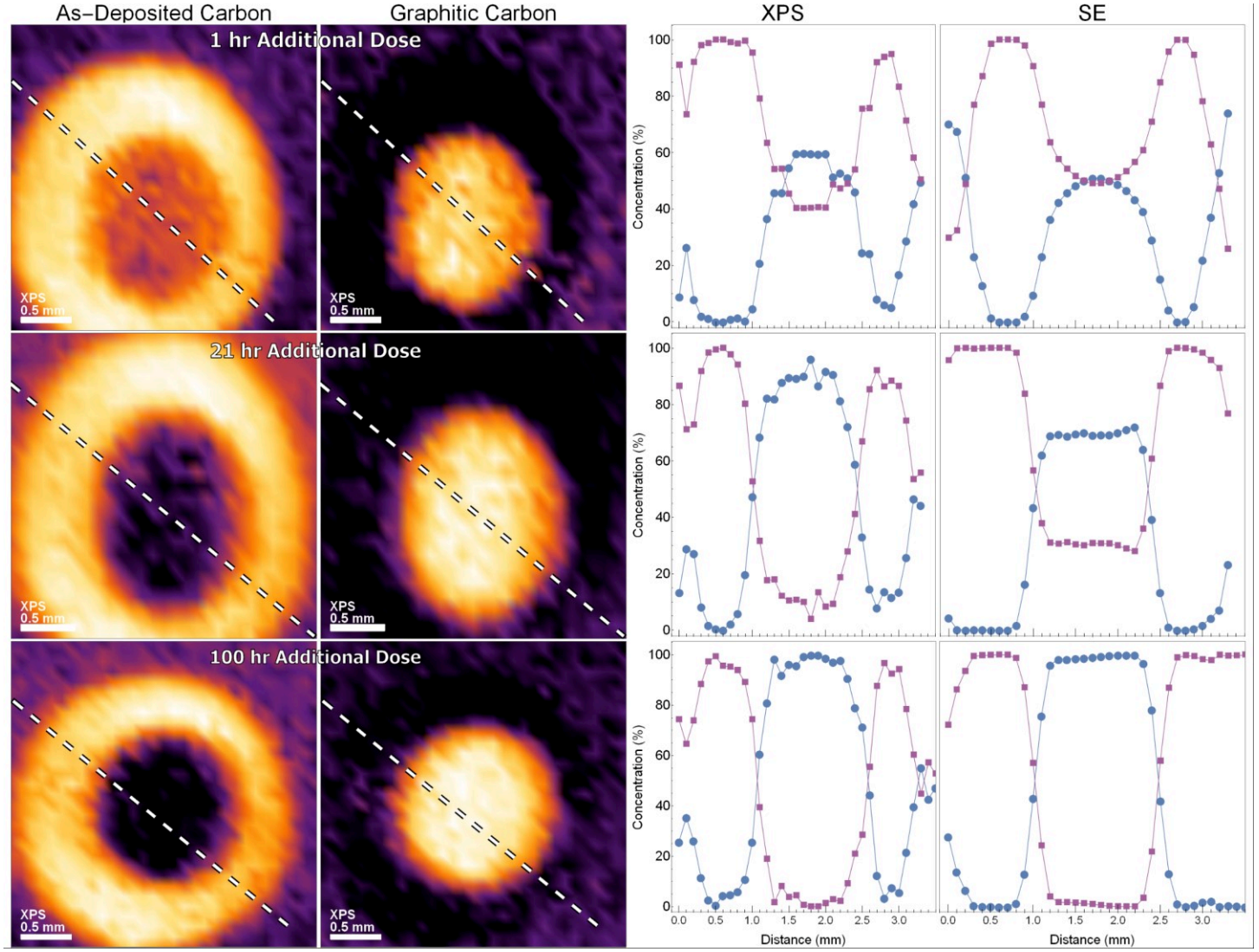

Figure 2. 12: (Left two columns) two-dimensional XPS C 1s component concentration maps showing the relative intensity of as-deposited carbon and graphitic carbon for deposits exposed to 1 hour (top row), 21 hours (middle row) and 100 hours (bottom row) of additional electron exposure. (Right two columns) Line profiles (dashed white lines) through the deposits showing the fractional concentration of as-deposited carbon (purple squares) and graphitic carbon (blue circles) determined by XPS and the BEMA SE model.

increasing whiteness in the central region where electron exposure occurred. For deposits exposed to only 1 hour of additional electron irradiation, data from both the XPS and BEMA SE model indicate that only about half the as-deposited carbon was converted to graphitized carbon (top right panel). After 21 hours of electron irradiation, the extent of graphitization increases and after 100 hours, the entire irradiated region has been converted to graphitized carbon. The lateral distribution of graphitic carbon for deposits where graphitization is not complete (i.e. 1 hour) exhibits a near gaussian profile across the deposit, consistent with the Gaussian-like intensity profile of the electron beam used to induce graphitization (see Figure 2.3). Figure 2.12 also highlights that the lateral distribution of graphitic carbon as measured by XPS and SE (using the BEMA model) agree well. Indeed, the similar sp^2/sp^3 distributions and thicknesses determined by XPS and BEMA SE model indicate the accuracy with which these techniques can be used to determine both thickness and film composition.

Characterization of films exposed to hydrogen atoms:

After XPS and SE characterization, each set of 4 deposits was exposed to hydrogen atoms (AH) for specific periods of time. After each AH exposure, XPS thickness maps were acquired and superimposed on top of the preceding map by adjusting the X/Y coordinates to maximize the correlation between the two thickness maps; the same technique used to compare the SE and XPS thickness maps. The thickness of carbon removed at any point within the deposit was calculated by measuring the change in the Au 4f XPS signal using equation (2.1). Figure 2.13 plots the carbon removed as a function hydrogen atom exposure for an as-deposited film (blue) as well as deposits where the central region had been exposed to 7 hours (red), 14 (green) hours, and 21 hours (orange) of additional electron irradiation. Examination of these plots shows that the rate of removal for as-

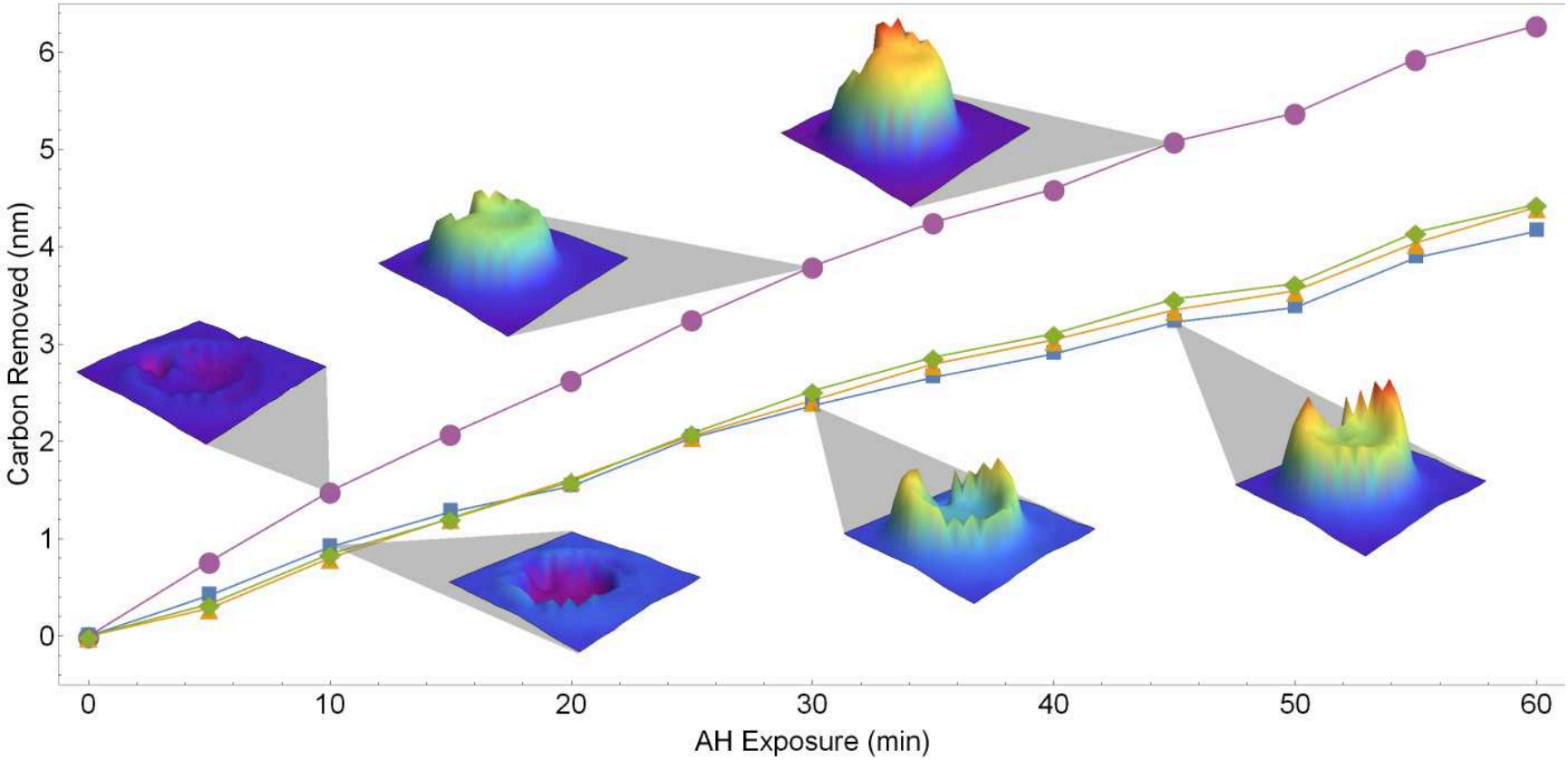

Figure 2. 13: Carbon etched as a function of hydrogen atom (AH) exposure, plotted for an as-deposited film (purple circle) as well as films where the central portion of the deposit was exposed to an additional 7 hours (green diamond), 14 hours (orange triangle) and 21 hours (blue square) of electron irradiation. Also shown are 3D XPS thickness maps representing the spatial distribution of carbon removed from as-deposited films and films where the central region was exposed to 21 hours of additional electron irradiation, after various AH exposures.

deposited tetradecane is higher than for carbon which had been exposed to additional electron irradiation. However, within deposits exposed to 7, 14 and 21 hours, there is little to no difference in the AH cleaning rate. A best fit line was applied to all data points (0 – 60 min) for each of the plots to obtain cleaning rates for each deposit; for the as-deposited tetradecane a value of 0.102 nm/min was determined while the slopes for the deposits exposed to 7, 14 and 21 hours were 0.074 nm/min, 0.072 nm/min, and 0.067 nm/min, respectively. The coefficient of determination (R^2) was determined to be ≈ 0.99 for all of the associated fits.

AH exposure studies have shown that amorphous carbon films are etched by an Eley-Rideal reaction[58-60]. Moreover, the rate of carbon removal using AH has been shown to be a first order process[53, 58, 61]. However, due to the limited penetration depth of hydrogen atoms within carbonaceous deposits, a pseudo-zeroth order reaction is observed when the film thickness is larger than the depth of AH penetration[52]. When this happens, the concentration of accessible/removable carbon can be considered constant, manifesting as a linear reduction in film thickness and a constant cleaning rate, as we observe experimentally. The etching rates (slopes) observed in Figure 2.13 show that hydrogenated (as-deposited, sp^3) films clean at a higher rate than graphitic carbon (additionally dosed, sp^2) films.

As expected, areas not exposed to additional electron irradiation (at the periphery of the deposit) cleaned at the same rate as the as-deposited tetradecane deposits. This results in contrasting cleaning rates within the central region of the deposits, where they were exposed to additional radiation. The effects of this differential in cleaning rates can be visualized in the 3D maps found in Figure 2.13. The top set of 3D figures correspond to a deposit that did not receive any additional electron dose. As a result, carbon is removed at an equal rate across the deposit giving rise to a nearly flat top distribution of carbon removed after 30 minutes of AH exposure.

This is in stark contrast to deposits exposed to additional electron irradiation which show reduced cleaning rates within the electron exposed regions. This manifests as a volcano-like carbon loss profile after both 30 and 45 minutes of AH exposure. It is worth noting the carbon loss profiles after 15 minutes of AH exposure. These profiles are visually dominated by the removal of the small amount of background carbon outside the deposit region, which occurs at a faster rate than either the as-deposited or graphitized carbon. These 3D maps illustrate the variance in cleaning rates that can be seen within the deposits themselves for the three different forms of carbon identified by XPS (background, as-deposited, and graphitized). The different cleaning rates measured at several locations in and around a deposit (corresponding to the different forms of carbon) are plotted in Figure 2.14.

After 60 minutes of AH exposure, both XPS and SE analysis was performed on the remaining deposit. At this point, according to XPS thickness maps, most of the carbon had been removed. For as-deposited films XPS analysis revealed no difference (other than signal intensity) between the C 1s spectral envelopes before and after 60 minutes of AH exposure. This contrasts with results from portions of the film exposed to additional electron doses. Figure 2.15 shows example C 1s XPS spectra for as-deposited carbon (top spectrum), graphitized carbon generated by exposing as-deposited carbon to 100 hours of electron irradiation (middle) and the same graphitized carbon after 60 minutes exposure to AH (bottom). Analysis of Figure 2.15 shows that the largely symmetric C 1s envelope of the graphitized carbon has been transformed by AH exposure to an asymmetric peak centered around 285.1 eV (compare the middle and bottom C 1s spectra in Figure 2.15). Other than a slightly higher binding energy (by ≈ 0.1 eV) this new peak shape is identical to the hydrogenated sp^3 carbon species observed in the as-deposited film (compare the top and bottom C 1s spectra in Figure 2.15).

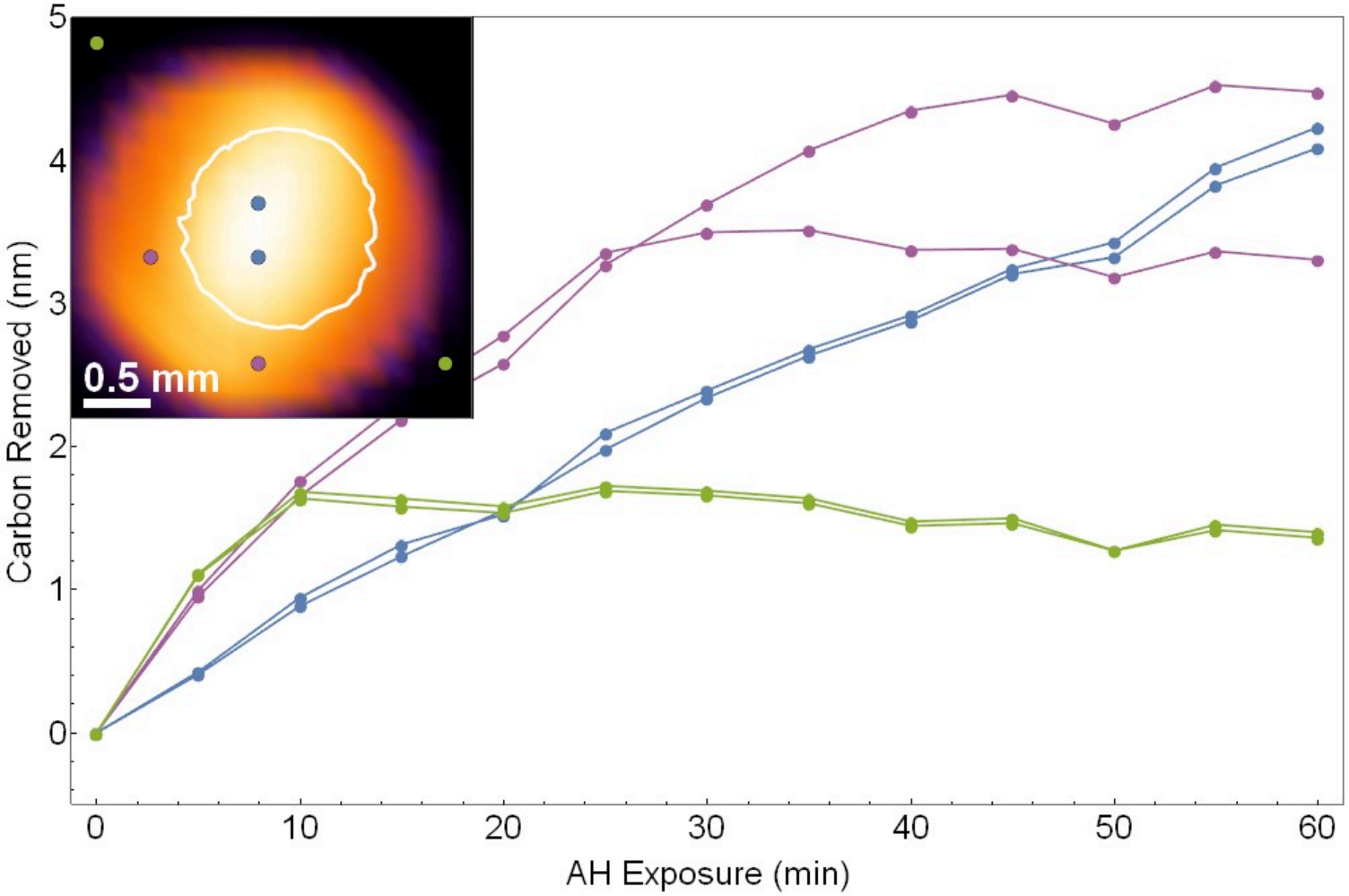

Figure 2. 14: Carbon etched as a function of atomic hydrogen exposure, plotted for three different types of carbon atoms found in and around a deposit where the central portion (demarcated by a white line was exposed to additional electron irradiation). The inset featured at the top right of the plot illustrates the location where each measurement was taken; with blue corresponding to carbon atoms in the center of the deposit that were exposed to additional electron irradiation, purple corresponding to as-deposited carbon, and green corresponding to background carbon outside of the deposit.

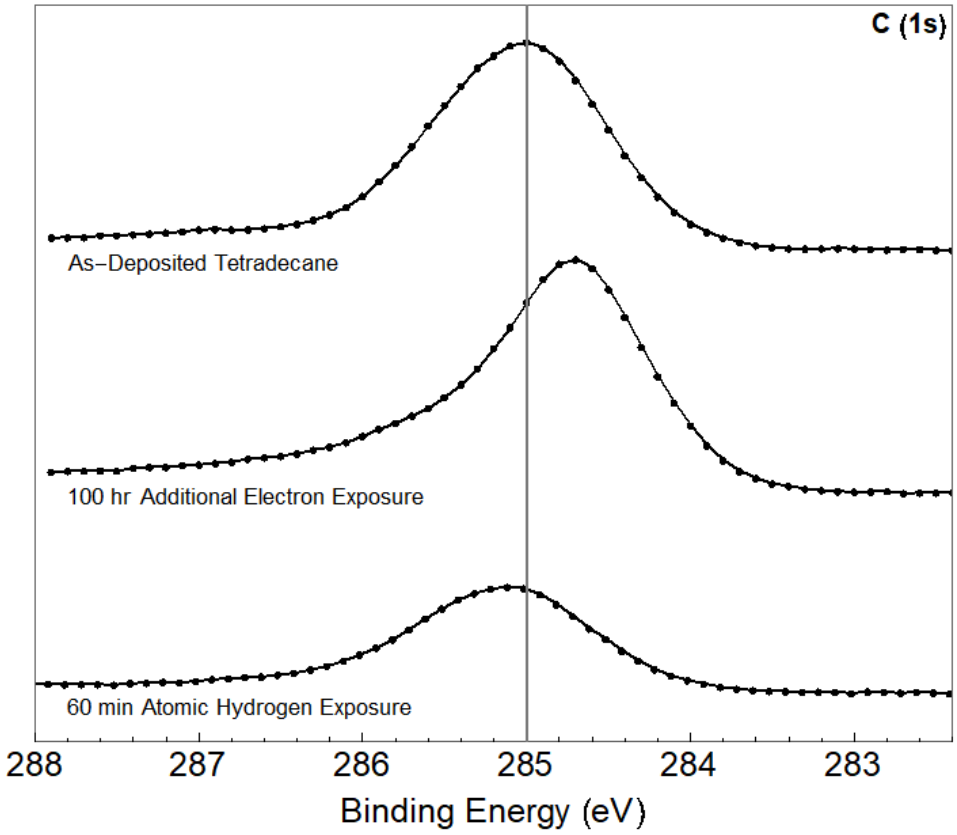

Figure 2. 15: C 1s XPS spectra taken from films of as-deposited carbon (top), graphitized carbon formed after exposing an as-deposited film to 100 hours of additional electron irradiation (middle), and after exposing graphitized carbon to 60 mins of hydrogen atoms (bottom). A gray line at 285.0 eV is used as a guide to help illustrate the binding energy shifts.

Previous SE, Raman and ATR-FTIR studies on amorphous carbon films show that hydrogen atom etching occurs as a direct result of film hydrogenation[27, 60]. These studies, performed by Jariwala et al., indicate that hydrogenation primarily occurs at graphitic sp^2 sites converting them to more hydrogenated sp^3 CH_x sites[24, 27, 60, 62]. In Figure 2.15, the binding energy shift C 1s peak from 284.7 eV (graphitic, sp^2) to a more hydrogenated (sp^3) species at 285.1 eV supports the idea that AH exposure leads to the conversion of graphitized to hydrogenated sp^3 carbon, the latter analogous to the as-deposited carbon. Further progression results in the production of C_xH_y volatile species and the eventual etching of the carbonaceous film. It can be inferred then, that the reduced etch rated observed for graphitic (sp^2) films compared to hydrogenated (sp^3) is the result of the additional sp^2 to sp^3 hydrogenation step needed before etching[24, 27, 60, 62].

SE data, at least qualitatively, supports the XPS findings. The blue and purple plots in Figure 2.16 show raw SE data taken from two locations of identical thickness (according to XPS) but different doses of additional electron exposure. As expected, the variation in the distribution of sp^2/sp^3 species between these different locations results in differences between psi and delta. In contrast, after 60 minutes of AH exposure (Figure 2.16, Orange/Brown) all of the locations with identical thicknesses, determined by XPS, exhibit identical SE signals, indicative of the presence of a single carbon (sp^3) species.

It should be noted that the present study focused on the analysis of relatively large millimeter sized deposits. This was dictated by the limitations of the electron gun. In principle, however, the approach adopted in the present study could also be applied to analyze deposits of significantly smaller size. In this regard lateral resolutions would only be limited by the spot size of ellipsometer, 25 um x 60 um.

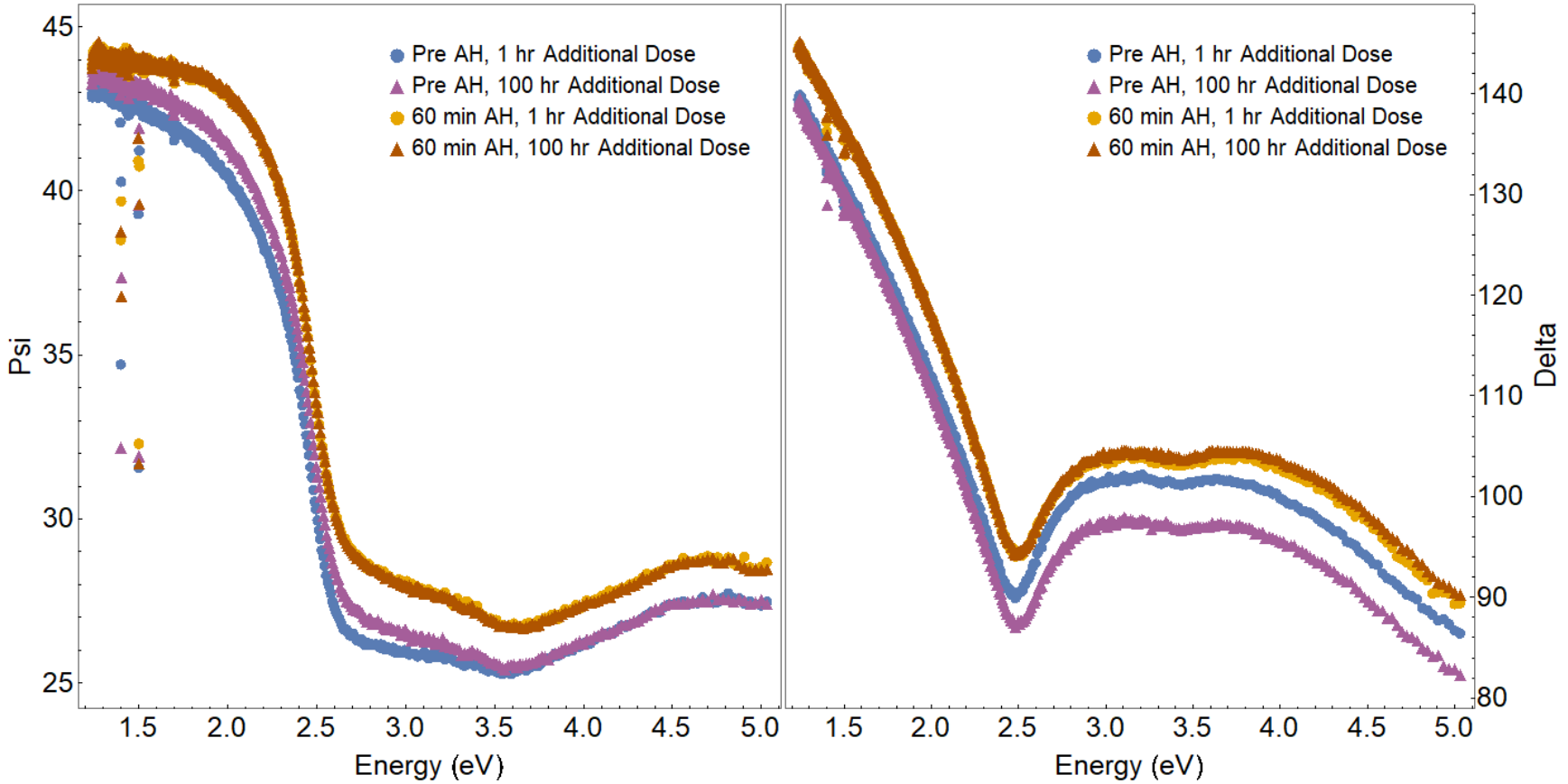

Figure 2. 16: (Left) psi and delta (right) values measured by SE and plotted as a function of photon energy taken from two locations of identical thickness (as determined by XPS) but exposed to different electron doses (1 hour (circles) and 100 hour (triangles). Data is shown for paired locations, before (blue (circles)/purple (triangles)) and after (orange (circles)/brown (triangles)) 60 minutes of hydrogen atom exposure.

2. 4. Conclusions

Electron beam induced deposition of tetradecane has been used to create ~ 6 nm amorphous carbon films. XPS and SE maps of the C 1s spectral regions revealed that electron irradiation of the deposited films resulted in the conversion of carbon from a hydrogenated, sp^3-like species into a graphitized, sp^2-like species. Based on corresponding attenuation of the Au 4f intensity, this transformation did not, however, change the overall thickness of the film. Spectroscopic ellipsometry demonstrated that this electron induced dehydrogenation process also produced measurable changes in the dielectric and optical properties of the film. Exposing the graphitized sp^2-like carbon atoms to hydrogen atoms (AH) caused them to convert back to a more hydrogenated sp^3-like species. The need to convert sp^2 to sp^3 carbon atoms as a discrete step on the way to forming volatile carbon species is believed to be responsible for the observed decrease in AH etching rate of sp^2 vs sp^3 carbon atoms.

As part of this study, protocols were developed to analyze this conversion of as-deposited sp^3-like carbon to graphitic sp^2-like carbon, particularly in situations where regions of the deposits contained a mixture of both species. For XPS, this protocol utilized linear combinations of the individual C 1s lineshapes associated with as-deposited sp^3 and graphitized sp^2 carbon atoms. For SE, the first step in this protocol involved obtaining the optical / dielectric functions for each carbon species independently; a step that could not be possible without XPS's identification of the pure (as-deposited and graphitic carbon) regions within the deposits. In conjunction with a Bruggeman effective medium approximation, this information enabled the ratio of sp^3/sp^2 carbon atoms as well as the film's thickness to be mapped. The good agreement between composition and thickness maps obtained by XPS and SE indicates the efficacy of both techniques in terms of their

ability to follow the interconversion between as-deposited sp^3 and graphitic sp^2 carbon in ultra-thin carbonaceous deposits exposed to electron irradiation and hydrogen atoms.

2. 5. Acknowledgements

DHF thanks the National Science Foundation for partial support of this work through the linked collaborative grants CHE-1607621 and CHE-1607547. MB thanks the National Institute of Standards and Technology for use of their equipment as well as J.A. Woolam for their guidance in interpreting spectroscopic ellipsometry data.

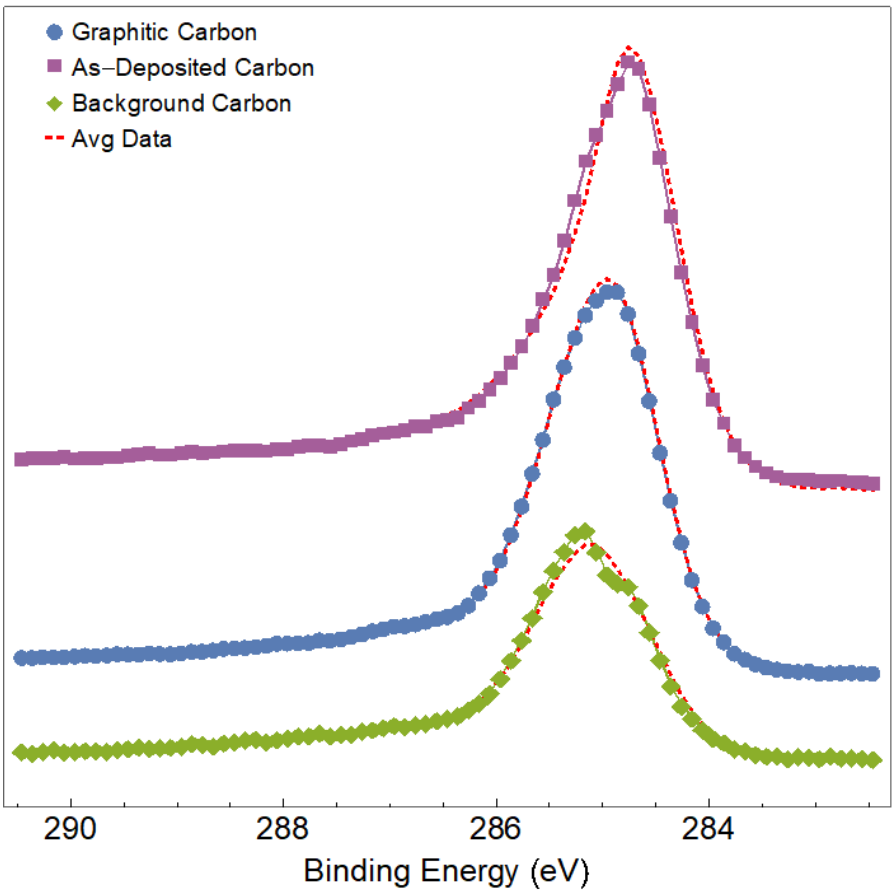

SI Figure 2. 1: Raw C 1s XPS data take from an as-deposited carbon region (purple squares), carbon atoms within the deposit exposed to 100 hour additional electron irradiation (blue circles), and carbon atoms outside of the deposit (background carbon) (green diamond). The red dotted lines correspond to the averaged C 1s XPS data acquired from each region.

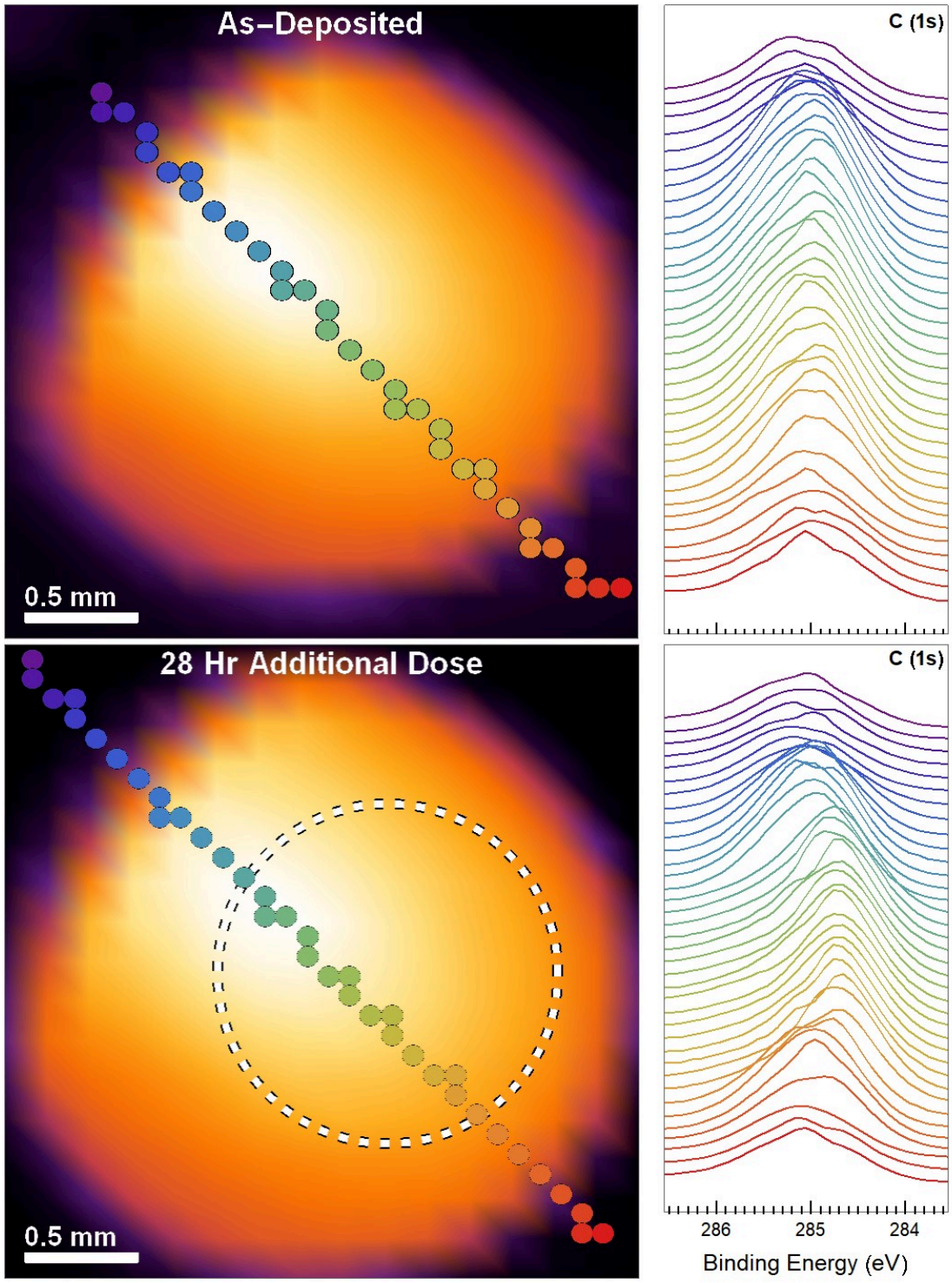

SI Figure 2. 2: (Left column) XPS thickness plots for (top row) a deposit which was not exposed to any post-deposition electron irradiation and (bottom row) one where the central region was exposed to an additional 28 hours of electron irradiation (the dashed white circle demarcates the region exposed to additional electron irradiation). (Right column) Raw C 1s XPS data taken from various locations within both deposits, color matched to the dots in their corresponding XPS thickness plots.

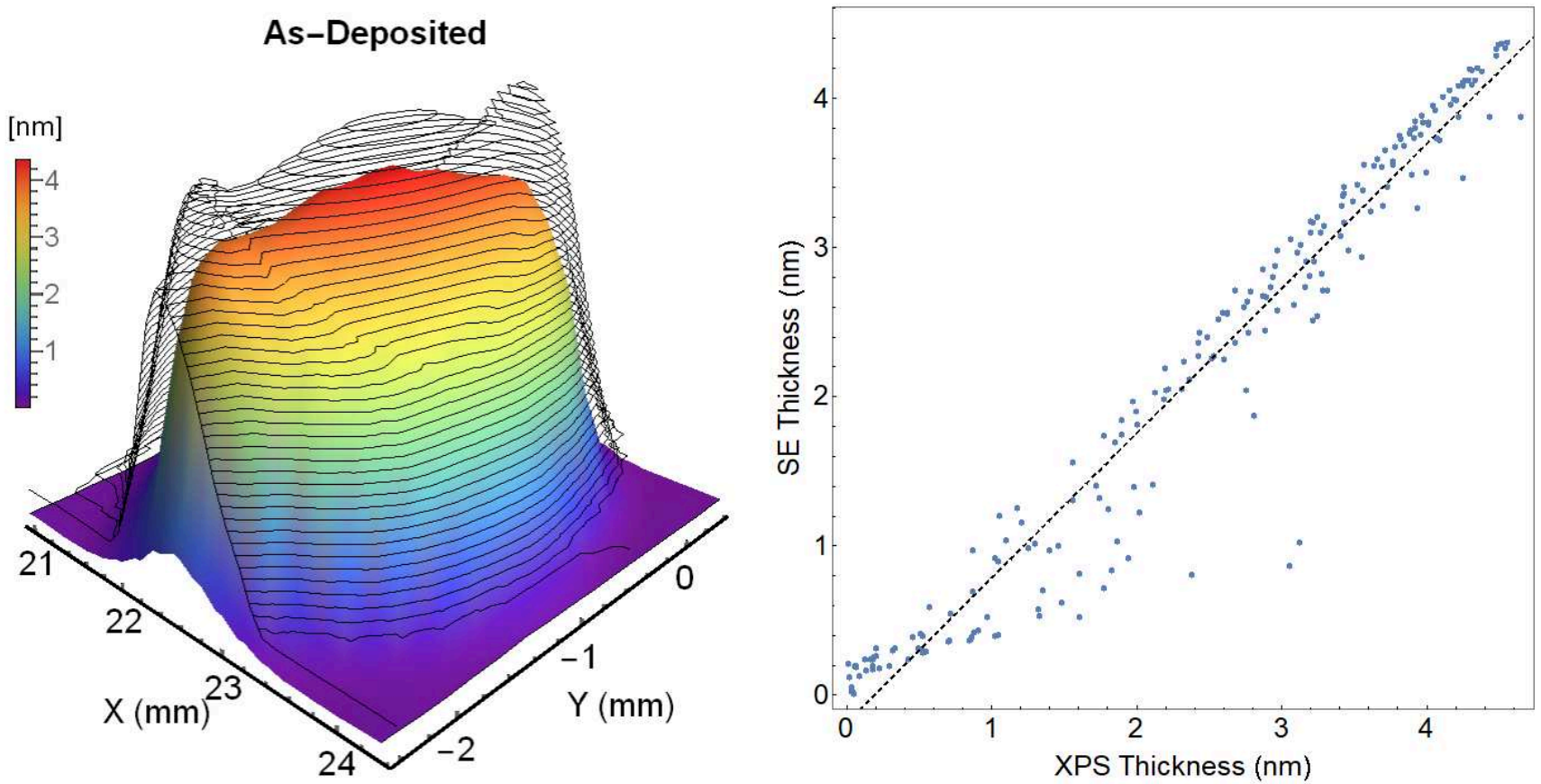

SI Figure 2. 3: Bruggeman EMA SE and XPS thickness data for an as-deposited tetradecane deposit. (Left) 3D color map showing XPS thickness with a superimposed wireframe plotting the Bruggeman EMA SE thickness, both plotted as a function of position within the deposit. (Right) Correlation plot, comparing the XPS (x-axis) and Bruggeman EMA SE (y-axis) thickness measured at each point within the deposit. The correlation between the thickness values determined by both techniques is 0.970 as determined by the gradient.

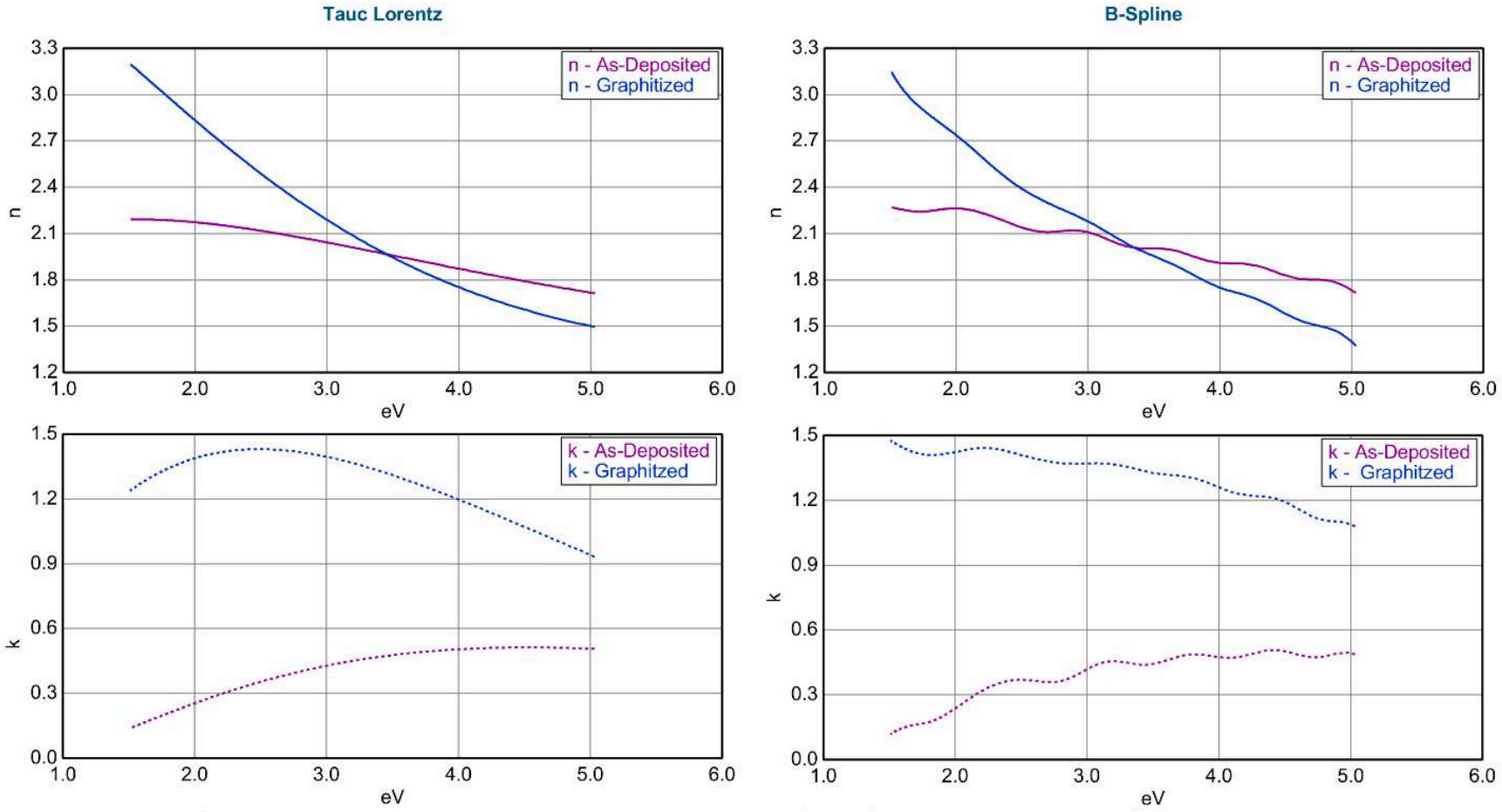

SI Figure 2. 4: Plots showing the optical constants n (top panels, solid lines) and k (bottom panels, dashed lines) as a function of energy (eV) predicted by both the Tauc-Lorentz (left panels) and B-Spline (right panels) for both as-deposited (purple) and graphitized (blue) carbon.

2. 6. References

1. Lu, W.; Komvopoulos, K., Nanotribological and Nanomechanical Properties of Ultrathin Amorphous Carbon Films Synthesized by Radio Frequency Sputtering. *Journal of Tribology* **2000,** *123* (3), 641-650.
2. Han, Y. S.; Yu, J.-S.; Park, G. S.; Lee, J. Y., *Effects of Synthesis Temperature on the Electrochemical Characteristics of Pyrolytic Carbon for Anodes of Lithium-Ion Secondary Batteries*. 1999; Vol. 146, p 3999-4004.
3. Liu, J.; Mirri, F.; Notarianni, M.; Pasquali, M.; Motta, N., High performance all-carbon thin film supercapacitors. *Journal of Power Sources* **2015,** *274*, 823-830.
4. Maruyama, J.; Yamamoto, M.; Hasegawa, T.; Iwasaki, S.; Siroma, Z.; Mineshige, A., *Carbonaceous thin film coated on nanoparticle as fuel cell catalyst formed by one-pot hybrid physical–chemical vapor deposition of iron phthalocyanine*. 2013; Vol. 90, p 366-374.
5. Zhou, Z.; Zhao, X. S.; Zeng, X. T., Surface patterning with carbon thin films by nanosphere lithography. *Surface and Coatings Technology* **2005,** *198* (1), 178-183.
6. B. Hill, S.; Ermanoski, I.; Grantham, S.; Tarrio, C.; Lucatorto, T.; E. Madey, T.; Bajt, S.; Chandhok, M.; Yan, P.; Wood, O.; Wurm, S.; V. Edwards, N., *EUV testing of multilayer mirrors: Critical issues*. 2006; Vol. 6151.
7. Arumainayagam, C. R.; Lee, H.-L.; Nelson, R. B.; Haines, D. R.; Gunawardane, R. P., Low-energy electron-induced reactions in condensed matter. *Surface Science Reports* **2010,** *65* (1), 1-44.
8. Shuji, K.; Hideaki, T.; Katsumi, M., Microfabrication of diamond films by localized electron beam chemical vapour deposition. *Semiconductor Science and Technology* **2002,** *17* (10), 1096.
9. Utke, I.; Hoffmann, P.; Dwir, B.; Leifer, K.; Kapon, E.; Doppelt, P., Focused electron beam induced deposition of gold. *Journal of Vacuum Science & Technology B: Microelectronics and Nanometer Structures Processing, Measurement, and Phenomena* **2000,** *18* (6), 3168-3171.
10. Koops, H. W. P.; Schössler, C.; Kaya, A.; Weber, M., Conductive dots, wires, and supertips for field electron emitters produced by electron-beam induced deposition on samples having increased temperature. *Journal of Vacuum Science & Technology B: Microelectronics and Nanometer Structures Processing, Measurement, and Phenomena* **1996,** *14* (6), 4105-4109.
11. Budaev, V. P.; Khimchenko, L. N., Fractal growth of deposited films in tokamaks. *Physica A: Statistical Mechanics and its Applications* **2007,** *382* (2), 359-377.
12. Jacob, W., Surface reactions during growth and erosion of hydrocarbon films. *Thin Solid Films* **1998,** *326* (1), 1-42.
13. Ennos, A. E., The sources of electron-induced contamination in kinetic vacuum systems. *British Journal of Applied Physics* **1954,** *5* (1), 27.
14. Mitura-Nowak, M.; Karczmarska, A.; Marczewska, B.; Marszalek, M., *TL characterization of CVD diamond films deposited at different growth parameters*. 2013; Vol. 9, p 210.
15. Knapp, Q. W.; Wren, J. C., Film formation on type-316L stainless steel as a function of potential: Probing the role of gamma-radiation. *Electrochimica Acta* **2012,** *80*, 90-99.
16. Avasthi, D. K., Effects and uses of ion beams with diamond, DLC and fullerene films. *Vacuum* **1996,** *47* (11), 1249-1258.
17. Silinskas, M.; Grigonis, A., Low energy post-growth irradiation of amorphous hydrogenated carbon (a-C:H) films. *Diamond and Related Materials* **2002,** *11* (3), 1026-1030.
18. Xu, C.; Koel, B. E., Electron-induced dissociation of hydrocarbon multilayers. *Surface Science Letters* **1993,** *292* (1), A601.
19. Martin, A. A.; Filevich, J.; Straw, M.; Randolph, S.; Botman, A.; Aharonovich, I.; Toth, M., Radiation-Induced Damage and Recovery of Ultra-Nanocrystalline Diamond: Toward Applications in Harsh Environments. *ACS Applied Materials & Interfaces* **2017,** *9* (45), 39790-39794.

20. Zharnikov, M.; Geyer, W.; Gölzhäuser, A.; Frey, S.; Grunze, M., Modification of alkanethiolate monolayers on Au-substrate by low energy electron irradiation: Alkyl chains and the S/Au interface. *Physical Chemistry Chemical Physics* **1999,** *1* (13), 3163-3171.
21. Wnuk, J. D.; Gorham, J. M.; Rosenberg, S. G.; van Dorp, W. F.; Madey, T. E.; Hagen, C. W.; Fairbrother, D. H., Electron Induced Surface Reactions of the Organometallic Precursor Trimethyl(methylcyclopentadienyl)platinum(IV). *The Journal of Physical Chemistry C* **2009,** *113* (6), 2487-2496.
22. B. Hill, S.; Faradzhev, N.; Richter, L.; Grantham, S.; Tarrio, C.; Lucatorto, T.; Yulin, S.; Schürmann, M.; Nesterenko, V.; Feigl, T., *Optics contamination studies in support of high-throughput EUV lithography tools*. 2011; Vol. 7969.
23. Grantham, S.; Tarrio, C.; B. Hill, S.; Richter, L.; Lucatorto, T.; van Dijk, J.; Kaya, C.; Harned, N.; Hoefnagels, R.; Silova, M.; Steinhoff, J., *The NIST EUV facility for advanced photoresist qualification using the witness-sample test*. 2011; Vol. 7969.
24. Biener, J.; Schubert, U. A.; Schenk, A.; Winter, B.; Lutterloh, C.; Küppers, J., A surface reaction with atoms: Hydrogenation of sp- and sp2-hybridized carbon by thermal H(D) atoms. *The Journal of Chemical Physics* **1993,** *99* (4), 3125-3128.
25. Jellison, G. E.; Geohegan, D. B.; Lowndes, D. H.; Puretzky, A. A.; Merkulov, V. I., Characterization of Pulsed-Laser Deposited Amorphous Diamond Films by Spectroscopic Ellipsometry. *MRS Proceedings* **2011,** *526*, 349.
26. Jellison, G. E.; Merkulov, V. I.; Puretzky, A. A.; Geohegan, D. B.; Eres, G.; Lowndes, D. H.; Caughman, J. B., Characterization of thin-film amorphous semiconductors using spectroscopic ellipsometry. *Thin Solid Films* **2000,** *377-378*, 68-73.
27. Jariwala, B. N.; Ciobanu, C. V.; Agarwal, S., Atomic hydrogen interactions with amorphous carbon thin films. *Journal of Applied Physics* **2009,** *106* (7), 073305.
28. Díaz, J.; Paolicelli, G.; Salvador, F.; Comin, F., *Separation of the sp3 and sp2 components in the C1s photoemission spectra of amorphous carbon films*. 1996; Vol. 54, p 8064-8069.
29. Kaciulis, S., Spectroscopy of carbon: from diamond to nitride films. *Surface and Interface Analysis* **2012,** *44* (8), 1155-1161.
30. Berger, S. D.; McKenzie, D. R.; Martin, P. J., EELS analysis of vacuum arc-deposited diamond-like films. *Philosophical Magazine Letters* **1988,** *57* (6), 285-290.
31. Zemek, J.; Houdkova, J.; Jiricek, P.; Jelinek, M., Surface and in-depth distribution of sp2 and sp3 coordinated carbon atoms in diamond-like carbon films modified by argon ion beam bombardment during growth. *Carbon* **2018,** *134*, 71-79.
32. Haerle, R.; Riedo, E.; Pasquarello, A.; Baldereschi, A., *Sp2/sp3 hybridization ratio in amorphous carbon from C 1s core-level shifts: X-ray photoelectron spectroscopy and first-principles calculation*. 2002; Vol. 65.
33. Barlow, A. J.; Popescu, S.; Artyushkova, K.; Scott, O.; Sano, N.; Hedley, J.; Cumpson, P. J., Chemically specific identification of carbon in XPS imaging using Multivariate Auger Feature Imaging (MAFI). *Carbon* **2016,** *107*, 190-197.
34. Lascovich, J. C.; Giorgi, R.; Scaglione, S., Evaluation of the sp2/sp3 ratio in amorphous carbon structure by XPS and XAES. *Applied Surface Science* **1991,** *47* (1), 17-21.
35. Jackson, S. T.; Nuzzo, R. G., Determining hybridization differences for amorphous carbon from the XPS C 1s envelope. *Applied Surface Science* **1995,** *90* (2), 195-203.
36. Chu, P. K.; Li, L., Characterization of amorphous and nanocrystalline carbon films. *Materials Chemistry and Physics* **2006,** *96* (2), 253-277.
37. Ferrari, A. C.; Robertson, J., Resonant Raman spectroscopy of disordered, amorphous, and diamondlike carbon. *Physical Review B* **2001,** *64* (7), 075414.

38. Wokaun, A., B. Schrader: Infrared and Raman Spectroscopy - Methods and Applications. VCH, Weinheim, 1995, DM 298,-, ISBN 3-527-26446-9. *Berichte der Bunsengesellschaft für physikalische Chemie* **1996,** *100* (7), 1268-1268.
39. Weber, J. W.; Hansen, T. A. R.; Sanden, M. C. M. v. d.; Engeln, R., B-spline parametrization of the dielectric function applied to spectroscopic ellipsometry on amorphous carbon. *Journal of Applied Physics* **2009,** *106* (12), 123503.
40. Tompkins, H. G.; Hilfiker, J. N., *Spectroscopic Ellipsometry: Practical Application to Thin Film Characterization*. Momentum Press: 2015.
41. *Complete Ease™ Software Manual*. J. A. Woolam Co., Inc. : 2011; Vol. Verson 4.63.
42. Fujiwara, H., *Spectroscopic Ellipsometry: Principles and Applications*. Wiley: 2007.
43. Johs, B.; Hale, J. S., Dielectric function representation by B-splines. *physica status solidi (a)* **2008,** *205* (4), 715-719.
44. Jr., G. E. J.; Modine, F. A., Parameterization of the optical functions of amorphous materials in the interband region. *Applied Physics Letters* **1996,** *69* (3), 371-373.
45. Jr., G. E. J.; Modine, F. A., Erratum: ''Parameterization of the optical functions of amorphous materials in the interband region'' [Appl. Phys. Lett. 69, 371 (1996)]. *Applied Physics Letters* **1996,** *69* (14), 2137-2137.
46. Logothetidis, S.; Petalas, J.; Ves, S., The optical properties of a-C:H films between 1.5 and 10 eV and the effect of thermal annealing on the film character. *Journal of Applied Physics* **1996,** *79* (2), 1040-1050.
47. Logothetidis, S., Hydrogen-free amorphous carbon films approaching diamond prepared by magnetron sputtering. *Applied Physics Letters* **1996,** *69* (2), 158-160.
48. Hodgkinson, I. J.; Wu, Q. h., *Birefringent Thin Films and Polarizing Elements*.
49. Aspnes, D. E., Optical properties of thin films. *Thin Solid Films* **1982,** *89* (3), 249-262.
50. Irene, E. A., Applications of spectroscopic ellipsometry to microelectronics. *Thin Solid Films* **1993,** *233* (1), 96-111.
51. Chuang, T.-S.; Chang, L.-M., To mitigate airborne molecular contamination through ultra-pure air system. *Building and Environment* **2013,** *59*, 153-163.
52. Chen, J.; Louis, E.; Harmsen, R.; Tsarfati, T.; Wormeester, H.; van Kampen, M.; van Schaik, W.; van de Kruijs, R.; Bijkerk, F., In situ ellipsometry study of atomic hydrogen etching of extreme ultraviolet induced carbon layers. *Applied Surface Science* **2011,** *258* (1), 7-12.
53. Yates, J. T.; Cheng, C. C.; Gao, Q.; Colaianni, M. L.; Choyke, W. J., Atomic H: A reagent for the extraction of chemical species from Si surfaces. *Thin Solid Films* **1993,** *225* (1), 150-154.
54. Vickerman, J. C.; Gilmore, I., *Surface Analysis: The Principal Techniques*. Wiley: 2009.
55. Jablonski, C. J. P. a. A., *NIST Electron Effective-Attentuation-Length Database - Version 1.3*. National Institute of Standards and Technology, Gaithersburg, MD, 2011.
56. High Resolution XPS of Organic Polymers: The Scienta ESCA300 Database (Beamson, G.; Briggs, D.). *Journal of Chemical Education* **1993,** *70* (1), A25.
57. Filik, J.; May, P. W.; Pearce, S. R. J.; Wild, R. K.; Hallam, K. R., XPS and laser Raman analysis of hydrogenated amorphous carbon films. *Diamond and Related Materials* **2003,** *12* (3), 974-978.
58. Cheng, C. C.; Lucas, S. R.; Gutleben, H.; Choyke, W. J.; Yates, J. T., Atomic hydrogen-driven halogen extraction from silicon(100): Eley-Rideal surface kinetics. *Journal of the American Chemical Society* **1992,** *114* (4), 1249-1252.
59. Jackson, B.; Lemoine, D., Eley–Rideal reactions between H atoms on metal and graphite surfaces: The variation of reactivity with substrate. *The Journal of Chemical Physics* **2001,** *114* (1), 474-482.
60. Weinberg, W. H., Eley−Rideal Surface Chemistry: Direct Reactivity of Gas Phase Atomic Hydrogen with Adsorbed Species. *Accounts of Chemical Research* **1996,** *29* (10), 479-487.

61. Knutti, R.; Bühler, R. E., Kinetics of the hydrogen atom reactions with benzene, cyclohexadiene and cyclohexene: hydrogenation mechanism and ring cleavage. *Chemical Physics* **1975,** *7* (2), 229-243.
62. Nakazawa, H.; Osozawa, R.; Enta, Y.; Suemitsu, M., Changes in chemical bonding of diamond-like carbon films by atomic-hydrogen exposure. *Diamond and Related Materials* **2010,** *19* (11), 1387-1392.

Chapter 3

A Study of Electron-Induced Bond Rupture of Halogenated Biphenyls through Dissociative Electron Attachment and Dissociative Ionization.

3. 1. Introduction

Carbon nanomembranes (CNMs) are free-standing films with thicknesses of only a few nanometers[1] . These two-dimensional molecular sheets boast a high mechanical strength and thermal stability along with various other properties which can be tailored depending on the molecular composition and structure of the assembled molecular layers[1-3]. As such, these membranes have great potential for a wide variety of applications[2]. While various methods exist, a promising avenue of CNM fabrication involves the use of electrons to induce cross-linking of specific aromatic self-assembled monolayers (SAMs)[4-7]. While the cross-linking is typically achieved with low energy electrons (50-100 eV), similar cross-linking has been observed with UV, ion, and even high-energy electron (keV range) irradiation[8-13].

It is generally thought that, for typical aromatic monomers of SAMs (such as biphenyls) cross-linking occurs through electron-induced C-H and C-C bond cleavage in the monomers[14]. The resulting reactive radical site, generated through bond cleavage, induces a cross-link with neighboring SAM monomers. Propagation of this effect across the film's surface results in a laterally cross-linked monomolecular film (nanomembrane). While this cross-linking can be initiated directly through the primary (high energy) electron interaction, it is generally thought that backscattered and secondary electrons play a more dominant and direct role in the bond cleavage step[11, 12, 15, 16].

The effects of electrons on matter has been extensively studied. Electron-induced bond rupture and dissociation is ubiquitous in a wide range of fields including: mass spectrometry; lithography; biochemistry; electron beam induced deposition; scanning electron microscopy; and much more. Electrons have been shown to induce bond rupture in self-assembled monolayers, adsorbed molecules (EBID), DNA, and gaseous molecules (mass spectrometry) [11, 17-21].

Electron-induced fragmentation has been shown to proceed through four distinctly different processes: dissociative ionization (DI); neutral dissociation (ND); dipolar dissociation (DD); or through dissociative electron attachment (DEA)[17, 22-25]. DEA is a resonant, bond selective process that begins with the formation of a transient negative ion (TNI). The TNI is formed when a molecule combines with a free electron inducing a vertical transition from the molecules neutral ground state to a corresponding anionic state. DEA can be represented by the following equation.

$$MX + e^- \rightarrow MX^{(\ddagger)-} \rightarrow M^{(\ddagger)} + X^{(\ddagger)-} \quad (3.1)$$

Due to the unstable nature of the TNI, only two channels of relaxation are possible: re-emission of the electron (autodetachment) or dissociation. Dissociation of the TNI results in the formation of a negative ion fragment and a neutral radical counterpart. For low energy electrons, the cross section for TNI formation follows an $E^{-1/2}$ energy dependency and is substantial at or around threshold (0 eV)[26, 27].

Dissociative ionization is a stark contrast to DEA's narrow energy, bond selective process. Whereas DEA requires specific conditions to be met in order to create a TNI, dissociative ionization simply requires that enough energy is imparted to the molecular system to cross the ionization energy threshold required to remove an electron from the molecule. DI can be represented by the following equation where AB represents the progenitor molecule and A and B correspond to the resulting molecular fragments.

$$AB + e^- \rightarrow AB^{(\ddagger)+} + 2e^- \rightarrow A^{(\ddagger)+} + B^{(\ddagger)} + 2e^- \quad (3.2)$$

"(‡)" denotes a molecule / fragment that is in a vibrationally or electronically excited state. The corollary is that DI is a more statistical process whose cross-section spans a wide energy range with an onset slightly above the ionization limit and a maximum in the range of 70-100 eV.

Consequently, the DI phenomenon is prolific occurring in a wide range of fields from electron beam induced deposition to electron impact mass spectroscopy.

While the ion yield for DEA resembles sharp gaussian peaks, indicative of the specific electron energies required for TNI creation, the ion yield curves for DI fragments result in cross sections that are non-existent below a certain threshold energy, known as the appearance energy. After this threshold energy, cross sections quickly increase to their maximum and slowly taper off as the energy transfer in the electron-molecule collision becomes less efficient. The thermochemical threshold (E_{th}) for the formation of positive ion fragments in DI can be written as the following equation where BDE(AB) is the bond dissociation energy of AB and IE(A) is the ionization energy of A.

$$E_{th}(A^+) = BDE(AB) + IE(A) \quad (3.3)$$

Practically speaking, for ion fragments produced through DI, the onset of the ion yield curve corresponds to the energy needed to ionize the corresponding molecular fragment. This makes DI a particularly useful tool in approximating the ionization energy of various molecules and molecular fragments. However, it is worth noting that there are two different types of ionization energy thresholds which can be measured; vertical and adiabatic. The adiabatic ionization energy is defined as the minimum distance between the vibrational ground state of the neutral and the vibrational ground state of the ion[28]. While this is truly the minimum amount of energy necessary to remove an electron from a neutral molecule, it is difficult to directly measure due to the Frank-Condon principle. Since nuclear transitions happen on a much longer time scale than electronic, many techniques, such as electron impact ionization directly measure the vertical ionization energy (appearance energy), which is defined as the energy difference vibrational

ground state of the neutral and the vibrationally excited state of the positive ion at the same equilibrium distance.

For substrates exposed to electrons, the energy distribution of secondary electrons sits below 10 eV and peaks near threshold (0 eV). Additionally, this distribution has a high energy tail whose extension varies depending on the energy of the incident beam and substrate composition[16, 29]. Research on the secondary electron distribution of both silver and copper (common substrates used for self-assembled monolayers) show that, when exposed to a primary electron energy of 30 eV, there is a secondary electron yield that peaks below 1 eV with a full-width half-maximum (FWHM) of about 3.4 and 5.6, respectively[30]. With similar distributions existing for gold (another common SAM substrate), there is a significant intensity of threshold (0 eV) electrons during electron-induced CNM fabrication[31].

Significant secondary electron yields at 0 eV, and bond selectivity, open the possibility to use DEA to purposely enhance cross-linking efficiency and explore the potential of site selectivity in the cross-linking step. This introduces a wide range of possibilities when it comes to controlling the properties and functionality of the resulting nanomembranes. In order to induce a single bond rupture in DEA at 0 eV incident electron energy (highest cross-section), the electron affinity of the charge-retaining molecular fragment (X) must exceed the respective bond dissociation energy (BDE(M-X));

$$\Delta H_{rxn} \approx E_{th} = BDE(M-X) - EA(X) \quad (3.4)$$

In this case, the reaction enthalpy (ΔH_{rxn}) is roughly equal to the respective threshold energy (E_{th}).

In the case of higher halogenated benzenes (Cl, Br, and I), the BDE(C_6H_5-X) decreases significantly from X = Cl (4.14 eV), to Br (3.49 eV), to I (2.82 eV)[32]. The EA of all three halogens,

on the other hand, is comparable (3.61, 3.36, and 3.06 eV for Cl, Br, and I respectively)[33]. This means that the thresholds for the corresponding DEA processes should be 0.53, 0.13, and -0.24 eV for X = Cl, Br, and I respectively.

$$C_6H_5 - X \rightarrow C_6H_5^{\cdot} + X^- \quad (3.5)$$

For comparison, the electron affinity of hydrogen and the phenyl radical is about 0.75 and 1.1 eV respectively[33]. With BDE(C_6H_6-H) being about 4.5 eV[32], the cleavage of hydrogen from benzene is endothermic by more than 3 eV. In practical terms, this means that a higher halogenated phenyl is predisposed to C-X bond cleavage when exposed to very low energy electrons.

It is expected that halogenated biphenyls will follow a similar trend. To this end, this paper performed DEA on three halogenated biphenyl compounds (2-chlorobiphenyl (2-Cl-BPh), 2-bromobiphenyl (2-br-BPh), and 2-iodobiphenyl (2-I-BPh)) with the expectation that the DEA cross sections will behave accordingly: For iodo-biphenyls, the DEA cross sections are expected to be significant at 0 eV due to the exothermic nature of the DEA channel. For bromo-biphenyl we expect the cross section to be noticeably lower yet still existent due to accessibility of this channel at lower energies. Additionally, we expect the chloro-biphenyl DEA cross section to be the lowest due to the inaccessibility of this channel near 0 eV. Finally, we expect C-H cleavage through DEA to be almost non-existent; a conclusion supported by studies performed by Houplin et al. which indicated that DEA was insignificant for terphenyl-thiol (TPT) SAMs[34].

Additionally, experimental studies on electron impact ionization and fragmentation of native biphenyl and halogenated biphenyls are scarce. To aid in this, a systematic evaluation of the positive ionization thresholds for 2-iodobiphenyl, 2-bromobipenyl, and 2-chlorobiphenyl was performed. Ion yield curves were generated, and appearance energies were calculated for the

dominant mass fragments for each compound. Lastly, using approximate thermochemical calculations, several dissociative mechanisms for the dominant fragments were proposed.

3. 2. Experimental

Dissociative electron attachment and dissociative ionization experiments were conducted in an electron-molecule crossed beam apparatus consisting of a trochoidal electron monochromator, an effusive gas inlet system and a quadrupole mass spectrometer (Hiden EPIC1000). The instrument has been described in detail elsewhere[35] and only a brief description is featured here. Electrons emitted from a tungsten filament were collimated by a magnetic field B and guided with electric lenses through the trochoidal electron monochromator in which an E×B section dispersed the electron beam in accordance with the initial electron energy distribution. A quasi mono-energetic segment of the electron energy distribution was selected after the E×B section and crossed an effusive beam of the target molecules in an interaction region confined by the extraction optics of the quadrupole mass spectrometer (QMS). The ionized fragments resulting from the electron-molecule interaction were extracted by a small electric field and subsequently focused into the entrance aperture of the QMS to be analyzed and detected. Mass spectra were recorded by fixing the electron impact energy at 70 eV and scanning through relevant m/z range. Both positive (DI) and negative (DEA) ion yield curves were obtained by fixing the m/z ratio and scanning through the relevant electron energy range. The typical background pressure of the instrument was about 4 x 10^{-8} mbar. The target gas pressure for experimentation ranged from 3 x 10^{-7} to 6 x 10^{-7} mbar making secondary collisions unlikely.

The energy resolution of the electron beam was estimated from the SF_6^- signal of SF_6 at 0 eV incident electron energy and was found to be in the range of about 120-140 meV. To account

for the non-linear energy response of the instrument, a two-point calibration was employed. This energy scale calibration was performed using Equation (3.6) and entering in the measured and reference appearance energies (AEs) of Ar^+ and O_2^+ with argon and ambient air used as target gasses, respectively[36, 37].

$$AE_{Cal} = \frac{(Ar_M - O_{2,m})}{(Ar_{Ref} - O_{2,Ref})}(AE_M - Ar_M) + Ar_{Ref} \quad (3.6)$$

In this equation AE_m represents the measured AE and AE_{Cal} represents the corrected AE value. Ar_m and Ar_{Ref} correspond to both the measured AE and the reference ionization energy of argon, respectively. $O_{2,m}$ and $O_{2,Ref}$ correspond to both the measured AE and the reference ionization energy of oxygen, respectively.

The monochromator was heated to 120°C with two halogen lamps to avoid condensation of the target gas on the electrical lens components. 2-cholorbiphenyl was purchased from abcr, Karlsruhe, Germany with a stated purity of 97%. 2-bromobiphenyl and 2-iodobiphenyl were both purchased from Alfa Aesar, Karlsruhe, Germany, with stated purities of about 98%. All substances were used as delivered without further purification.

Appearance Energies (DI):

To determine the appearance energies (AEs), a function form based on the Wannier threshold law was fitted to the onset regions of the respective positive ion yield curves[38];

$$\begin{aligned} &E \leq AE, && f(x) = b \\ &E > AE, && f(x) = b + a(E - AE)^d \end{aligned} \quad (3.7)$$

E represents the energy of the incident electron, AE the appearance energy, b is a constant that considers the baseline background signal, a is a scaling coefficient and d is an exponential factor. All data sets were recorded in duplicates or triplicates, whereby data acquisition took place

independently on separate days. The fitting procedure was carried out with the commercial software, Mathematica Version 11.0.1.0. These fitting procedures were carried out separately, providing four to six independent determinations for the AEs of all fragments. The confidence limits reported here are the standard deviations from the mean of these values.

To allow comparison between the ionization and fragmentation efficiency between the three halogenated biphenyls, the ion yields are normalized by the pressure, and the Ar^+ ion yield (measured at 70 eV) acquired during each specific experiment:

$$I_{Norm.} = \left(\frac{I_{m/z} / p_{2-X-BPh}}{I_{Ar^+_{70eV}} / p_{Ar}} \right) \quad (3.8)$$

$I_{m/z}$ represents the spectral intensity of the m/z fragment from the halogenated biphenyl, and $p_{2-X-BPh}$ is the partial pressure of the respective halogenated biphenyl during that measurement. $I_{Ar^+_{70eV}}$ and p_{Ar} are the measured Ar^+ ion yield at 70 eV and the partial pressure of argon during the measurement. It is worth noting that the kinetic energy release in the dissociation processes will influence the extraction efficiency of the respective fragments and the transmission efficiency through the QMS may also vary, depending on the m/z ratio of the respective fragments, as discussed in detail in ref. [39].

3. 3. Results and Discussion

Dissociative Electron Attachment (DEA) Analysis:

Figure 3.1. shows the energy dependence of the Cl^-, Br^-, and I^- ion yield from the 2-chlorobiphenyl (2-Cl-BPh), 2-bromobiphenyl (2-Br-BPh), and 2-iodobiphenyl (2-I-BPh), respectively. These represent the DEA cross-sections in the energy range from 0-10 eV. It is worth noting that DEA also revealed the presence of the 153 m/z negative ion fragment between 0-10eV

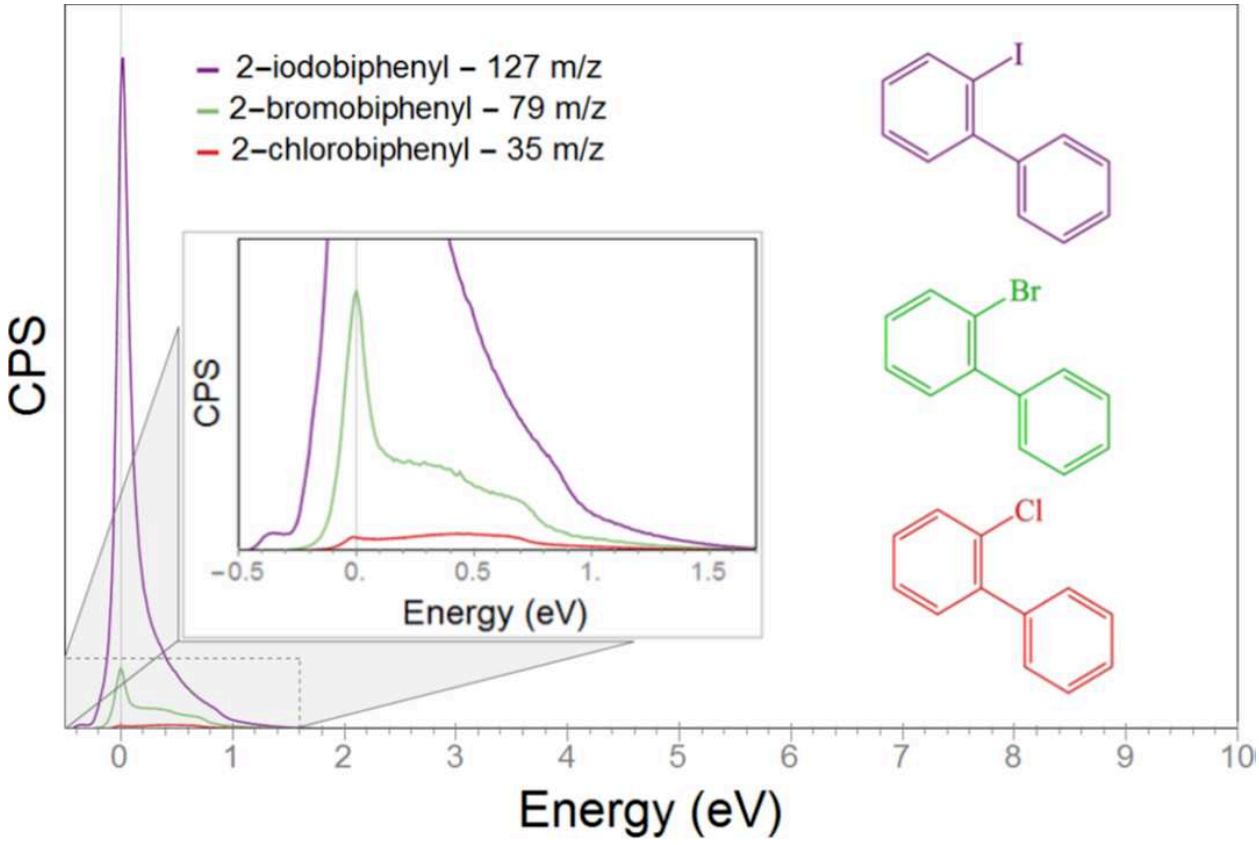

Figure 3. 1: Negative halogen ion yield curves for dissociative electron attachment to 2-chlorobiphenyl (red), 2-bromobiphenyl (green) and 2-iodobiphenyl (violet) in the incident electron energy range from 0 to 10 eV. The region from 0 to about 1.5 eV is expanded to allow better comparison of the 2-chlorobiphenyl and 2-bromobiphenyl ion yield. The respective molecular structures are shown at the top of the figure.

range for all three molecules; however, these cross sections were quite small. Consequently, in DEA, halogen loss is the only significant fragmentation channel. Additionally, the formation of halogen ions is largely confined to a narrow contribution at around 0 eV. Importantly, the relative cross-section for I^- formation is about ten times larger than the relative cross-section for Br^- formation and more than 200 times larger than the cross-section observed for Cl^- formation.

As mentioned in the introduction, the electron attachment cross section at very low electron energies is proportional to $E^{-1/2}$ with a peak centered close to 0 eV[26, 27]. For the attachment process to lead to dissociation at these energies (around 0 eV), the formation of the respective fragment ion must be exothermic. This is the case for the formation of I^- from 2-I-BPh. However, as explained in the introduction, the formation of Cl^- and Br^- anions through DEA is endothermic and should result in negligible cross-sections. The observed formation of Cl^- and Br^- at 0eV (Figure 3.1) can be explained by the internal energy distribution of these molecules at the experimental temperature. If the internal energy of the molecules exceeded the endothermic threshold, the formation of the corresponding ions would become exothermic allowing for DEA at low energies (0 eV). Consequently, the formation of chlorine and bromine anions below their thermomechanical threshold is a direct result of the high energy tail of the respective Maxwell-Boltzmann distribution of internal energy. The higher efficiency of Br- formation as compared to Cl- formation correspondingly reflects the ratio of molecules with an internal energy of >0.13 as compared to >0.53 eV, not the actual attachment cross section. It is worth noting that DEA to 2-bromobiphenyl-4-thiol was studied as a control. It was determined that the effect of the 4-thiol group was found to be insignificant.

For a comparison, the positive ion mass spectra at 70 eV (Figure 3.2) were examined for all three compounds. Initial glances showed that these agreed well with spectra available in the

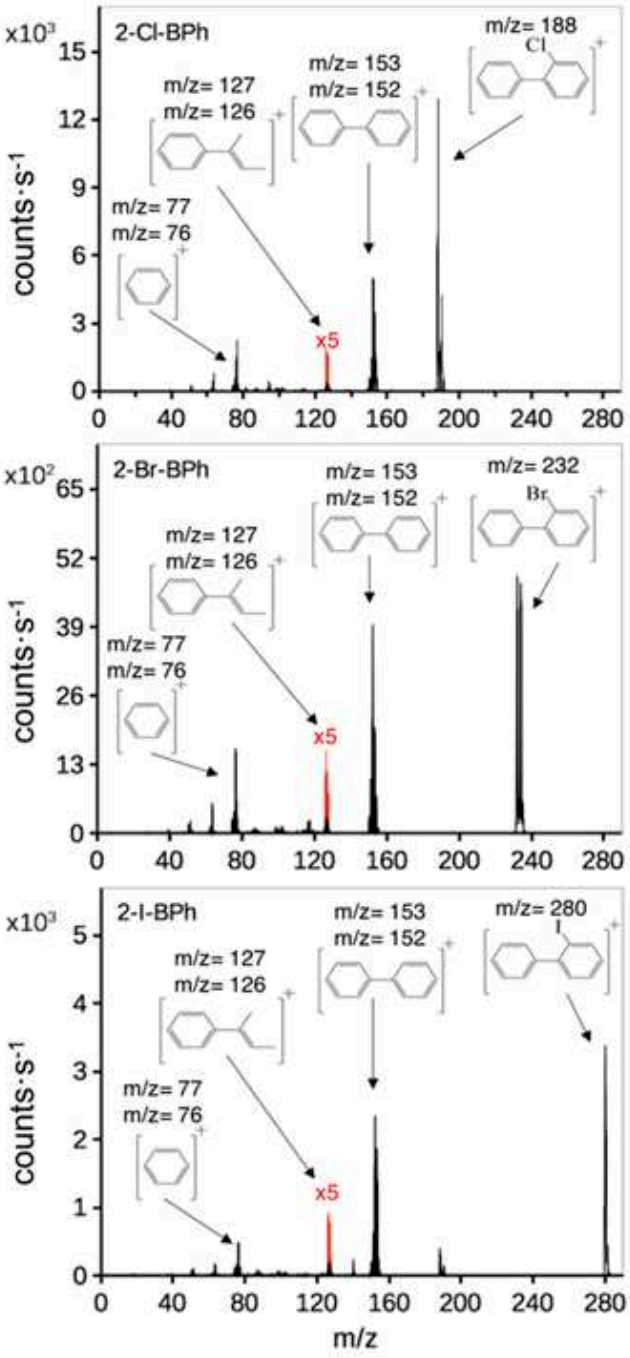

Figure 3. 2: Positive ion mass spectra for 2-chlorobiphenyl (top panel), 2-bromobiphenyl (middle panel) and 2-iodobiphenyl (bottom panel) resulting from electron impact ionization at 70 eV incident electron energy. The double-peak contribution in the mass Spectron of 2-I-BPh at m/z ratios 188/190 is attributed to residual 2-Cl-BPh impurities. Other peaks are assigned as shown in the legend and discussed in the text

NIST database[33]. Efficiency ratios for the DI channels were calculated from the integral intensities of the respective DI fragments divided by the integral intensity of the corresponding parent ions. These ratios were determined to be 1:0.7:0.65 for 2-I-BPh, 2-Br-BPh, and 2-Cl-BPh, respectively. These ratios essentially show that the degree of dissociation following electron impact ionization is similar for all three differently halogenated compounds. Compare this to the efficiency ratio of about 1:0.1:0.0025 observed in DEA of 2-I-BPh, 2-Br-BPh, and 2-Cl-BPh, respectively. While these numbers are not quantitative, they show definitively that there is a significant difference between DEA cross sections of each halogenated species; that is not the case for DI.

The efficacy of this hypothesis, that targeted generation of a radical site by DEA may be used to increase the cross-linking efficiency of CNMs, was tested by Koch et al.[40]. In their studies, self-assembled monolayers (SAM) of biphenyl-thiols (BPTs) and halogenated biphenyl-thiols (2-Cl-BPT, 2-Br-BPT and 2-I-BPT), prepared on Au(111) substrates, were irradiated by electrons at an electron energy of 50 eV. The transition of the SAMs to CNMs was monitored through X-Ray photoelectron spectroscopy (XPS) during the irradiation process. Results from this experiment are shown in Figure 3.3 which plot the XP spectra for nine different stages of electron exposure. It is clear from these results that while electron exposure results in the decrease in intensity of each respective halogen, the rate of reduction for iodine is the fastest followed by bromine and finally chlorine (see Figure 3.3b). This confirms the trend predicted by the DEA experiments performed on 2-I-BPH, 2-Br-BPh, and 2-Cl-BPh. Moreover, comparisons between native and halogenated biphenyl thiols indicate that all three halogenated biphenyls form CNMs at a faster rate than their native counterpart[40].

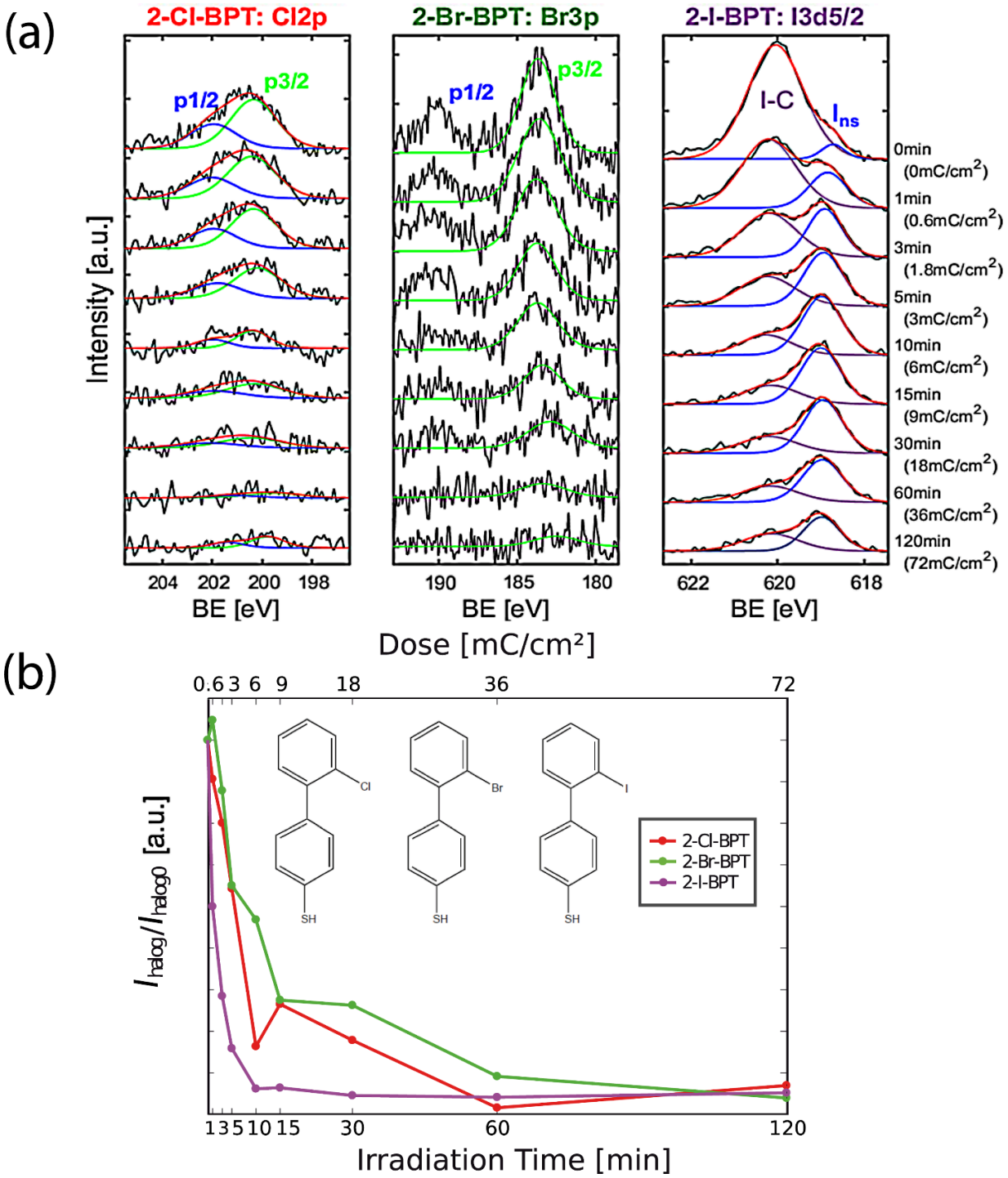

Figure 3. 3: XP spectra of the Cl 2p, Br 3p doublets, and the I $3d_{5/2}$ peak regions of SAMs made of 2-Cl-BPT, 2-Br-BPT, and 2-I-BPT after 0 to 120 min of electron irradiation respectively, where 1 min corresponds to an electron dose of 0.6 mC/cm^2. (a) Raw and fitted spectra of the Cl 2p, Br 3p doublets (blue fit: $p_{1/2}$; green fit: $p_{3/2}$) and the I $3d_{5/2}$ peak of the I 3d doublet peaks of the three halogenated BPT molecules, as a function of electron dose. After electron irradiation, besides the iodine-carbon signal (I-C), a new iodine species becomes more dominant (I_{nS}). (b) Evolution of halogen peak area I_{halog} for Cl (red), Br (green), and I (purple) normalized to the non-irradiated halogen area I_{halog0} due to increasing irradiation dose.

Dissociative Ionization (DI) Analysis:

Figure 3.2 shows the positive ion mass spectra (MS) for 2-chlorobiphenyl (2-Cl-BPh; top panel), 2-bromobiphenyl (2-Br-BPh; middle panel), and 2-iodobiphenyl (2-I-BPh; bottom panel) resulting from electron impact ionization at 70 eV incident electron energy. All three halogenated biphenyls show very similar spectra with the strongest contribution to each spectrum being from the respective progenitor cations. These principal peaks are located at the m/z ratios 188, 232 and 280 for 2-Cl-BPh, 2-Br-BPh, and 2-I-BPh, respectively. The next significant contribution is three main peaks occurring at 153, 152 and 151 m/z for all three species. These correspond to the loss of the halogen, the halogen and one hydrogen and the halogen and two hydrogen atoms, respectively.

All of the remaining peaks at lower m/z values reflect further fragmentation of the biphenyl structure and are largely identical for all three of the halogenated biphenyls. Amongst these lower m/z fragments, the low intensity peaks occurring at m/z = 127 and 126 are attributed to the loss of two carbon atoms along with 2 and 3 hydrogen atoms from the biphenyl moiety, respectively. A more intense set of peaks appears at m/z = 77, 76, and 75 with m/z 76 being the most prominent contribution. From these, the m/z ratios 77 and 75 are attributed to a rupture of the biphenyl bond while the m/z ratio 76 is, to a large extent, from doubly charged fragments associated with the 152 Da fragment. In addition to these principal peaks, there are numerous lower intensity contributions that can be associated with further C_nH_m loss from the biphenyl, e.g., around m/z 100 and 86 or from the phenyl fragment ions, e.g., around m/z 64 and 52, etc.

To determine the appearance energies (AEs) for the formation of individual fragments from the three halogenated biphenyls, we have recorded positive ion yield curves in the onset region for each ion. The experimentally determined AEs for selected fragments are given in Table 3.1. We

Fragment	m/z	Exp. AE	Hessian IE
$C_{12}H_9Cl^+$	188	9.83±0.1	-
$C_{12}H_9^+$	153	13.88±0.2	13.97
$C_{12}H_8^+$	152	14.74±0.1	14.39
$C_{12}H_7^+$	151	14.77±0.2	14.33
$C_{10}H_7^+$	127	16.22±0.4	16.91
$C_{10}H_6^+$	126	14.95±0.3	19.67
$C_6H_5^+$	77	18.66±0.2	-
$C_6H_4^+$	76	22.24±0.9	-
$C_{12}H_9Br^+$	232	9.62±0.2	-
$C_{12}H_9^+$	153	13.07±0.1	13.11
$C_{12}H_8^+$	152	14.10±0.1	14.21
$C_{12}H_7^+$	151	14.16±0.1	14.15
$C_{10}H_7^+$	127	16.36±0.2	16.10
$C_{10}H_6^+$	126	18.91±0.1	19.03
$C_6H_5^+$	77	18.92±0.1	-
$C_6H_4^+$	76	23.42±0.1	-
$C_{12}H_9I^+$	280	8.87±0.3	-
$C_{12}H_9^+$	153	11.79±0.2	11.69
$C_{12}H_8^+$	152	13.43±0.2	13.49
$C_{12}H_7^+$	151	13.42±0.1	13.42
$C_{10}H_7^+$	127	15.42±0.3	14.82
$C_{10}H_6^+$	126	18.51±0.5	18.36
$C_6H_5^+$	77	19.42±0.2	-
$C_6H_4^+$	76	23.39±0.8	-

Table 3. 1: Experimentally derived ionization and appearance energies for the principal fragments observed in electron impact ionization and fragmentation of 2-Cl-BPh, 2-Br-BPh, and 2-I-BPh compared to the respective hessian calculated energies.

note that for the low intensity fragments, the accuracy of the experimentally determined AEs suffers from poor signal-to-noise ratios, which is reflected in the greater error margins reported.

Figure 3.4 shows the electron energy dependence of the positive ion yields for the principal fragmentation channels of 2-Cl-BPh (a and b), 2-Br-BPh (c and d), and 2-I-BPh (e and f). All channels are shown for electron impact energies up to about 50eV. To allow a semi-quantitative comparison, these are normalized with respect to the corresponding Ar^+ ion yields recorded along with the individual data sets, as outlined in the experimental section.

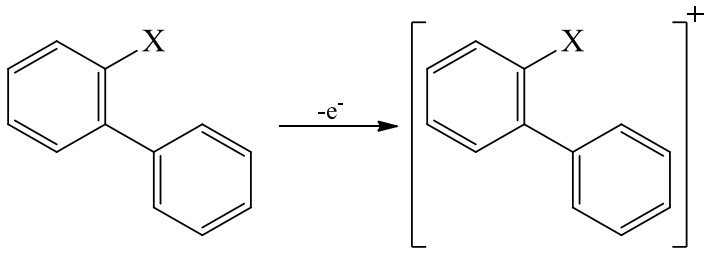

Analysis of Figure 3.2 additionally reveals that each of the halogenated biphenyls exhibit a similar fragmentation pattern; providing strong support for the conclusion that the electron impact fragmentation mechanisms are the same for each of the three halogenated biphenyls. To shed light on the fragmentation pathways we have used a thermochemical approach, utilizing Hess's Law to estimate the appearance energy for a fragment based on a proposed fragmentation of the progenitor ion ($C_{12}H_9X^+$). The viability of a particular fragmentation process was assessed by comparing the agreement between the Hess's law calculation and the experimentally determined appearance energy. In the Hess's Law calculation, approximate bond dissociation energies (BDE) for each of the different bonds (e.g. Ph-H, Ph-Ph) were determined from values found in Luo et al.[32].

To illustrate this process, we start with the cluster of peaks between 150 m/z - 155 m/z, where the biphenyl structure of the parent compound is still intact but the halogen atoms are no longer present. The fragments at 153 m/z, 152 m/z and 151 m/z were chosen due to their relative

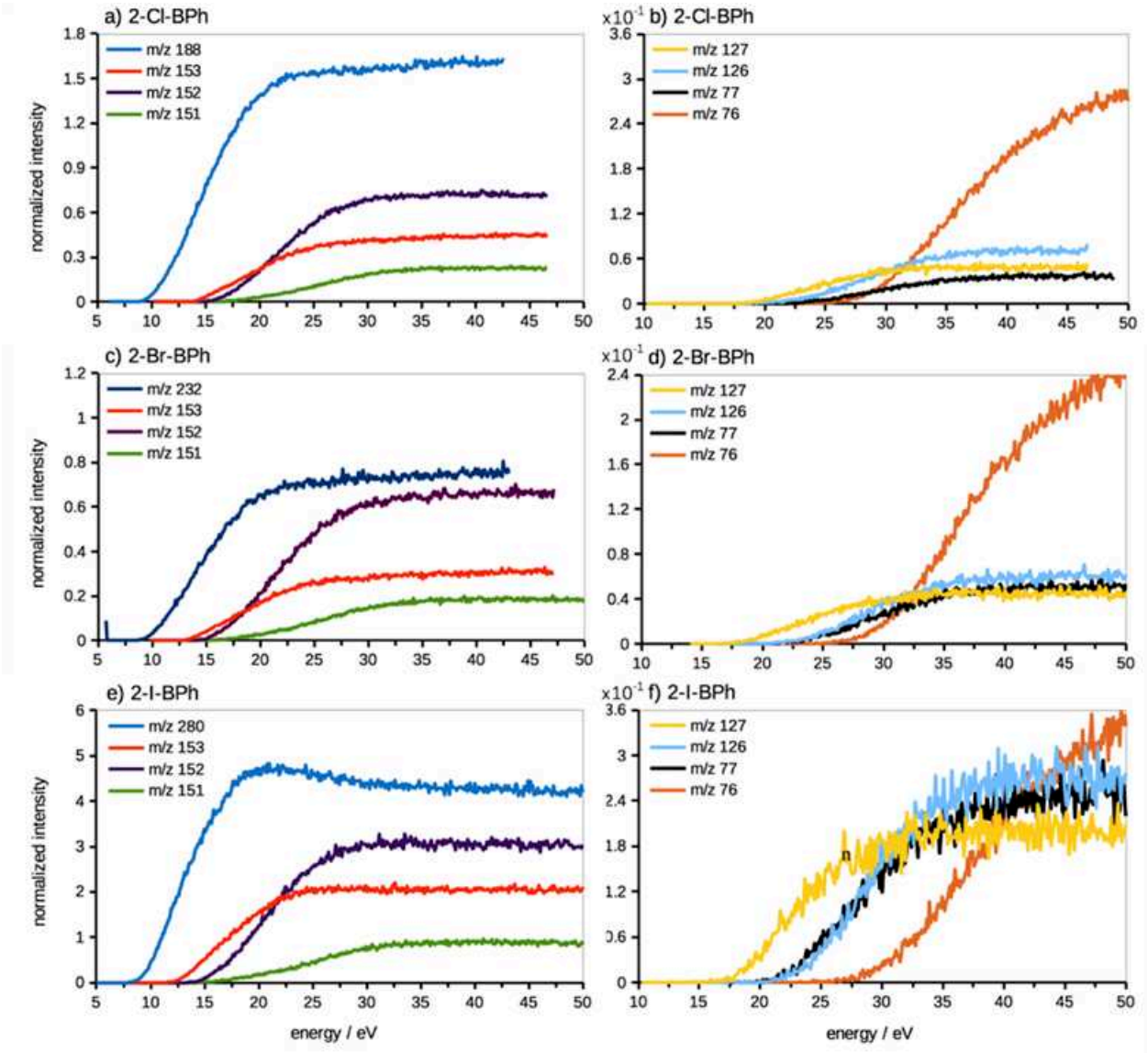

Figure 3. 4: Ion yield curves for the incident electron energy range up to about 50 eV for 2-chlorobiphenyl (a and b), 2-bromobiphenyl (b and c), and 2-iodobiphenyl (d and e). The ion yields are normalized with respect to the target gas pressure and the corresponding Ar^+ ion yield recorded with individual datasets.

intensity, which ensures that each one of these ions can be unambiguously assigned to a $^{12}C_x$ / $^{1}H_y$ fragment. The first fragment, 153 m/z, must involve the loss of a halogen atom from the progenitor ion and the corresponding appearance energy can be estimated from our thermochemical approach by using the equation

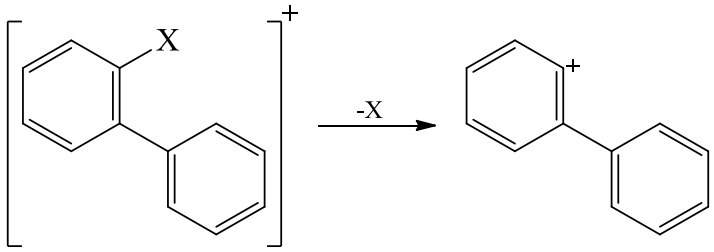

$$\boldsymbol{AE(TCC)}_{153\,m/z} = \boldsymbol{IP}_{C_{12}H_6X} + \boldsymbol{BDE}_{C_6H_5-X}$$

where **AE(TCC)**$_{153m/z}$ represents the appearance energy estimated from the thermochemical calculation (**TCC**) and **BDE**$_{C6H5-X}$ represents the C-X bond dissociation energy in the halogenated biphenyl. Using this approach, the **TCC**$_{153\ m/z}$ values calculated for Cl, Br, and I were 13.97 eV, 13.11 eV, and 11.69 eV respectively. These values are in excellent agreement with the measured AE's of 13.88 eV, 13.07eV, and 11.79 eV for Cl, Br, and I respectively, providing support for the validity of this TCC approach in determining possible fragmentation pathways.

The measured AE's for the 152 m/z fragments are 0.84 eV, 1.03 eV, and 1.64 eV (for I, Br, Cl respectively), higher than the AE's for the 153 m/z fragment. Since the Ph-H BDE is 4.89 eV, is it clear that the 152 m/z fragment cannot be produced by sequential fragmentation of 153 m/z to 152 m/z. Instead, we propose that this ion is formed via the concomitant formation of HX during fragmentation of the progenitor ion.

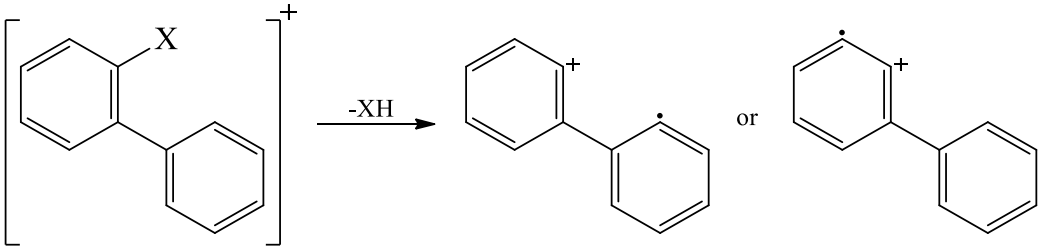

The appearance energy predicted from the thermochemical, Hess's Law, calculation can be determined from the following equation:

$$\boldsymbol{AE(TCC)}_{152\,m/z} = \boldsymbol{IP}_{C_{12}H_6X} + \boldsymbol{BDE}_{C_6H_5-X} + \boldsymbol{BDE}_{C_6H_5-H} - \boldsymbol{BDE}_{H-X}$$

The calculated $\mathbf{AE(TCC)}_{153m/z}$ values for Cl, Br, and I were 14.39 eV, 14.21 eV, and 13.49 eV respectively, closely agreeing with the corresponding measured AE values of 14.74 eV, 14.1 eV, and 13.43 eV.

Examination of the measured AEs for 151 m/z shows that there is little to no change in the appearance energy between the 152 m/z and 151 m/z fragments (e.g. for 2-iodobiphenyl $AE_{152m/z}$ = 13.43 eV and $AE_{151m/z}$ = 13.42 eV). This similarity in AE indicates that in addition to the loss of hydrogen, another bond must be formed. The TCC's indicate that the formation of another Ph-Ph bond is the most likely option.

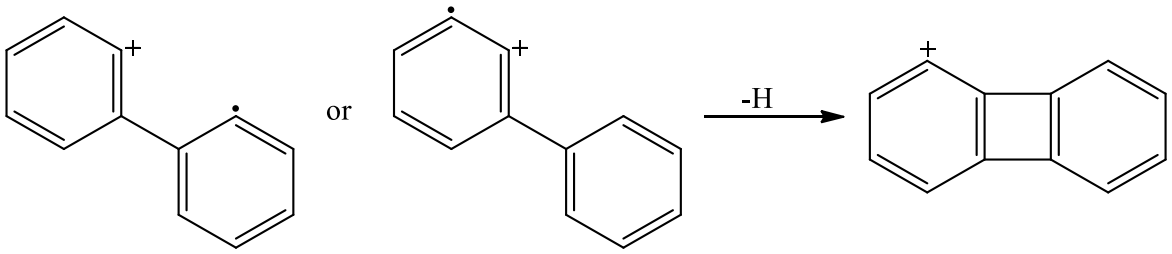

The appearance energy for the 151 m/z fragment formed in this fashion as determined from the TCC ($\mathbf{AE(TCC)}_{151m/z}$) is given by the following equation;

$$\boldsymbol{AE(TCC)}_{151\,m/z} = \boldsymbol{AE}_{152\,m/z} + \boldsymbol{BDE}_{C_6H_5-H} - \boldsymbol{BDE}_{C_6H_5-C_6H_5}$$

The calculated values for this proposed fragmentation pathway are 14.33 eV, 14.15 eV, and 13.42 eV (for Cl, Br, and I respectively), values that are in good agreement with the measured

AE values of 14.77 eV, 14.16 eV, 13.42 eV. In principle the 151m/z fragment could also originate from the loss of H_2 from the 153m/z fragment. However, the thermochemical calculation for such a process overestimates the measured AE by about 4 eV. Thus, the 151 m/z fragment is most likely stems from the fragmentation of the 152 m/z ion.

The next cluster of peaks are at 127 m/z and 126 m/z where a C2 moiety along with the halogen atoms have been lost from the parent compound. We assert that these two peaks are formed by the loss of acetylene from the 153 m/z and 152 m/z fragments. This assertion is based on the characteristic loss of acetylene from aromatic cations. For example, in the electron impact ionization MS of toluene the frequently observed peak at m/e = 65 is due to the loss of neutral acetylene from the tropylium ion. The same acetylene loss is also observed in the mass fragmentation of naphthalene.

For the 127m/z peak, the most likely structure of the cation is shown below, where loss of acetylene is accompanied by the formation of a polycylic aromatic hydrocarbon.

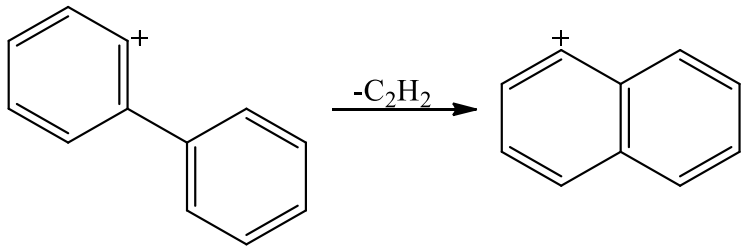

The thermochemical approximation for the 127 m/z fragment formed in this fashion is given by the following equation;

$$\boldsymbol{AE(TCC)}_{127\,m/z} = \boldsymbol{AE}_{153\,m/z} + \boldsymbol{BDE}_{C_6H_6} - \boldsymbol{BDE}_{C\equiv C} + \boldsymbol{BDE}_{C_6H_5-\boldsymbol{C_6H_5}} + \Delta_{RE}$$

where $\mathbf{AE(TCC)}_{127m/z}$ corresponds to the measured appearance energy of the 127 m/z fragment and $\boldsymbol{\Delta}_{RE}$ corresponds to the difference in resonance energy between two phenyl groups and naphthalene ($\boldsymbol{\Delta}_{RE}$ = 0.46 eV). The calculated values for this proposed fragmentation pathway

are 16.87 eV, 16.23 eV, and 15.56 eV (for Cl, Br, and I respectively). These values are in reasonably good agreement with the measured AE's of 16.22 eV, 16.36 eV, and 15.42 eV.

Much like the 153 m/z and 152 m/z fragments, the difference in measured AE for 126 m/z and 127 m/z is not enough to explain a simple sequential degradation of 127 m/z via hydrogen loss. Consequently, the mechanism to produce 126 m/z is more likely the result of sequential degradation of the 152 m/z fragment. A similar type of acetylene loss has been shown to occur in the dissociative ionization of naphthalene among other polycyclic compounds.

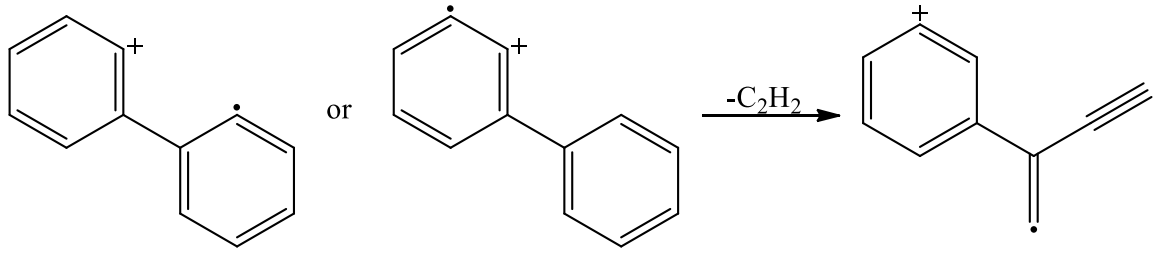

The thermochemical approximation for the 126 m/z fragment formed in this fashion is given by the following equation;

$$\boldsymbol{AE(TCC)}_{126\,m/z} = \boldsymbol{AE}_{152\,m/z} + 6\left(\boldsymbol{BDE}_{C_6H_6}\right) - 2(\boldsymbol{BDE}_{C\equiv C}) - \boldsymbol{BDE}_{C=C} - \boldsymbol{BDE}_{C-C}$$

where, **AE(TCC)**$_{126\ m/z}$ represents the thermochemical approximation for the 126 m/z fragment. The inclusion of six **BDE**$_{C6H6}$ is used to approximate the opening of the benzene ring and loss of the aromatic nature of the corresponding carbons. The calculated values for this proposed fragmentation pathway are 19.03 eV and 18.36 eV (for Br and I respectively) and agree with the measured AE's of 18.91 eV and 18.51 eV. It is important to note that the measured AE for the 126 m/z fragment (14.95 eV) of 2-chlorobiphenyl was significantly ~4 eV lower than what was observed for either 2-iodobiphenyl and 2-bromobiphenyl. The significant difference for the AE for 2-chlorobiphenyl is unclear, but we note that the onset of this fragment has a particularly

shallow gradient and thus a large degree of experimental error is associated with the calculated AE.

The last prominent peak encountered for each of the halogenated biphenyls is the fragment at 77 m/z. This fragment likely corresponds to ionized phenyl ($C_6H_5^+$). The large energy difference between the measured AE's of the progenitor peaks and 77 m/z fragments indicate that 77 m/z cannot come from the degradation of the ionized progenitor. The energy difference between the AE of 77 m/z and the 152 m/z fragments roughly corresponds to the Ph-Ph bond energy (see **AE(TCC)**$_{77m/z}$ below), suggesting that the 77 m/z ion could be formed as a result of the fragmentation of the 152 m/z ion.

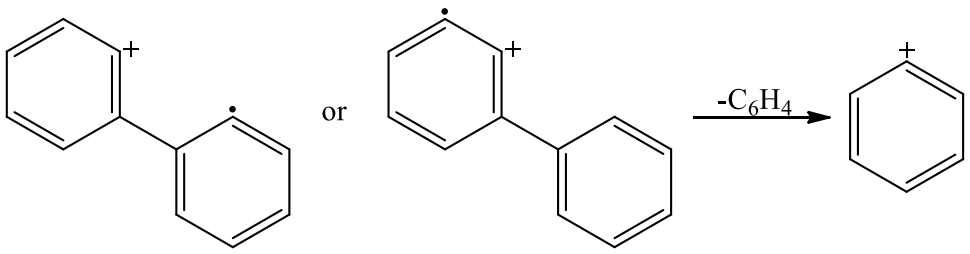

The thermochemical approximation for the appearance energy of the 77 m/z fragment formed in this fashion is given by the following equation;

$$\boldsymbol{AE(TCC)}_{77\ m/z} = \boldsymbol{AE}_{152\ m/z} + \boldsymbol{BDE}_{C_6H_5-\boldsymbol{C_6H_5}}$$

The calculated values for this proposed fragmentation pathway are 19.34 eV, 19.16 eV, and 18.44 eV (for Cl, Br, and I respectively), in relatively good agreement with measured AE's of 18.66 eV, 18.92 eV, and 19.42 eV. In principle the $C_6H_5^+$ ion could also have been formed by fragmentation of the Ph-Ph bond in the 153m/z ion. This TCC approach yields AEs of 18.93 eV, 18.06 eV, and 16.64 eV which are in poorer agreement with the experimentally determined values, but within the bounds of possibility. As a result, the 77 m/z fragment could be formed as a sequential degradation product of 153 m/z and/or 152 m/z ions.

3. 4. Conclusions

High DEA cross sections were observed at 0 eV for 2-I-BPh as compared to 2-Br-BPh and 2-Cl-BPh. Comparison of the ratio of these cross sections with similar DI pathways revealed that that 2-I-BPh was particularly susceptible to halogen cleavage through DEA as compared to DI. This radical formation through effective DEA channels may be purposely used to enhance the cross-linking efficiency for the production of CNMs. To test this hypothesis, Koch et al. tested the cross-linking efficiency for biphenyl thiol (BPT), 2-iodobiphenyl thiol (2-I-BPT), 2-bromobiphenyl (2-Br-BPT), and 2-chlorobiphenyl (2-Cl-BPT)[40]. The effect of electron irradiation on the bonding in the halogenated biphenyl thiols was monitored using XPS. These studies revealed that the concentration of each corresponding halogen species decreased at a steeper rate for 2-I-BPT as compared to 2-Br-BPT and 2-Cl-BPT. Furthermore, it was also shown that the extent and rate at which new electron-induced sulphur species formed were almost 10 time faster for 2-I-BPT as compared to conventional BPT and other halogenated biphenyl species[40]. Additionally, CNMs of each species were made and transferred to TEM grids for optical inspection. It was revealed that for 2-I-BPT, an electron dose of only 1.8 mC/cm^2 was able to generate a CNM of sufficient mechanical stability to survive the transfer process to a TEM grid. This is compared to the significantly higher dose of 40-60 mC/cm^2 needed to produce a native BPT CNM of comparable strength[40]. The superior performance of 2-I-BPT compared to 2-Br-BPT, 2-Cl-BPT, and native BPT strongly indicated that this enhanced cross-linking efficiency is rooted in the significantly higher DEA cross section of 2-I BPT, supporting the hypothesis presented here.

In addition, the AE's for the principal fragments observed upon DI of 2-I-BPh, 2-Br-Bph, and 2-Cl-BPh were reported. Further analysis comparing hessian calculated energies with the

experimentally determined AE's revealed several possible fragmentation pathways common for all three halogenated biphenyl compounds (see Figure 3.5).

3. 5. Acknowledgements

MB would like to thank Oddur Ingólfsson and the University of Iceland for their hospitality, expertise, and use of their equipment.

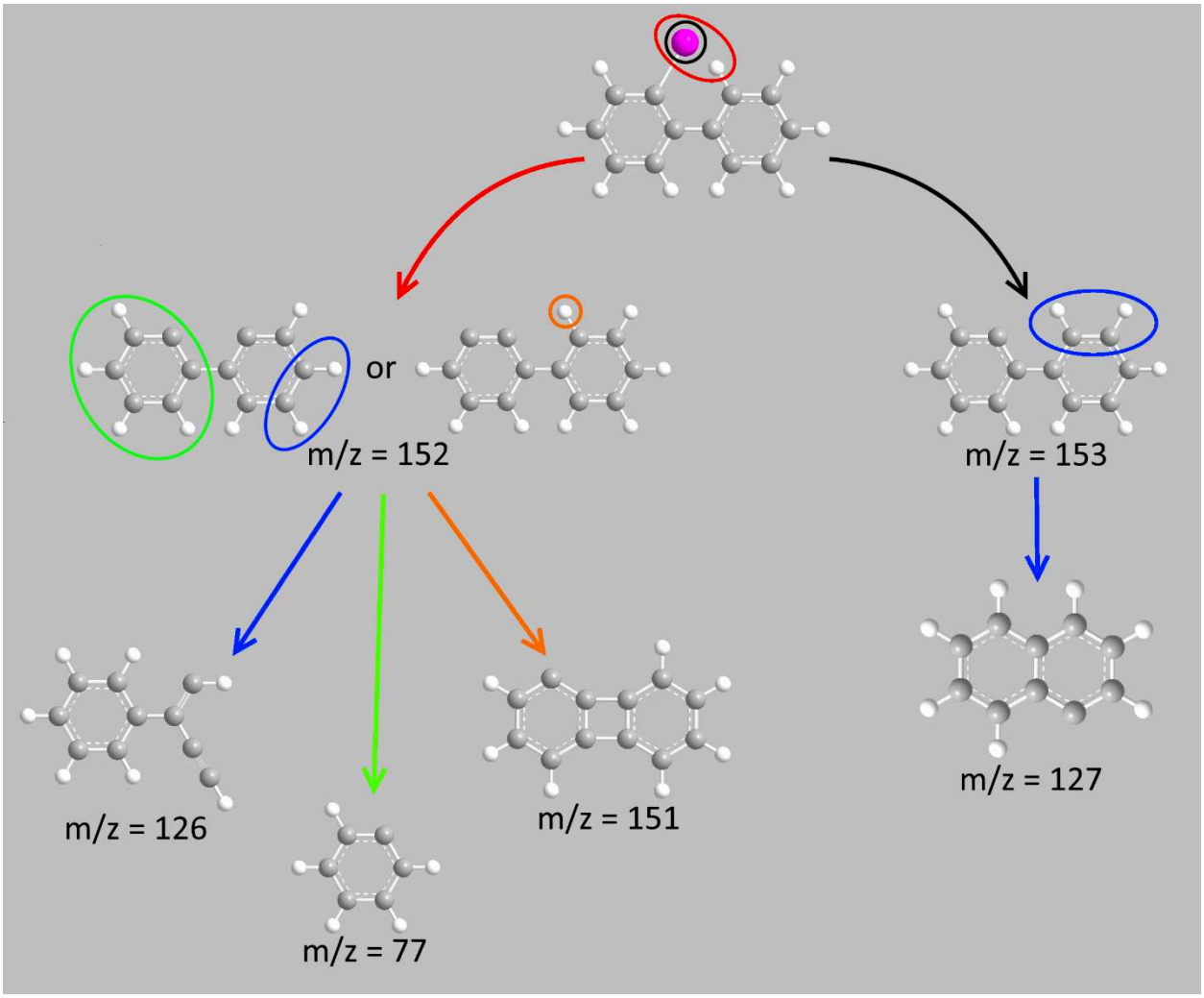

Figure 3. 5: Overview of the predicted fragmentation pathways upon electron impact ionization of the halogenated biphenyls 2-X-Bph, X= Cl, Br, or I. The initial fragmentation is expected to advance through halogen (black) or halogen-hydrogen loss (red). Further fragmentation is sequential to these and results primarily in the m/z 151 ions (additional hydrogen loss from the m/z 152 fragment) and the m/z 127 and 126 ions through acetylene loss from the m/z 153 and 152 ions, respectively. Lastly, the m/z ratio 77 fragment is assigned to the cleavage of the C-C bond joining both rings and coming predominantly from the m/z/ 152 fragment.

3. 6. References

1. Angelova, P.; Vieker, H.; Weber, N.-E.; Matei, D.; Reimer, O.; Meier, I.; Kurasch, S.; Biskupek, J.; Lorbach, D.; Wunderlich, K.; Chen, L.; Terfort, A.; Klapper, M.; Müllen, K.; Kaiser, U.; Gölzhäuser, A.; Turchanin, A., A Universal Scheme to Convert Aromatic Molecular Monolayers into Functional Carbon Nanomembranes. *ACS Nano* **2013,** *7* (8), 6489-6497.
2. Turchanin, A.; Gölzhäuser, A., Carbon Nanomembranes. *Advanced Materials* **2016,** *28* (29), 6075-6103.
3. Eck, W.; Küller, A.; Grunze, M.; Völkel, B.; Gölzhäuser, A., Freestanding Nanosheets from Crosslinked Biphenyl Self-Assembled Monolayers. *Advanced Materials* **2005,** *17* (21), 2583-2587.
4. Beyer, A.; Godt, A.; Amin, I.; Nottbohm, C. T.; Schmidt, C.; Zhao, J.; Gölzhäuser, A., Fully cross-linked and chemically patterned self-assembled monolayers. *Physical Chemistry Chemical Physics* **2008,** *10* (48), 7233-7238.
5. Turchanin, A.; Tinazli, A.; El-Desawy, M.; Großmann, H.; Schnietz, M.; Solak, H. H.; Tampé, R.; Gölzhäuser, A., Molecular Self-Assembly, Chemical Lithography, and Biochemical Tweezers: A Path for the Fabrication of Functional Nanometer-Scale Protein Arrays. *Advanced Materials* **2008,** *20* (3), 471-477.
6. Kankate, L.; Aguf, A.; Großmann, H.; Schnietz, M.; Tampé, R.; Turchanin, A.; Gölzhäuser, A., Vapor Phase Exchange of Self-Assembled Monolayers for Engineering of Biofunctional Surfaces. *Langmuir* **2017,** *33* (15), 3847-3854.
7. Schnietz, M.; Turchanin, A.; Nottbohm, C. T.; Beyer, A.; Solak, H. H.; Hinze, P.; Weimann, T.; Gölzhäuser, A., Chemically Functionalized Carbon Nanosieves with 1-nm Thickness. *Small* **2009,** *5* (23), 2651-2655.
8. Eck, W.; Gölzhäuser, A.; Grunze, M.; Küller, A.; Shaporenko, A.; Tai, Y.; Zharnikov, M., *Electron-beam induced cross-linking of aromatic-assembled monolayers: A basis for nanolithography and free-standing nanosheets*. 2005.
9. Geyer, W.; Stadler, V.; Eck, W.; Gölzhäuser, A.; Grunze, M.; Sauer, M.; Weimann, T.; Hinze, P., Electron induced chemical nanolithography with self-assembled monolayers. *Journal of Vacuum Science & Technology B: Microelectronics and Nanometer Structures Processing, Measurement, and Phenomena* **2001,** *19* (6), 2732-2735.
10. Geyer, W.; Stadler, V.; Eck, W.; Zharnikov, M.; Gölzhäuser, A.; Grunze, M., Electron-induced crosslinking of aromatic self-assembled monolayers: Negative resists for nanolithography. *Applied Physics Letters* **1999,** *75* (16), 2401-2403.
11. Turchanin, A.; Schnietz, M.; El-Desawy, M.; Solak, H. H.; David, C.; Gölzhäuser, A., Fabrication of Molecular Nanotemplates in Self-Assembled Monolayers by Extreme-Ultraviolet-Induced Chemical Lithography. *Small* **2007,** *3* (12), 2114-2119.
12. Zhang, X.; Vieker, H.; Beyer, A.; Gölzhäuser, A., Fabrication of carbon nanomembranes by helium ion beam lithography. *Beilstein Journal of Nanotechnology* **2014,** *5*, 188-194.
13. Beyer, A.; Turchanin, A.; Nottbohm, C. T.; Mellech, N.; Schnietz, M.; Gölzhäuser, A., Fabrication of metal patterns on freestanding graphenoid nanomembranes. *Journal of Vacuum Science & Technology B* **2010,** *28* (6), C6D5-C6D10.
14. Amiaud, L.; Houplin, J.; Bourdier, M.; Humblot, V.; Azria, R.; Pradier, C. M.; Lafosse, A., Low-energy electron induced resonant loss of aromaticity: consequences on cross-linking in terphenylthiol SAMs. *Physical Chemistry Chemical Physics* **2014,** *16* (3), 1050-1059.
15. Turchanin, A.; Beyer, A.; Nottbohm, C. T.; Zhang, X.; Stosch, R.; Sologubenko, A.; Mayer, J.; Hinze, P.; Weimann, T.; Gölzhäuser, A., One Nanometer Thin Carbon Nanosheets with Tunable Conductivity and Stiffness. *Advanced Materials* **2009,** *21* (12), 1233-1237.
16. Schaefer, J.; Hoelzl, J., A contribution to the dependence of secondary electron emission from the work function and fermi energy. *Thin Solid Films* **1972,** *13* (1), 81-86.

17. Bald, I.; Langer, J.; Tegeder, P.; Ingólfsson, O., From isolated molecules through clusters and condensates to the building blocks of life. *International Journal of Mass Spectrometry* **2008,** *277* (1), 4-25.
18. Li, Z.; Zheng, Y.; Cloutier, P.; Sanche, L.; Wagner, J. R., Low Energy Electron Induced DNA Damage: Effects of Terminal Phosphate and Base Moieties on the Distribution of Damage. *Journal of the American Chemical Society* **2008,** *130* (17), 5612-5613.
19. Turchanin, A.; Käfer, D.; El-Desawy, M.; Wöll, C.; Witte, G.; Gölzhäuser, A., Molecular Mechanisms of Electron-Induced Cross-Linking in Aromatic SAMs. *Langmuir* **2009,** *25* (13), 7342-7352.
20. Wnuk, J. D.; Gorham, J. M.; Rosenberg, S. G.; van Dorp, W. F.; Madey, T. E.; Hagen, C. W.; Fairbrother, D. H., Electron Induced Surface Reactions of the Organometallic Precursor Trimethyl(methylcyclopentadienyl)platinum(IV). *The Journal of Physical Chemistry C* **2009,** *113* (6), 2487-2496.
21. Hans , W. P. K.; Johannes, K.; Michael, R.; Markus, W.; Gerold, D.; Kam , L. L., Characterization and Application of Materials Grown by Electron-Beam-Induced Deposition. *Japanese Journal of Applied Physics* **1994,** *33* (12S), 7099.
22. Christophorou, L. G., *Electron–Molecule Interactions and Their Applications*. Academic Press: Cambridge, MA, U.S.A., 2013; Vol. 2.
23. Fabrikant, I. I.; Eden, S.; Mason, N. J.; Fedor, J., Chapter Nine - Recent Progress in Dissociative Electron Attachment: From Diatomics to Biomolecules. In *Advances In Atomic, Molecular, and Optical Physics*, Arimondo, E.; Lin, C. C.; Yelin, S. F., Eds. Academic Press: 2017; Vol. 66, pp 545-657.
24. Arumainayagam, C. R.; Lee, H.-L.; Nelson, R. B.; Haines, D. R.; Gunawardane, R. P., Low-energy electron-induced reactions in condensed matter. *Surface Science Reports* **2010,** *65* (1), 1-44.
25. Böhler, E.; Warneke, J.; Swiderek, P., Control of chemical reactions and synthesis by low-energy electrons. *Chemical Society Reviews* **2013,** *42* (24), 9219-9231.
26. Wigner, E. P., On the Behavior of Cross Sections Near Thresholds. *Physical Review* **1948,** *73* (9), 1002-1009.
27. Schramm, A.; Weber, J. M.; Kreil, J.; Klar, D.; Ruf, M. W.; Hotop, H., Laser Photoelectron Attachment to Molecules in a Skimmed Supersonic Beam: Diagnostics of Weak Electric Fields and Attachment Cross Sections Down to $20\mathit{\ensuremath{\mu}}\mathrm{eV}$. *Physical Review Letters* **1998,** *81* (4), 778-781.
28. Field, F. H.; Franklin, J. L., *Electron impact phenomena and the properties of gaseous ions*. New York (N.Y.) : Academic press: 1957.
29. Kaoru Ohya; Akio Harada; Jun Kawata; Kenji Nishimura, Monte Carlo Simulation of Yield and Energy Distribution of Secondary Electrons Emitted from Metal Surfaces. *Japanese Journal of Applied Physics* **1996,** *35* (12R), 6226.
30. Seah, M. P., Slow electron scattering from metals: I. The emission of true secondary electrons. *Surface Science* **1969,** *17* (1), 132-160.
31. Nishimura, K.; Kawata, J.; Ohya, K., Comparative study of secondary electron emission from solids under positron and electron impacts. *Nuclear Instruments and Methods in Physics Research Section B: Beam Interactions with Materials and Atoms* **2000,** *164-165*, 903-909.
32. Luo, Y. R., *Comprehensive handbook of chemical bond energies*. CRC Press: Boca Raton, FL, U.S.A., 2007.
33. Stein, S. E., NIST Chemistry WebBook, NIST Standard Reference Database Number 69. Linstrom, P. J.; Mallard, W. G., Eds. National Institute of Standards and Technology: Gaithersburg MD, U.S.A., 2017.
34. Houplin, J.; Dablemont, C.; Sala, L.; Lafosse, A.; Amiaud, L., Electron Processing at 50 eV of Terphenylthiol Self-Assembled Monolayers: Contributions of Primary and Secondary Electrons. *Langmuir* **2015,** *31* (50), 13528-13534.

35. Bjarnason, E. H.; Ómarsson, B.; Engmann, S.; Ómarsson, F. H.; Ingólfsson, O., Dissociative electron attachment to titatinum tetrachloride and titanium tetraisopropoxide. *The European Physical Journal D* **2014,** *68* (5), 121.
36. Wetzel, R. C.; Baiocchi, F. A.; Hayes, T. R.; Freund, R. S., Absolute cross sections for electron-impact ionization of the rare-gas atoms by the fast-neutral-beam method. *Physical Review A* **1987,** *35* (2), 559-577.
37. Linstrom, P. J.; Mallard, W. G.; National Institute of, S.; Technology NIST chemistry webbook. http://webbook.nist.gov/chemistry/.
38. Wannier, G. H., The Threshold Law for Single Ionization of Atoms or Ions by Electrons. *Physical Review* **1953,** *90* (5), 817-825.
39. Engmann, S.; Stano, M.; Papp, P.; Brunger, M. J.; Matejčík, Š.; Ingólfsson, O., Absolute cross sections for dissociative electron attachment and dissociative ionization of cobalt tricarbonyl nitrosyl in the energy range from 0 eV to 140 eV. *The Journal of Chemical Physics* **2013,** *138* (4), 044305.
40. Koch, S.; Kaiser, C. D.; Penner, P.; Barclay, M.; Frommeyer, L.; Emmrich, D.; Stohmann, P.; Abu-Husein, T.; Terfort, A.; Fairbrother, D. H.; Ingólfsson, O.; Gölzhäuser, A., Amplified cross-linking efficiency of self-assembled monolayers through targeted dissociative electron attachment for the production of carbon nanomembranes. *Beilstein Journal of Nanotechnology* **2017,** *8*, 2562-2571.

Chapter 4

Electron-Induced Reactions of Surface Adsorbed Iron Carbonyl Precursors

4. 1. Introduction

Electron beam induced deposition (EBID) is a fabrication technique capable of creating complex three-dimensional nano-structures. This vacuum-based technique utilizes focused electron beams to decompose transiently adsorbed precursor molecules into nanosized structures[1]. The innate, direct-write, methodology removes the need for solvents, resists, or masks and allows for an almost limitless array of free-standing, nanometer scale 3D structures. Due to the high interaction cross-section of electrons, a vast library of precursor molecules can be utilized, allowing for numerous potential applications[1]. Currently, EBID is being used in the repair of extreme ultraviolet light lithography masks, the production of custom tips for scanning tunneling / atomic force microscopes, and as a method for fabricating hall sensors[1-4].

Thus far, most studies, centered around EBID, involve using volatile organometallic precursors to deposit metal containing structures. The desired chemical and/or physical properties of these metal containing structures dictate the identity of the organometallic precursor used. In addition, ideal precursors are sufficiently volatile, nontoxic, and commercially available. Iron containing organometallic precursors are of particular interest in the EBID community due to their ability to make nanometer-sized ferromagnetic deposits[5-8]. These nanometer scale deposits have a wide variety of potential applications that range from their ability to make ultrahigh density magnetic recording devices as well as nanometer sized magnetic devices such as those used in spintronics and magneto-optical Kerr devices.

There is a diverse selection of sufficiently volatile, commercially available, and cheap iron containing precursors. Iron pentacarbonyl, $Fe(CO)_5$, is one of the more popular iron containing precursors and a wide variety of supporting research. $Fe(CO)_5$'s high vapor pressure and commercial abundance are the likely sources for its common use in the EBID community. Papers

involving this precursor have used it as a precursor gas for magnetic iron nanopillars, making iron nanocrystals, and as method of producing iron capping layers for already deposited nanostructures[7, 9]. As reported in Hochleitner et al., Schirmer et al. and Masaki et al. the average atomic percent of iron in these deposits ranges from about 48% - 80%[6, 8, 10]. Research performed by Lukasczyk et al. has even induced $Fe(CO)_5$ to produce deposits as pure as 95% iron[7].

Diiron nonacarbonyl, $Fe_2(CO)_9$, has an almost nonexistent vapor pressure at room temperature. Consequently, EBID research involving this compound is less common. Nonetheless, $Fe_2(CO)_9$ has been successfully used to dope carbon nanotubes with iron and to construct iron nanowires used for magneto-resistance and spintronic devices[5, 11]. As reported in these sources, the average atomic percentages of iron in these deposits ranges from about 50% - 80% with Pfeiffer et al. showing a purity as high as 95%[5, 11, 12].

In addition to its even lower vapor pressure, triiron dodecacarbonyl, $Fe_3(CO)_{12}$, is relatively unstable with respect to the other iron carbonyl compounds. As a method of stabilization, commercial sources of this precursor add 5-10% methanol. To avoid co-deposition of the methanol additive during EBID, $Fe_3(CO)_{12}$ must be further purified upon delivery. For these reasons, there is very little EBID research involving this compound. Presently, only two known and published EBID references can be found[9, 13]. In both cases $Fe_3(CO)_{12}$ was utilized to simple, iron containing nanostructures. However, of these two, only the thesis written by M. Beljaars involved characterization of structure purity[13]. The average atomic percentage of iron in the corresponding iron nanostructures was shown to be about 50%[13].

The precursor, $HFeCo_3(CO)_{12}$, is a compound that provides an interesting case study[14, 15]. The bimetallic nature of this precursor allows for the production of mixed metal nanostructures with well-defined metal ratios. While the bimetallic nature and the resulting properties of these

nanostructures is quite interesting, the most notable property of these deposits is their unusually high metal content when compared to typical EBID deposits. Compositional studies performed by Porrati et al. have shown this precursor to produce structures with metal contents averaging about 80 at. %[15].

As mentioned, the EBID process leaves behind relatively high levels of organic contamination. It is generally accepted that the deposition process is driven by low energy, secondary electrons produced when the high energy, principal electron beam interacts with the substrate. The low energy electrons interact with transiently adsorbed molecules on the surface of the substrate causing these molecules to decompose into both non-volatile and volatile components[14, 16-18]. The resulting volatile fragments are pumped off while the non-volatile fragments are incorporated into the deposit. While residual water and/or hydrocarbons present in the deposition chamber can contribute to the observed contamination, previous studies have shown that neither are principal contributors. The organic impurities primarily result from incomplete scission of volatile ligand fragments from the metal center during the initial fragmentation steps[16-19]. These remaining ligands get incorporated into the deposit and are subjected to further electron interactions resulting in their decomposition into a carbonaceous matrix. The resulting impurities are often significant enough to impact important physical properties such as resistivity, conductivity, and magnetic susceptibility. The inability to control the extent and the type of impurities found in these final deposits limits the applications of EBID. In addition, since EBID centers around dissociation of the precursor molecule to create nanostructures, a better understanding of the fragmentation dynamics of these molecules is crucial toward making EBID a more viable technique.

An approach, pioneered by Wnuk et al., has been successfully utilized to study precursor decomposition in the EBID process[18]. This technique employs an ultrahigh vacuum (UHV) surface science approach which allows for the study of chemical mechanisms that cannot be observed in the electron microscopes typically used to make EBID nanostructures. The first step in this two-step process involves the creation of a thin film, formed by adsorbing a finite amount of precursor onto a chilled, chemically inert substrate. The second step involves exposing this film to a controlled amount of low energy (typically 500 eV) electron irradiation. Using X-ray photoelectron spectroscopy (XPS), and other surface analytical tools, changes in the bonding environment of elements contained in the precursor complex can be tracked. This in-situ interrogation plots the effects of electron irradiation of adsorbed precursors as a function of electron dose allowing for the elucidation of the mechanistic steps responsible for precursor decomposition and metal deposition.

Using this methodology previous studies on $W(CO)_6$, $Co(CO)_3NO$, and $[(\eta^3 - C_3H_5)Ru(CO)_3Br]$ have shed light on the decomposition mechanism for metal carbonyl precursors[17, 20, 21]. These studies have shown that deposition occurs through a two-step mechanism. In the first step, the adsorbed molecule interacts with a single electron resulting in the scission of one or more volatile carbonyl ligands from the precursor. In the second step, the remaining metal plus ligand fragments are exposed to additional electrons resulting in non-volatile decomposition of the remaining ligands. The most notable result from these studies is the fact that some, but not all ligands are removed from these compounds. An exception to this trend has been observed by some researchers for several multi-metallic compounds, most notably $HFeCo_3(CO)_{12}$ and $Co_2(CO)_8$[15, 22]. In both cases EBID structures consisting of a metal content >90% were produced. In the case of $Co_2(CO)_8$, this effect was ascribed to the catalytic properties of Co[22]. Despite this, a

general trend remains, indicating that metal-metal bonds tend to yield deposits with higher metal content than those without.

Since no studies have been conducted involving similar mono and multi-metallic compounds, three compounds were selected. $Fe(CO)_5$, $Fe_2(CO)_9$, and $Fe_3(CO)_{12}$ were chosen due to their systematic differences and relative similarities. By applying the aforementioned surface science approach, a comparison between the kinetic differences of all three compounds can be obtained aiding in studying effect metal-metal bonding of the same metal has on electron beam induced deposition.

4. 2. Experimental

A custom-built ultrahigh vacuum (UHV) chamber with a baseline pressure of about 3×10^{-9} torr was utilized to study the effects of electron irradiation on nanometer thick films of three different iron containing, organometallic compounds. The chamber was equipped with a mass spectrometer, low energy electron source and X-Ray photoelectron spectrometer. A detailed description of this instrument, along with its analytical capabilities, can be found in previous publications[17, 18].

Precursors:

Iron pentacarbonyl ($Fe(CO)_5$; >99.99%, CAS: 13463-40-6, Sigma-Aldrich), diiron nonacarbonyl ($Fe_2(CO)_9$; 99%, CAS: 15321-51-4, Strem Chemicals, Inc.), and triiron dodecacarbonyl ($Fe_3(CO)_{12}$; 95% (5-10% methanol), CAS: 17685-52-8, Strem Chemicals, Inc.) were chosen as the precursors for this experiment. Due to their reactivity in air, an anaerobic environment was utilized to load each compound into an airtight stainless-steel container mounted to the inlet of a leak valve. After loading, the leak valves were mounted to the UHV chamber and

the organometallic complex subsequently underwent multiple freeze-pump-thaw cycles. The presence of impurities and contaminants was checked by an RGA attached to the UHV chamber.

Creating Films:

Nanometer scale films of $Fe(CO)_5$, $Fe_2(CO)_9$ and $Fe_3(CO)_{12}$ were created by leaking the corresponding precursor through a UHV-compatible leak valve and depositing the precursors onto a cooled, 1cm x 1cm, polycrystalline Au substrate. The $Fe_2(CO)_9$ and $Fe_3(CO)_{12}$ compounds were heated to 50°C and 80°C respectively to improve their vapor pressure during dosing. Iron pentacarbonyl, however, was sufficiently volatile to be dosed at room temperature. All three compounds were dosed at a pressure of about 5×10^{-7} torr. It took about 10-15 minutes to create the 1-2nm film for $Fe(CO)_5$. $Fe_2(CO)_9$ required 30-40 minutes of dose and $Fe_3(CO)_{12}$ required 45-50 minutes. To induce adsorption of the precursor, the substrate needed to be cooled. Preliminary dosing tests revealed -130°C was the best substrate temperature for $Fe(CO)_5$ and -80°C was determined to be the best for the multi-metallic precursors. The average film thickness was obtained by measuring the attenuation of the Au substrate 4f photoelectrons upon film deposition. Deposited films were exposed to varying doses of 500 eV electrons produced by a low energy charge neutralizer. Dosage was monitored by connecting the substrate to a Keithley 6485 picoammeter. The substrate was biased with 20V to ensure no secondary electrons were lost during exposure. Changes in the surface composition and bonding within the films were monitored in situ with XPS.

4. 3. Results and Discussion

$Fe(CO)_5$:

Changes in the C(1s), O(1s), and Fe($2p_{3/2}$) regions of nanometer thick $Fe(CO)_5$ films exposed to 500eV electrons can be found in Figure 4.1. Prior to irradiation, the C(1s) region consists of two peaks at binding energies of ≈ 287.1eV and 292.7 eV. The lower energy, higher intensity peak corresponds to the C(1s) line for CO ligands in $Fe(CO)_5$[23, 24]. The higher energy peak is a shake-up feature associated with π-π* transitions[23, 24]. These can accompany C(1s) core level excitations in metal carbonyls. Examination of Figure 4.1 shows that, for electron doses ≤ 2.25 x 10^{16} e^-/cm^2, changes in the C(1s) region are characterized solely by a decrease in intensity of both peaks. As the electron dose exceeds 2.25 x 10^{16} e^-/cm^2, the continued decrease in both CO peak intensity is now accompanied by the appearance of a new peak centered around 284.5 eV. This peak is indicative of graphitic carbon, whose intensity continues to increase as a function of electron dose[25-28]. Analysis of the C(1s) region indicates that the integrated spectral intensity within the C(1s) region decreases by 50-60% of initial value after an electron dose of ≈ 2.25 x 10^{16} e^-/cm^2 but remains constant thereafter (filled blue circles in Figure 4.2). The lack of change in overall carbon signal indicates that, for doses exceeding 2.25 x 10^{16} e^-/cm^2, there is no further loss in carbon from the $Fe(CO)_5$ film.

Like the C(1s) region, the as deposited O(1s) region is composed of two peaks centered around 533.5 eV and 539.1 eV. These peaks are associated with the O(1s) CO ligand and π-π* shake up features respectively[23, 24]. Similar to the C(1s) region, electron doses ≤ 2.25 x 10^{16} e^-/cm^2 lead to a decrease in intensity of both O(1s) peaks. Above 2.25 x 10^{16} e^-/cm^2, the intensity of both CO peaks continues but is now accompanied by the appearance of a new peak centered around 530.8 eV which grows in intensity as the electron dose increases. The binding energy of this peak

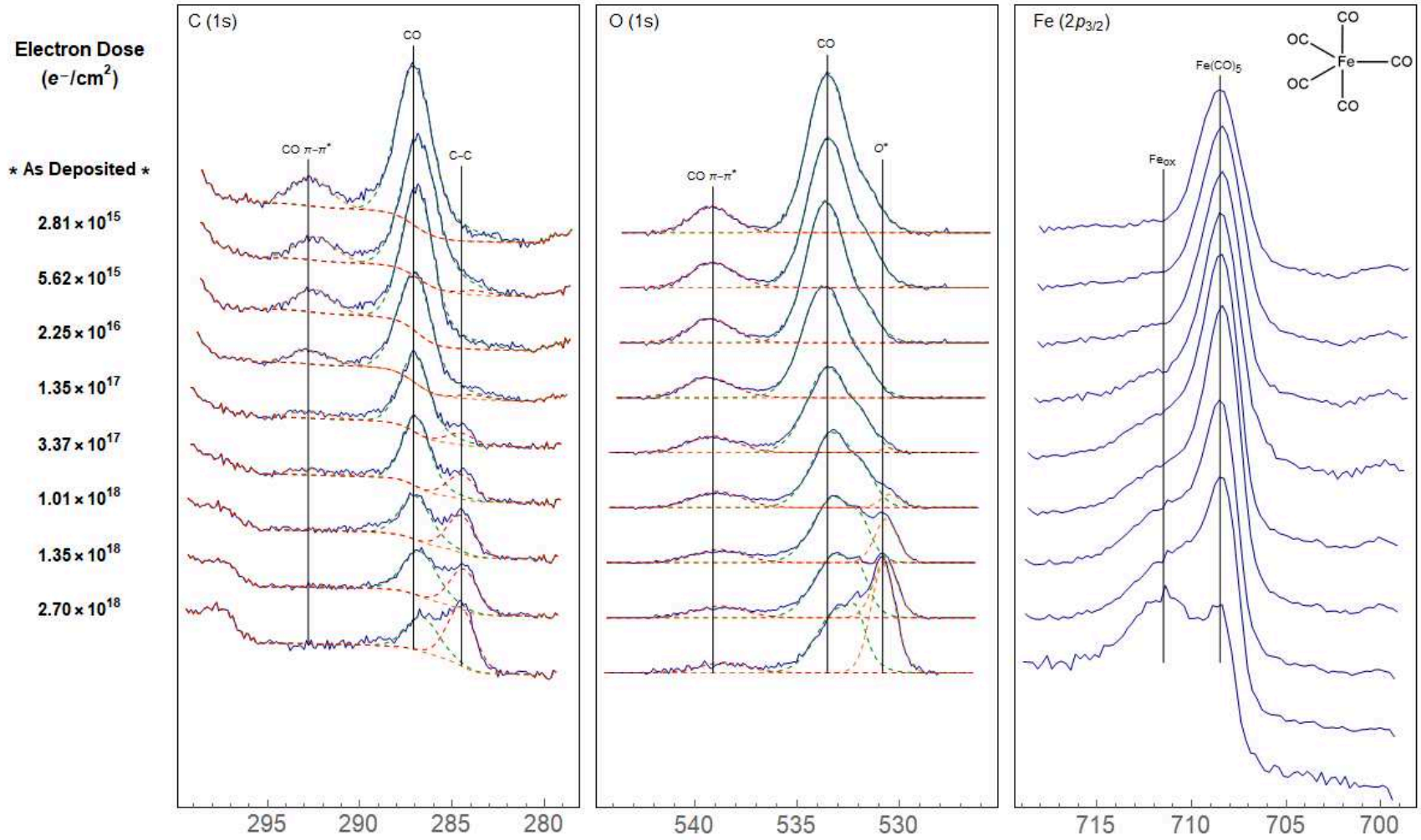

Figure 4. 1: Evolution of the C(1s), O(1s), and Fe($2p_{3/2}$) XP regions for 1-2 nm thick films of $Fe(CO)_5$ exposed to electron doses ≤ 2.70 x 10^{18} e^-/cm^2.

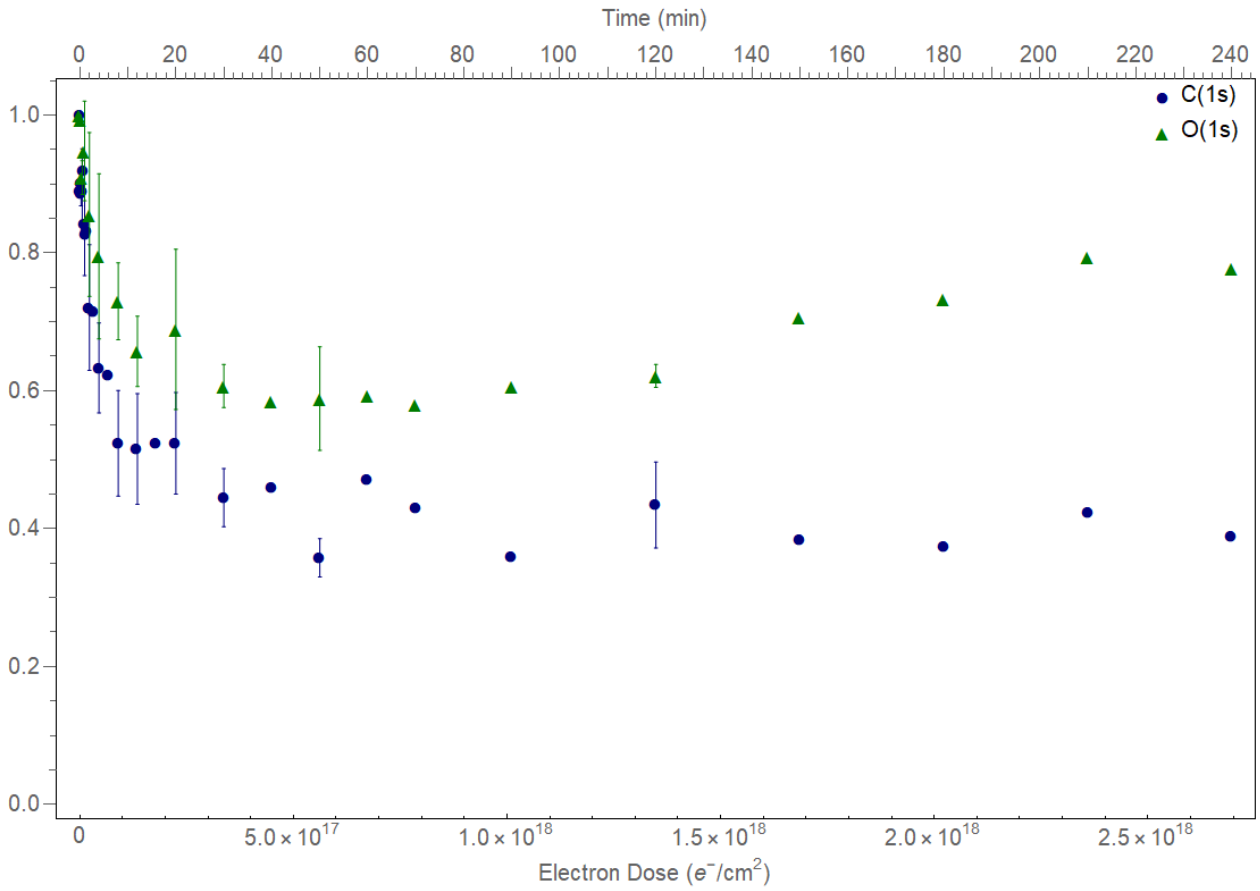

Figure 4. 2: C(1s) (blue circles) and O(1s) (green triangles) integrated peak areas and corresponding error bars for $Fe(CO)_5$ films exposed to electron doses $\leq 2.70 \times 10^{18}$ e^-/cm^2.

is characteristic of oxide formation. The integrated area in the O(1s) region initially decreases by ≈ 40% after an electron dose of ≈ 2.25 x 10^{16} e^-/cm^2 (filled green triangles Figure 4.2). Past this threshold, the area increases steadily. At the end of the exposure, 2.30 x 10^{18} e^-/cm^2, only a 20% reduction in the overall O(1s) signal is observed. The lack of growth in Fe, Au, or C signal, along with a lack of any other elements, indicates that this increase in oxygen is likely due to iron oxidation induced by residual water in the chamber (< 10^{-9} torr, as measured by the RGA). This effect has been observed in previous experiments where the substrate is cooled to a sufficient temp[29, 30].

Prior to irradiation, the Fe($2p_{3/2}$) region is composed of a single peak centered around 708.5 eV, which can be ascribed to $Fe(CO)_5$. Below 2.25 x 10^{16} e^-/cm^2 no changes are observed. However, as the electron dose exceeds 2.25 x 10^{16} e^-/cm^2, changes in the Fe($2p_{3/2}$) region are characterized by a peak broadening to a higher binding energy associated with the growth of a second peak centered around 711.5 eV, characteristic of an iron oxide. Analysis of the integrated area within the Fe($2p_{3/2}$) region reveals that the Fe peak area remains constant. Consequently, it can be assumed that little to no iron desorbs from the substrate. The lack of iron loss indicates that electron stimulated desorption is not observed for $Fe(CO)_5$ when exposed to 500 eV electrons.

Electron Stimulated Reactions of $Fe(CO)_5$:

Previous studies on metal carbonyl precursors have proposed a two-step reaction mechanism describing the electron stimulated decomposition[14, 16, 17, 19, 31]. From this precedent, the following mechanism was modified to describe the decomposition of $Fe(CO)_5$.

$$Fe(CO)_5 + e^- \xrightarrow{k_1} Fe(CO)_{5-x} + x(CO) \quad (4.1)$$

$$Fe(CO)_{5-x} + e^- \xrightarrow{k_2} Fe_yO_z + (5-x)C_{graphitic} \quad (4.2)$$

Examination of the results reveals that the experimentally observed chemical changes agree with and support the proposed two-step reaction mechanism. For electron doses < 2.25 x 10^{16} e^-/cm^2 the only change observed for the C(1s) and O(1s) regions is a decrease in intensity. During this exposure regime, no change is observed in the Fe(2p) region. It follows that, prior to the 2.25 x 10^{16} e^-/cm^2 threshold, $Fe(CO)_5$ decomposes via the loss of several CO ligands. The average number of CO ligands lost is ascribed to the variable *x*. The observed chemical changes in this regime agree with the first step of the proposed reaction mechanism. For doses > 2.25 x 10^{16} e^-/cm^2, the accompaniment of the growth of an additional peak for both C(1s) and O(1s) indicates that the carbon and oxygen inside the deposits is being converted to graphitic carbon and an iron oxide species, respectively. The presence of an additional, oxidized iron peak in the Fe(2p) spectrum confirms the iron oxide theory. In addition, the lack of change in Fe(2p) and C(1s) total peak area throughout this regime indicates nothing is being lost or gained, simply transformed. These observations agree with the second step of the proposed reaction mechanism. It is worth noting that these chemical changes are consistent with those observed for other carbonyl containing organometallic precursors[9, 17, 20, 21].

The proposed mechanism suggests that the electron stimulated degradation pathway for $Fe(CO)_5$ can be described with two kinetic rate constants, k_1 and k_2. Using the experimental data plotted as a function of electron dose both rate constants can be derived and solved for. Based on Equation (4.1) from the proposed mechanism, we can write[1]:

$$[Fe(CO)_5]_t = [Fe(CO)_5]_0 * e^{-k_1 t} \quad (4.3)$$

[1] The variable t refers to the amount of time each film was exposed to a 30 μA beam of electrons and is equivalent to a corresponding dose of electrons. In relevant figures both time and equivalent electron dose are displayed.

Since there is no evidence of any loss of iron during electron irradiation we can write the following mass balance equation.

$$[Fe(CO)_5]_0 = [Fe(CO)_5]_t + [Fe(CO)_{5-x}]_t + [Fe_yO_z]_t \quad (4.4)$$

Recognizing that the carbon atom coverage is conserved in Equation (4.2) we can also write:

$$[C_{ads}]_t = 5[Fe(CO)_5]_t + (5-x)\left([Fe(CO)_{5-x}]_t + [Fe_yO_z]_t\right) \quad (4.5)$$

Substituting Equations (4.3) and (4.4) into Equation (4.5) and rearranging, yields the following equation.

$$[C_{ads}]_t = [Fe(CO)_5]_0 \left(xe^{-k1t} + (5-x)\right) \quad (4.6)$$

The coverage of adsorbed carbon atoms ($[C_{ads}]$) is directly proportional to the integrated C(1s) XPS area, $[C_{XPS}]$, such that $[C_{ads}] = A\,[C_{XPS}]$, where A is a proportionality constant. Thus:

$$[C_{ads}]_t = A\,[C_{XPS}]_t = [Fe(CO)_5]_0 \left(xe^{-k1t} + (5-x)\right) \quad (4.7)$$

At t= 0 the only form of carbon present initially is $Fe(CO)_5$. As a result, the following can be written where $A\,[C_{XPS}]_0$ represents the carbon area measured at t=0 by XPS.

$$[C_{ads}]_o = A\,[C_{XPS}]_0 = 5[Fe(CO)_5]_0 \quad (4.8)$$

Dividing Equation (4.6) by Equation (4.7) leads to the result;

$$\frac{[C_{XPS}]_t}{[C_{XPS}]_o} = \frac{x}{5}e^{-k1t} + \frac{(5-x)}{5} \quad (4.9)$$

Figure 4.3 shows a plot of $\frac{[C_{XPS}]_t}{[C_{XPS}]_o}$ vs time, from which we can determine best fit values of $k_1 = 0.004147\ s^{-1}$ and x = 2.8. *X* corresponds to the average number of volatile carbonyl ligands that are ejected from the thin film upon electron exposure. From the best fit values, about 3 ligands leave $Fe(CO)_5$ during the first step of the degradation mechanism.

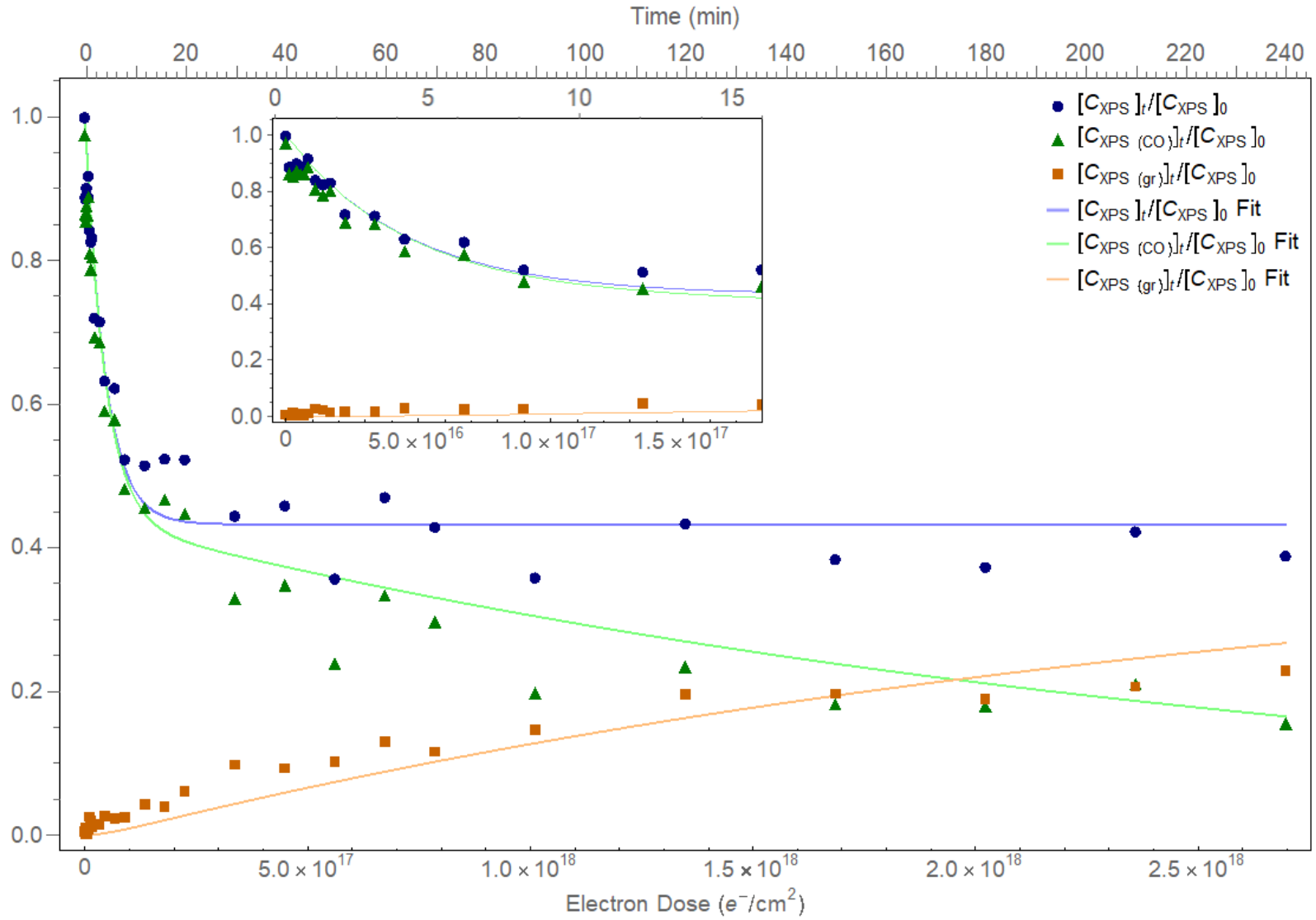

Figure 4. 3: Plots of the integrated C(1s) components and their corresponding fits for $Fe(CO)_5$ as a function of time and equivalent electron dose.

To obtain k_2, first principles were again used to derive a differential rate equation for $Fe(CO)_{5-x}$.

$$\frac{d[Fe(CO)_{5-x}]}{dt} = k_1[Fe(CO)_5]_t - k_2[Fe(CO)_{5-x}]_t \quad (4.10)$$

Substituting $[Fe(CO)_5]_t$ from Equation (4.3) and assuming $[Fe(CO)_{5-x}]_0$ is zero allows us to derive the following analytical solution for $[Fe(CO)_{5-x}]_t$.

$$[Fe(CO)_{5-x}]_t = [Fe(CO)_5]_0 \frac{e^{-k_1 t}(e^{(k_1-k_2)t}-1)k_1}{k_1-k_2} \quad (4.11)$$

To determine k_2 the C(1s) spectral envelope must be decomposed into the contribution from graphitic carbon, $[C_{XPS(gr)}]$. Using CasaXPS, the C(1s) graphitic carbon peak was fit using a GL(30) peakshape. This fit was applied to the data for $Fe(CO)_5$ giving the concentration of graphitic carbon as a function of electron dose.

Based on Equation (4.2).

$$\left[C_{graphitic}\right]_t = A\,[C_{XPS(gr)}]_t = (5-x)\left[Fe_yO_z\right]_t \quad (4.12)$$

Using Equations (4.3), (4.4), and (4.11) we can rewrite $[Fe_yO_z]_t$ as;

$$[Fe_yO_z]_t = [Fe(CO)_5]_0\left(1 - e^{-k1t} - \frac{e^{-k_1 t}(e^{(k_1-k_2)t}-1)k_1}{k_1-k_2}\right) \quad (4.13)$$

The XPS area associated with graphitic carbon ($[C_{XPS(gr)}]_t$) can be determined experimentally as a fraction of the initial carbon area, $[C_{XPS}]_0$. By substituting Equation (4.13) into (4.12) and using Equation (4.8), we can derive the relationship;

$$\frac{[C_{XPS(gr)}]_t}{[C_{XPS}]_o} = \frac{(5-x)}{5}\left(1 - e^{-k1t} - \frac{e^{-k_1 t}(e^{(k_1-k_2)t}-1)k_1}{k_1-k_2}\right) \quad (4.14)$$

Using the previously determined values of k_1 and x, the expression can be solved with Mathematica to give $k_2 = 0.000068\ s^{-1}$.

With knowledge of k_1, k_2 and x the variation in the fractional change for the integrated carbon signal as well as the contributions to this signal from the CO and graphitic carbon

components can be determined. Results from this analysis are plotted in Figure 4.3 and seem to agree well with the corresponding values determined experimentally from the complete XPS data set; also plotted in Figure 4.3. In addition, since k_1, k_2, and *x* are known, the variation in $[Fe(CO)_5]_t$, $[Fe(CO)_{5-x}]_t$ and $[Fe_yO_z]_t$ can be plotted as a function of time and electron dose, Figure 4.4.

$Fe_2(CO)_9$ and $Fe_3(CO)_{12}$:

Changes in the C(1s), O(1s), and Fe($2p_{3/2}$) regions of nanometer thick $Fe_2(CO)_9$ and $Fe_3(CO)_{12}$ films exposed to 500eV electrons can be found in Figure 4.5. The effect of electron irradiation on the C(1s), O(1s), and Fe($2p_{3/2}$) regions for both molecules are qualitatively similar to those shown for $Fe(CO)_5$. In the case of $Fe_2(CO)_9$, electron exposure initially leads to a decrease in the intensity within the C(1s) and O(1s) regions without any significant changes in the shapes of the spectral envelopes. However, for electron doses in excess of 1.35×10^{15} e^-/cm^2 the loss of intensity associated with the CO species is now accompanied by the appearance of new spectral features; a graphitic carbon peak at ≈285.2 eV in the C(1s) region and an oxide species in the O(1s) region centered at ≈ 530.9 eV. Upon electron irradiation the Fe($2p_{3/2}$) region is observed to initially broaden to higher binding energies before a distinct shoulder with a peak centered around 711.8 eV is observed, characteristic of iron oxide formation.

Just like $Fe_2(CO)_9$ and $Fe(CO)_5$, $Fe_3(CO)_{12}$ follows the same trend. For electron doses below 2.81×10^{15} e^-/cm^2 changes in the C(1s) and O(1s) region are similarly limited to a decrease in intensity. Above this threshold, the continued loss of intensity is accompanied by the introduction of new spectral features. For C(1s), the graphitic carbon peak appears at ≈284.8 eV. For the O(1s) region, the oxide species peak appears around ≈531.1 eV. Just like $Fe_2(CO)_9$, the

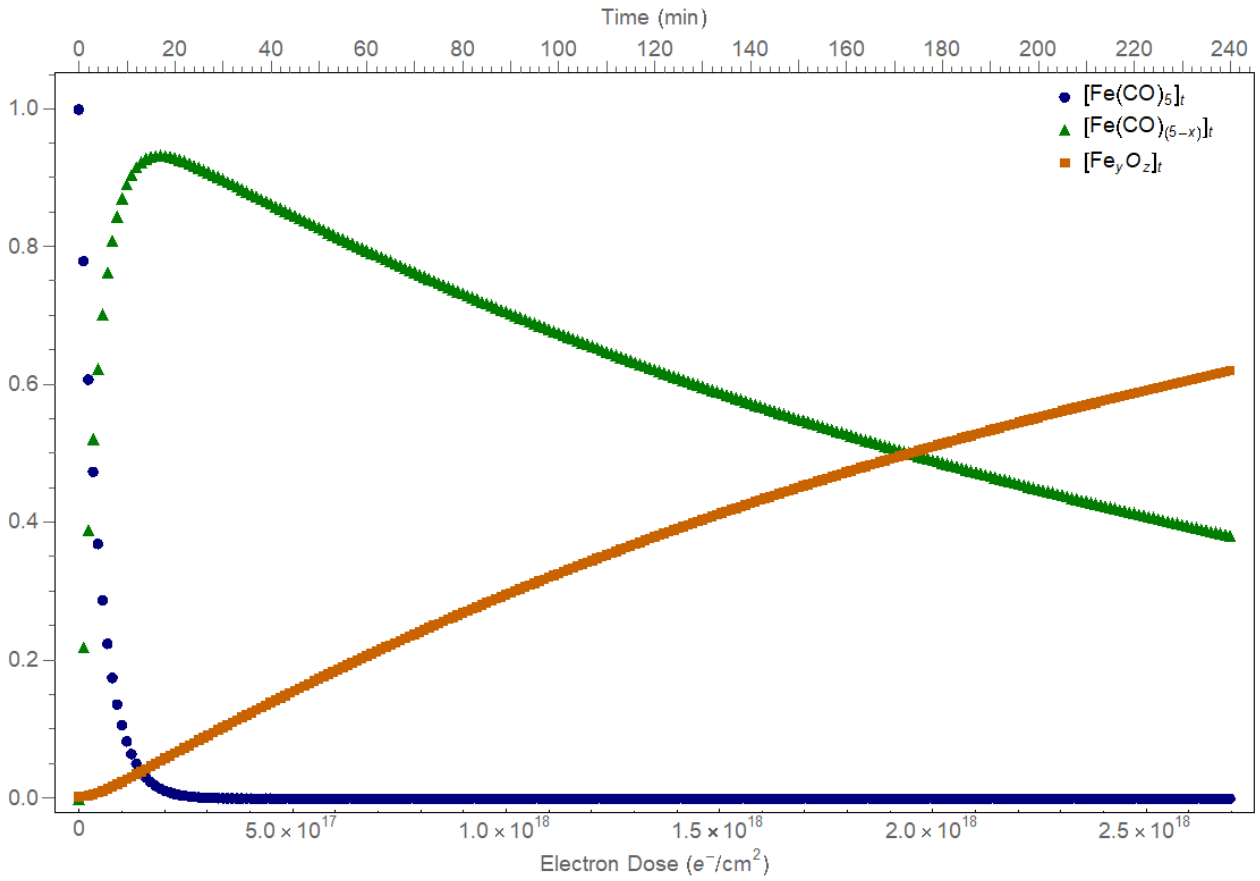

Figure 4. 4: Plots of the concentration of each iron species for $Fe(CO)_5$ as modeled using differential rate equations, *x*, and the rate constants k_1 and k_2.

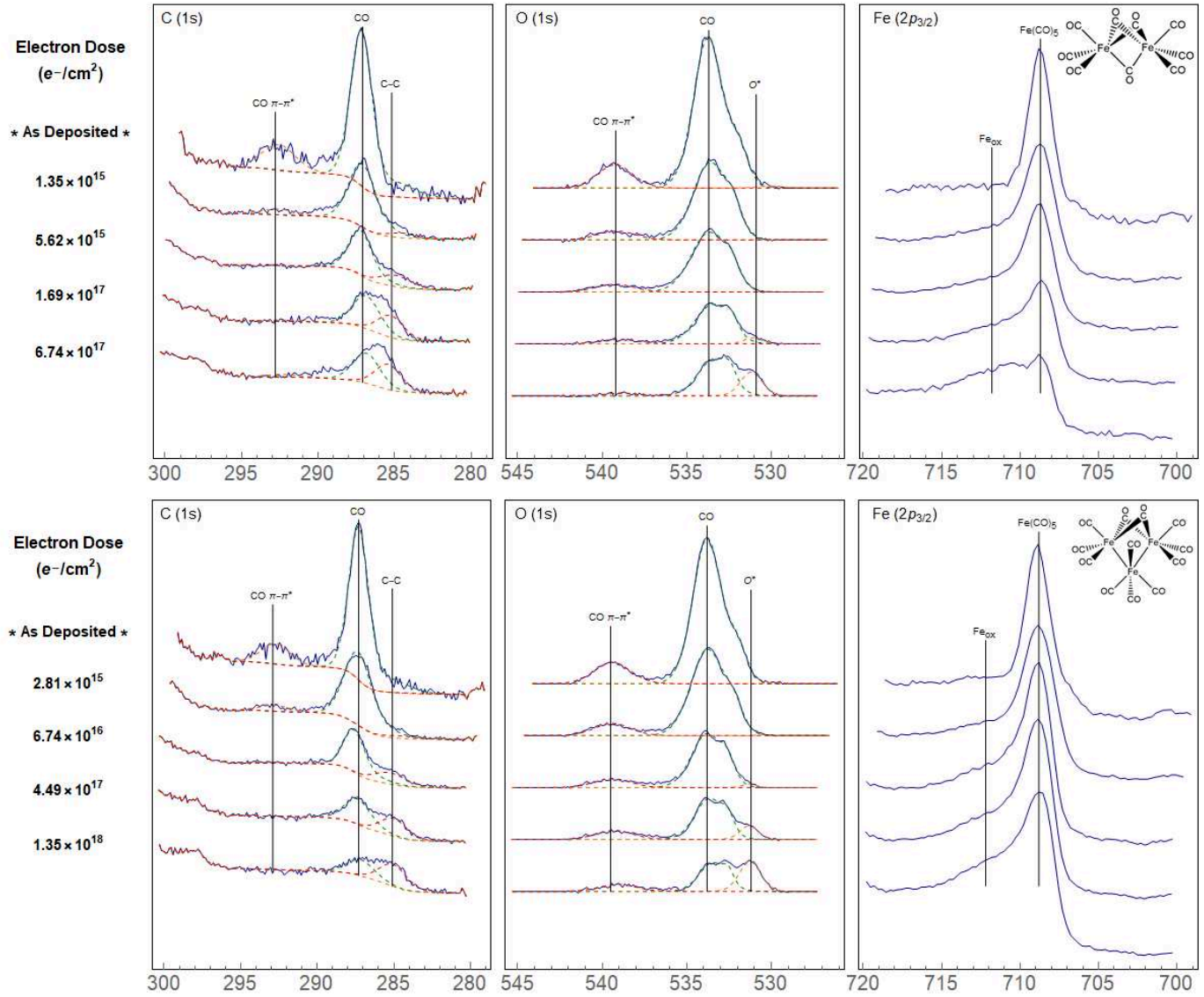

Figure 4. 5: Evolution of the C(1s), O(1s), and Fe($2p_{3/2}$) XP regions for 1-2 nm thick films of $Fe_2(CO)_9$ (top) and $Fe_3(CO)_{12}$ (bottom) exposed to electron doses ≤ 6.74 x 10^{17} e^-/cm^2 and ≤ 1.35 x 10^{18} e^-/cm^2 respectively.

Fe(2p3/2) region, upon electron irradiation appears to broaden slightly to higher binding energies. Just like the other compounds, as the electron dose exceeds the 2.81 x 10^{15} e^-/cm^2 threshold, a characteristic iron oxide formation is observed to grow, centered around 712.8 eV.

It is clear, upon comparison, the 500 eV electrons induce similar changes in all three iron carbonyl compounds. Both $Fe_2(CO)_9$ and $Fe_3(CO)_{12}$ seem to follow the same two-step reaction mechanism proposed for $Fe(CO)_5$. Electron doses below a certain threshold (1.35 x 10^{15} e^-/cm^2 and 2.81 x 10^{15} e^-/cm^2 for $Fe_2(CO)_9$ and $Fe_3(CO)_{12}$ respectively) result in a loss of C(1s) and O(1s) regions but no change in the Fe(2p) region. This is characteristic of the same carbonyl loss observed in $Fe(CO)_5$. Additionally, past these thresholds, both $Fe_2(CO)_9$ and $Fe_3(CO)_{12}$ show the growth of additional peaks corresponding to graphitic carbon and iron oxide (evident in both O(1s) and $Fe(2p_{3/2})$ regions). Comparing the requisite thresholds of all three compounds indicates that the termination of CO emission occurs at different electron doses, with $Fe(CO)_5$ stopping at a dose of around 2.25 x 10^{16} e^-/cm^2 while $Fe_2(CO)_9$ and $Fe_3(CO)_{12}$ terminates at an order of magnitude lower, 1.35 x 10^{15} e^-/cm^2 and 2.81 x 10^{15} e^-/cm^2 respectively. To better compare these findings, the integrated C(1s) areas obtained for all three compounds were plotted on top of one another in Figure 4.6. Examination of these dose curves confirms the observation that multi-metallic emit CO at a faster rate implying an even larger k_1 than that measured for $Fe(CO)_5$. However, statistically, the overall loss in carbon is identical for all three compounds, leveling off at a loss of between 50-60%. While this corresponds to an average loss of about 6 and 8 CO ligands for $Fe_2(CO)_9$ and $Fe_3(CO)_{12}$ respectively, at least for iron carbonyl compounds, the number of metallic atoms does not decrease the overall organic contamination leftover in the EBID process.

In principle, low energy electrons generated by the X-ray gun could also contribute to the observed changes in the composition and bonding within the adsorbate layer. To this end extended

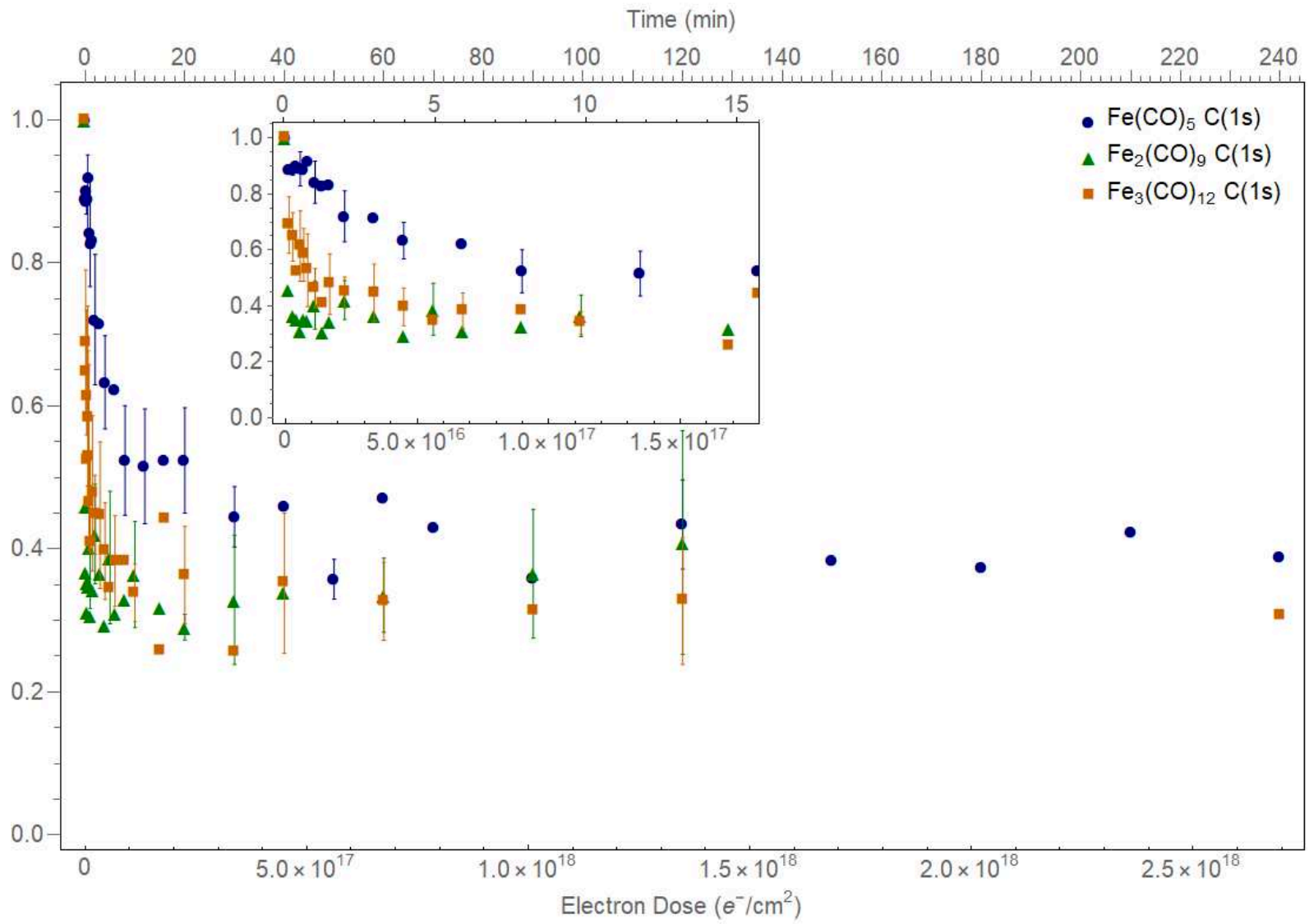

Figure 4. 6: C(1s) integrated peak areas and corresponding error bars for $Fe(CO)_5$ (blue circles), $Fe_2(CO)_9$ (green triangles), and $Fe_3(CO)_{12}$ (orange squares) films exposed to electron doses $\leq 2.70 \times 10^{18}$ e^-/cm^2

X-ray exposure studies were conducted and can be found in Figures 4.7 through 4.10. As shown in Figures 4.7 through 4.9, the effects of x-rays were slight. Measurable changes to the peakshape for all of the three compounds ($Fe(CO)_5$, $Fe_2(CO)_9$, and $Fe_3(CO)_{12}$) only occurred after significant x-ray exposure. While Figure 4.10 shows that all three precursors were somewhat sensitive to x-ray induced CO loss, Figure 4.6 shows they were significantly more sensitive to electron-induced CO loss. Practically this meant that for all three compounds, the smallest dose of electrons had surpassed the effects expected from the x-ray source. Consequently, for these iron carbonyl films exposed to 500 eV electrons, all changes observed in the photoelectron spectra can be attributed to the effect of the incident electrons.

Effects of Annealing on $Fe(CO)_5$ and $Fe_3(CO)_{12}$:

In an attempt to induce further carbonyl loss and improve the purity of the iron carbonyl deposits, annealing experiments were performed on electron exposed $Fe(CO)_5$ and $Fe_3(CO)_{12}$ films. Each compound was adsorbed onto the chilled substrate (-130°C and -80°C for $Fe(CO)_5$ and $Fe_3(CO)_{12}$ respectively), exposed to a set dose of electrons, and subsequently annealed to a temperature of 30°C. XPS spectra were taken at each step of the process to track the chemical changes induced by electrons and the annealing step. Two different dosing thresholds were chosen; the first corresponded to a high electron fluence (2.70×10^{18} e^-/cm^2) while the second corresponded the threshold at which carbonyl loss had sufficiently terminated (2.25×10^{17} e^-/cm^2).

Examination of the results showed that beginning the annealing step after a sufficiently high fluence of electrons (2.70×10^{18} e^-/cm^2) resulted in no measurable change in the either the $Fe(CO)_5$ and $Fe_3(CO)_{12}$ films. This is consistent with similar annealing experiments performed on $W(CO)_6$ by Rosenberg et al[30] which showed that adsorbed $W(CO)_6$ films, sufficiently decomposed

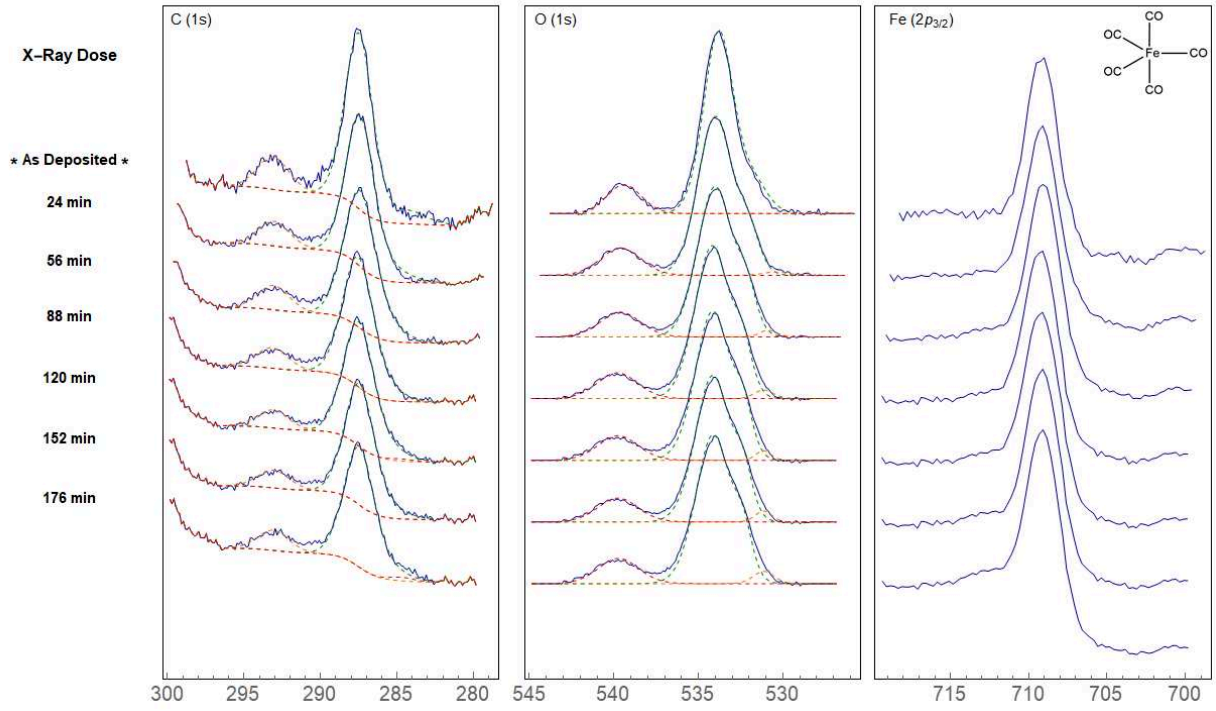

Figure 4. 7: Evolution of the C(1s), O(1s), and Fe($2p_{3/2}$) XP regions for 1-2 nm thick films of $Fe(CO)_5$ exposed to the XPS x-ray source.

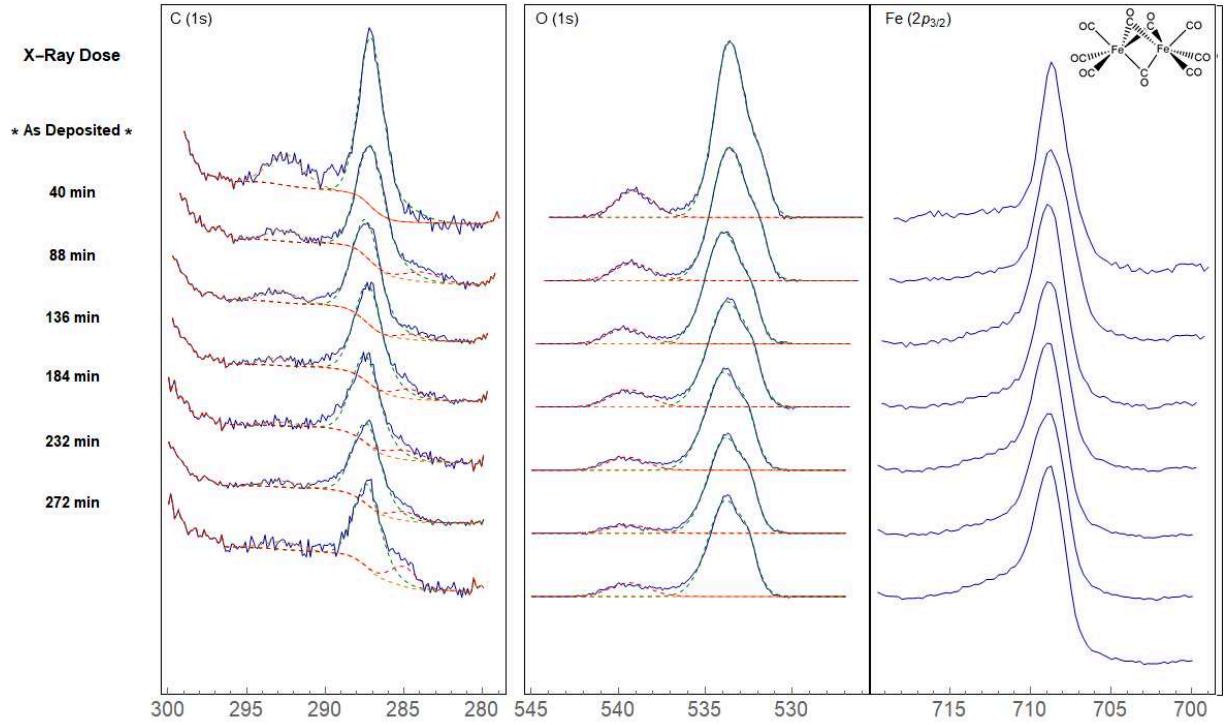

Figure 4. 8: Evolution of the C(1s), O(1s), and Fe($2p_{3/2}$) XP regions for 1-2 nm thick films of $Fe_2(CO)_9$ exposed to the XPS x-ray source.

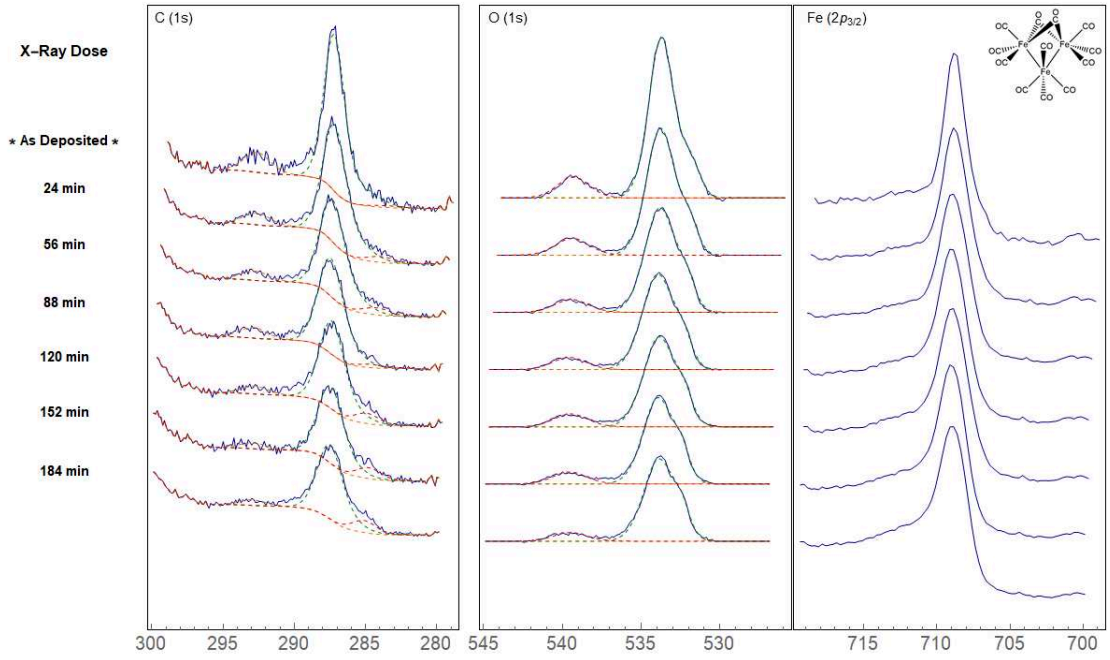

Figure 4. 9: Evolution of the C(1s), O(1s), and Fe($2p_{3/2}$) XP regions for 1-2 nm thick films of $Fe_3(CO)_{12}$ exposed to the XPS x-ray source.

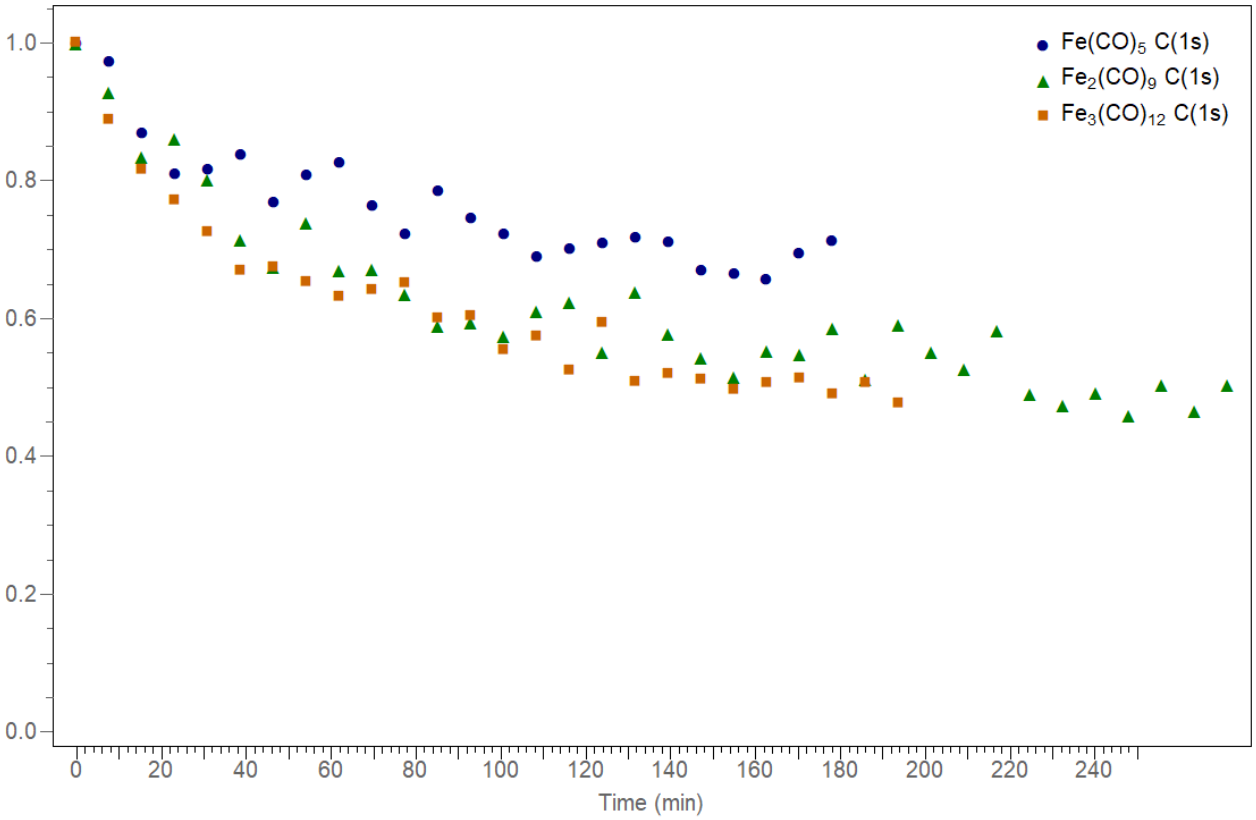

Figure 4. 10: C(1s) integrated peak areas for $Fe(CO)_5$ (blue circles), $Fe_2(CO)_9$ (green triangles), and $Fe_3(CO)_{12}$ (orange squares) films exposed to the XPS x-ray source for varying durations.

by electron adsorbate interactions, were no longer able to emit carbon and oxygen in form of carbonyl gas. Contrastingly, results from the lower dosed annealing experiments showed a significant change in the XPS spectra of both $Fe(CO)_5$ and $Fe_3(CO)_{12}$ films (shown in Figure 4.11). After annealing, the C(1s) and O(1s) spectral components attributed to CO disappear leaving only small contributions characteristic of the graphitic carbon and oxidized iron (C(1s) and O(1s) respectively) observed in the earlier experiments. The subsequent loss of both carbon and oxygen is characteristic of further carbonyl loss from the films. This is supported by similar annealing studies performed on $W(CO)_6$ which revealed that annealing, performed before the electron fluence was sufficient to decompose carbonyl ligands, resulted in further ligand removal[30].

Examination of the $Fe(2p_{3/2})$ peak reveals that the annealing process left behind at least two distinct forms of iron. The first, and less intense component (≈ 712 eV) corresponds to the same oxidized species observed after large doses of electrons. The second, dominant peak, at ≈ 708.2 eV is characteristic of metallic iron[32]. The heat induced ligand loss appears to be similarly effective for both $Fe(CO)_5$ and $Fe_3(CO)_{12}$ compounds.

Iron Carbonyl Compounds and EBID:

As alluded to earlier, EBID studies on these compounds have yielded a wide range of metallic percentages depending on the deposition conditions. Compositional EBID studies with $Fe(CO)_5$ and $Fe_2(CO)_9$ have produced deposits with iron purities ranging from 50% to 90% depending on the conditions[5-7, 11]. The observations provided by this study can help elucidate the reasons behind this wide range in deposit purity.

Most EBID experiments are conducted in a slightly modified SEM, with the substrate sitting at room temperature. The low temperature experiments (< -80°C) conducted here were at

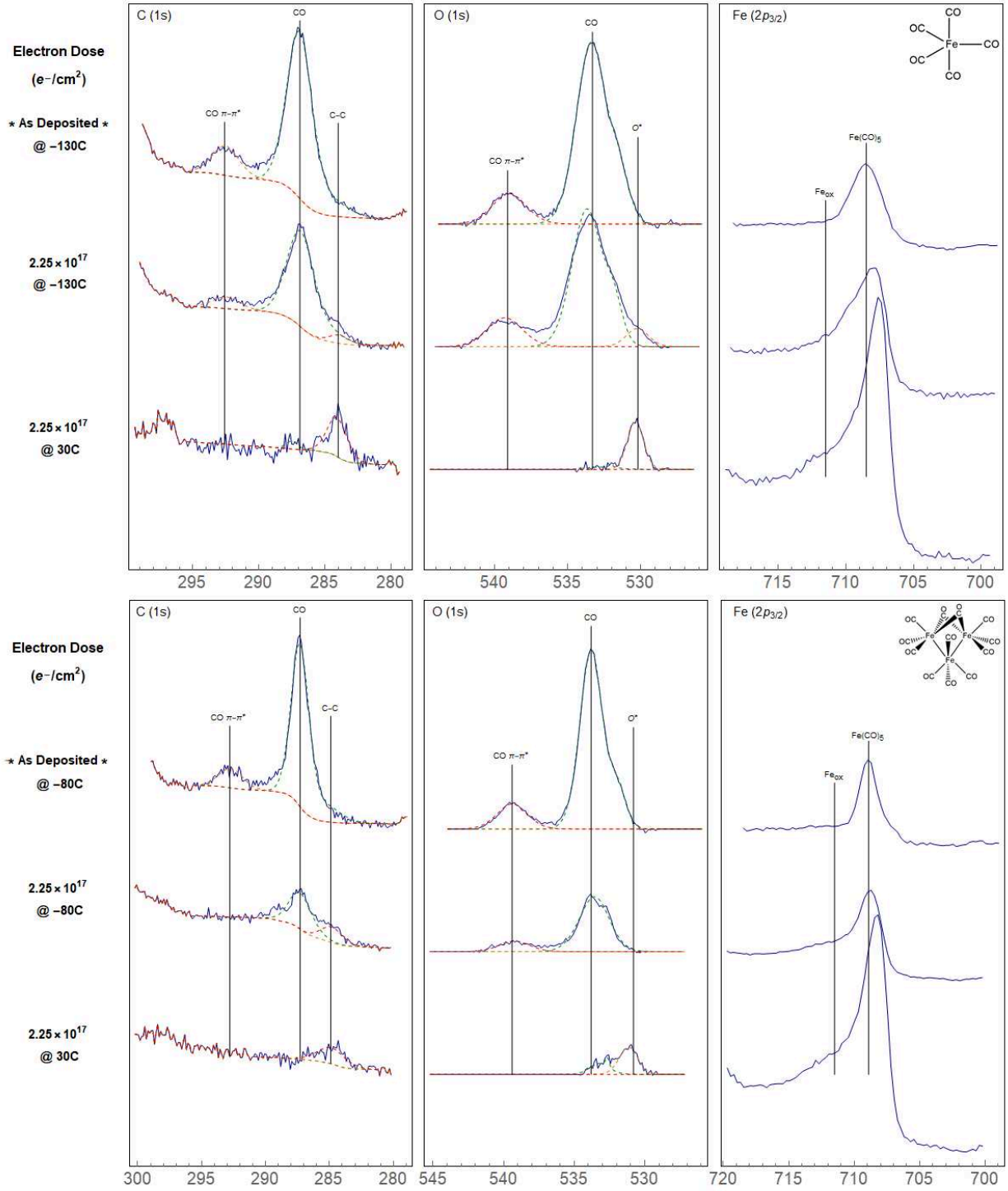

Figure 4.11:. Evolution of the C(1s), O(1s), and Fe($2p_{3/2}$) XP regions for 1-2 nm thick films of $Fe(CO)_5$ (top) and $Fe_3(CO)_{12}$ (bottom) exposed to an electron dose of 2.25 x 10^{17} e^-/cm^2 and subsequently annealed to 30°C.

temperatures sufficient to suppress the surface adsorption dynamics of the precursors as well as any thermal reactions that might take place. Consequently, to compare the results obtained here with those expected in EBID, the two-step reaction mechanism must be expanded to include the adsorption dynamics of the precursor as well as any thermal reactions that might also take place.

The cold substrate allowed the formation of an iron carbonyl film prior to electron exposure and sufficiently suppressed any gas-phase adsorption equilibrium. In EBID, with a room-temperature substrate, the initial reaction step is preceded by the equilibrium of the gas-phase precursor with the surface adsorbed species. Previous EBID adsorption studies have shown this equilibrium to be consistent with a Langmuir-type isotherm[1, 33]. While the equilibrium constant (k_{eq}) will be different for each iron carbonyl precursor, the following equation holds true for all three where n and m correspond to the number of ligands and iron species in each compound.

$$Fe_n(CO)_{m\,(g)} \overset{k_{eq}}{\leftrightarrow} Fe_n(CO)_{m\,(ads)} \quad (4.15)$$

The ability to fit the $Fe(CO)_5$ experimental data with the kinetic model supports the two-step reaction mechanism proposed in Equations (4.1) and (4.2). Furthermore, qualitative comparisons between the functional forms of the $Fe_2(CO)_9$ and $Fe_3(CO)_{12}$ data show that while the rate of CO loss and decomposition of each precursor is different, the extent and mechanism of CO loss is similar. Consequently, the following general form equations can be written.

$$Fe_n(CO)_{m\,(ads)} + e^- \overset{k_1}{\rightarrow} Fe_n(CO)_{(m-x)} + x(CO)_{(g)} \quad (4.16)$$

$$Fe_n(CO)_{(m-x)} + e^- \overset{k_2}{\rightarrow} Fe_yO_z + (m-x)C_{graphitic} \quad (4.17)$$

A key finding of the kinetic model is the fact that $k_1 >> k_2$ by at least several orders of magnitude. This means that the rate of decomposition (Equation 4.16) is much slower than that of CO loss (4.17). Consequently, in EBID conditions, the $Fe_n(CO)_{(m-x)}$ partially decarbonylated

species will be relative long lived for all iron carbonyl precursors. This has strong implications for thermal effects that occur at room temperatures.

Experiments, performed on $Fe(CO)_5$ and $Fe_3(CO)_{12}$ showed that annealing to room temperature had two contrastingly different results depending on the electron dose of the corresponding film. For sufficiently decomposed films (high electron dose), there was no observable change in composition after the annealing step, implying that the Fe_yO_z and graphitic carbon species left over are relatively invariant to thermal effects at room temperature. However, films with large concentrations of the partially decarbonylated species (low electron doses) showed an almost complete loss in carbon and oxygen upon annealing. This implies that these species, and by extension the precursors, will be susceptible to thermal desorption in room temperature EBID settings. Consequently, a third, competing, mechanism must be added to account for these effects.

$$Fe_n(CO)_{(m-x)} + \Delta \overset{k_3}{\rightarrow} Fe_n + (m-x)CO_{(g)} \quad (4.18)$$

The presence of the competing reactions in Equations (4.17) and (4.18) provides an explanation for why these metal carbonyls can, in certain situations, produce nearly pure iron deposits. The long lived partially decarbonylated species are susceptible to two different reaction pathways. In the presence of high doses of electrons, the electron stimulated decomposition of these intermediates dominates resulting in a large level of carbon and oxygen impurities. In contrast, lower doses of electrons allow these species to thermally degrade into the high purity iron structures.

Lastly, the oxygen data in Figure 4.2 showed that after a specific point, an oxygen increase was observed in the form of iron oxidation. As described in other studies, transiently adsorbed water can interact with electrons producing reactive oxygen species (ROS) which can facilitate metal atom oxidation accordingly[30].

$$H_2O_{(g)} \leftrightarrow H_2O_{(ads)} + e^- \rightarrow ROS + Fe \rightarrow Fe_xO_y \quad (4.19)$$

While the cold substrate featured here artificially amplified the effects of this phenomenon through an increased adsorption rate, EBID chambers are commonly known for their high partial pressures of water (~10^{-6} torr regime). This makes the iron species particularly susceptible to oxidation from water in the background.

4. 4. Conclusions

This study characterized the effects of 500 eV electrons on several adsorbed iron carbonyl precursors, $Fe(CO)_5$, $Fe_2(CO)_9$, and $Fe_3(CO)_{12}$. The results were shown to be consistent with previous metal carbonyl studies, indicating that the electron induced deposition of these species is a two-step mechanism that begins with the creation of partially decarbonylated species through CO emission and ends with the electron stimulated decomposition of the remaining CO species to produce a metal (in this case iron) oxide and graphitic carbon. To this end, a kinetic model based on this two-step mechanism was created and successfully fit to the data obtained for $Fe(CO)_5$ showing that the production of partially decarbonylated iron species proceeds at a much faster rate than the electron stimulated decomposition, $k_1 = 0.004147\ s^{-1}$ and $k_2 = 0.000068\ s^{-1}$ respectively.

Functional similarities between all three compounds confirmed that $Fe_2(CO)_9$ and $Fe_3(CO)_{12}$ shared similar reaction pathways with $Fe(CO)_5$. Additionally, these comparisons showed that while the rates of decomposition are precursor dependent, the extent of CO loss in this step is effectively similar for all three compounds. Further experiments with $Fe(CO)_5$ and $Fe_3(CO)_{12}$ showed that annealing the cooled substrate to room temperature resulted in almost complete CO loss for films with significant concentrations of partially decarbonylated species, yet showed no discernable difference in films that had undergone significant electron-induced

decomposition of the CO ligands. Lastly, a comparison between conditions surrounding these experiments and those found in EBID experiments illuminated the wide range of deposition purity for iron carbonyl compounds. The susceptibility of partially decarbonylated species to thermal reactions at room temperature is suspected to allow the creation of high purity deposits in situations where the electron dose is sufficiently small. Contrastingly, for high electron doses, electron-induced carbonyl decomposition dominates creating iron oxide and graphitic carbon. These high electron dose situations also introduce the possibility of ROS creation inducing further iron oxidation.

4. 5. References

1. Utke, I.; Hoffmann, P.; Melngailis, J., Gas-assisted focused electron beam and ion beam processing and fabrication. *Journal of Vacuum Science & Technology B: Microelectronics and Nanometer Structures Processing, Measurement, and Phenomena* **2008,** *26* (4), 1197-1276.
2. Gonzalez, C. M.; Slingenbergh, W.; Timilsina, R.; Noh, J.-H.; Stanford, M. G.; Lewis, B. B.; Klein, K. L.; Liang, T.; Fowlkes, J. D.; Rack, P. D. In *Evaluation of mask repair strategies via focused electron, helium, and neon beam induced processing for EUV applications*, SPIE Advanced Lithography, SPIE: 2014; p 7.
3. Utke, I.; Dwir, B.; Leifer, K.; Cicoira, F.; Doppelt, P.; Hoffmann, P.; Kapon, E., Electron beam induced deposition of metallic tips and wires for microelectronics applications. *Microelectronic Engineering* **2000,** *53* (1), 261-264.
4. Utke, I.; Hoffmann, P.; Dwir, B.; Leifer, K.; Kapon, E.; Doppelt, P., Focused electron beam induced deposition of gold. *Journal of Vacuum Science & Technology B: Microelectronics and Nanometer Structures Processing, Measurement, and Phenomena* **2000,** *18* (6), 3168-3171.
5. Córdoba, R.; Han, D. S.; Koopmans, B., Manipulating the switching in modulated iron nanowires grown by focused electron beam induced deposition. *Microelectronic Engineering* **2016,** *153*, 60-65.
6. Hochleitner, G.; Wanzenboeck, H. D.; Bertagnolli, E., Electron beam induced deposition of iron nanostructures. *Journal of Vacuum Science & Technology B: Microelectronics and Nanometer Structures Processing, Measurement, and Phenomena* **2008,** *26* (3), 939-944.
7. Lukasczyk, T.; Schirmer, M.; Steinrück, H.-P.; Marbach, H., Electron-Beam-Induced Deposition in Ultrahigh Vacuum: Lithographic Fabrication of Clean Iron Nanostructures. *Small* **2008,** *4* (6), 841-846.
8. Masaki, T.; Masayuki, S.; Kazuo, F., Nanostructure Fabrication by Electron-Beam-Induced Deposition with Metal Carbonyl Precursor and Water Vapor. *Japanese Journal of Applied Physics* **2007,** *46* (9S), 6183.
9. Bruk, M. A.; Zhikharev, E. N.; Grigor'ev, E. I.; Spirin, A. V.; Kal'nov, V. A.; Kardash, I. E., Focused electron beam-induced deposition of iron- and carbon-containing nanostructures from triiron dodecacarbonyl vapor. *High Energy Chemistry* **2005,** *39* (2), 65-68.

10. Schirmer, M.; Walz, M. M.; Papp, C.; Kronast, F.; Gray, A. X.; Balke, B.; Cramm, S.; Fadley, C. S.; Steinrück, H. P.; Marbach, H., Fabrication of layered nanostructures by successive electron beam induced deposition with two precursors: protective capping of metallic iron structures. *Nanotechnology* **2011,** *22* (47), 475304.
11. Lavrijsen, R.; Córdoba, R.; Schoenaker, F. J.; Ellis, T. H.; Barcones, B.; Kohlhepp, J. T.; Swagten, H. J. M.; Koopmans, B.; Teresa, J. M. D.; Magén, C.; Ibarra, M. R.; Trompenaars, P.; Mulders, J. J. L., Fe:O:C grown by focused-electron-beam-induced deposition: magnetic and electric properties. *Nanotechnology* **2011,** *22* (2), 025302.
12. Pfeiffer, B.; Erichsen, T.; Epler, E.; Volkert, C. A.; Trompenaars, P.; Nowak, C., Characterization of Nanoporous Materials with Atom Probe Tomography. *Microscopy and Microanalysis* **2015,** *21* (3), 557-563.
13. Beljaars, M. Electron Beam Induced Deposition of Iron. Masters Thesis, Eindhoven University of Technology (The Netherlands), 2009.
14. T P, R. K.; Unlu, I.; Barth, S.; Ingólfsson, O.; Fairbrother, D. H., Electron Induced Surface Reactions of HFeCo3(CO)12, a Bimetallic Precursor for Focused Electron Beam Induced Deposition (FEBID). *The Journal of Physical Chemistry C* **2018,** *122* (5), 2648-2660.
15. Porrati, F.; Pohlit, M.; Müller, J.; Barth, S.; Biegger, F.; Gspan, C.; Plank, H.; Huth, M., Direct writing of CoFe alloy nanostructures by focused electron beam induced deposition from a heteronuclear precursor. *Nanotechnology* **2015,** *26* (47), 475701.
16. P, R. K. T.; Weirich, P.; Hrachowina, L.; Hanefeld, M.; Bjornsson, R.; Hrodmarsson, H. R.; Barth, S.; Fairbrother, D. H.; Huth, M.; Ingólfsson, O., Electron interactions with the heteronuclear carbonyl precursor H2FeRu3(CO)13 and comparison with HFeCo3(CO)12: from fundamental gas phase and surface science studies to focused electron beam induced deposition. *Beilstein Journal of Nanotechnology* **2018,** *9*, 555-579.
17. Rosenberg, S. G.; Barclay, M.; Fairbrother, D. H., Electron induced reactions of surface adsorbed tungsten hexacarbonyl (W(CO)6). *Physical Chemistry Chemical Physics* **2013,** *15* (11), 4002-4015.
18. Wnuk, J. D.; Gorham, J. M.; Rosenberg, S. G.; van Dorp, W. F.; Madey, T. E.; Hagen, C. W.; Fairbrother, D. H., Electron Induced Surface Reactions of the Organometallic Precursor Trimethyl(methylcyclopentadienyl)platinum(IV). *The Journal of Physical Chemistry C* **2009,** *113* (6), 2487-2496.
19. Carden, W. G.; Lu, H.; Spencer, J. A.; Fairbrother, D. H.; McElwee-White, L., Mechanism-based design of precursors for focused electron beam-induced deposition. *MRS Communications* **2018,** *8* (2), 343-357.
20. Rosenberg, S. G.; Barclay, M.; Fairbrother, D. H., Electron Beam Induced Reactions of Adsorbed Cobalt Tricarbonyl Nitrosyl (Co(CO)3NO) Molecules. *The Journal of Physical Chemistry C* **2013,** *117* (31), 16053-16064.
21. Spencer, J. A.; Brannaka, J. A.; Barclay, M.; McElwee-White, L.; Fairbrother, D. H., Electron-Induced Surface Reactions of η3-Allyl Ruthenium Tricarbonyl Bromide [(η3-C3H5)Ru(CO)3Br]: Contrasting the Behavior of Different Ligands. *The Journal of Physical Chemistry C* **2015,** *119* (27), 15349-15359.
22. Muthukumar, K.; Jeschke, H. O.; Valentí, R.; Begun, E.; Schwenk, J.; Porrati, F.; Huth, M., Spontaneous dissociation of Co(2)(CO)(8) and autocatalytic growth of Co on SiO(2): A combined experimental and theoretical investigation. *Beilstein journal of nanotechnology* **2012,** *3*, 546-555.
23. Barber, M.; Connor, J. A.; Derrick, L. M. R.; Hall, M. B.; Hillier, I. H., High energy photoelectron spectroscopy of transition metal complexes. Part 2.—Metallocenes. *Journal of the Chemical Society, Faraday Transactions 2: Molecular and Chemical Physics* **1973,** *69* (0), 559-562.
24. Plummer, E. W.; Salaneck, W. R.; Miller, J. S., Photoelectron spectra of transition-metal carbonyl complexes: comparison with the spectra of adsorbed CO. *Physical Review B* **1978,** *18* (4), 1673-1701.

25. Díaz, J.; Paolicelli, G.; Salvador, F.; Comin, F., *Separation of the sp3 and sp2 components in the C1s photoemission spectra of amorphous carbon films*. 1996; Vol. 54, p 8064-8069.
26. Barlow, A. J.; Popescu, S.; Artyushkova, K.; Scott, O.; Sano, N.; Hedley, J.; Cumpson, P. J., Chemically specific identification of carbon in XPS imaging using Multivariate Auger Feature Imaging (MAFI). *Carbon* **2016,** *107*, 190-197.
27. Lascovich, J. C.; Giorgi, R.; Scaglione, S., Evaluation of the sp2/sp3 ratio in amorphous carbon structure by XPS and XAES. *Applied Surface Science* **1991,** *47* (1), 17-21.
28. Filik, J.; May, P. W.; Pearce, S. R. J.; Wild, R. K.; Hallam, K. R., XPS and laser Raman analysis of hydrogenated amorphous carbon films. *Diamond and Related Materials* **2003,** *12* (3), 974-978.
29. Landheer, K.; Rosenberg, S. G.; Bernau, L.; Swiderek, P.; Utke, I.; Hagen, C. W.; Fairbrother, D. H., Low-Energy Electron-Induced Decomposition and Reactions of Adsorbed Tetrakis(trifluorophosphine)platinum [Pt(PF3)4]. *The Journal of Physical Chemistry C* **2011,** *115* (35), 17452-17463.
30. Rosenberg, S. G.; Landheer, K.; Hagen, C. W.; Fairbrother, D. H., Substrate temperature and electron fluence effects on metallic films created by electron beam induced deposition. *Journal of Vacuum Science & Technology B* **2012,** *30* (5), 051805.
31. Henderson, M. A.; Ramsier, R. D.; Yates, J. T., Low-energy electron induced decomposition of Fe(CO)5 adsorbed on Ag(111). *Surface Science* **1991,** *259* (1), 173-182.
32. Suzuki, S.; Yanagihara, K.; Hirokawa, K., XPS study of oxides formed on the surface of high-purity iron exposed to air. *Surface and Interface Analysis* **2000,** *30* (1), 372-376.
33. Sanz-Hernández, D.; Fernández-Pacheco, A., Modelling focused electron beam induced deposition beyond Langmuir adsorption. *Beilstein journal of nanotechnology* **2017,** *8*, 2151-2161.

1722 N Calvert St.
Baltimore, MD 21202

Michael Barclay

(303) 669-2647
MSB91880@gmail.com

Summary

- Extensive technical knowledge and training with many devices, instruments, and software programs.
- Highly skilled at instrument fabrication, design, calibration, and maintenance.
- Excels at technical and scientific problem solving / troubleshooting.
- Skilled at learning new concepts quickly, working under pressure, and original thinking.
- Experienced working independently or in groups. Experienced with international research collaborations.
- Hard worker with an exceptional drive toward comprehensive knowledge and understanding.

Education

Ph.D. Chemistry Degree *Expected 2019*
Johns Hopkins University, *Baltimore, MD*
Advisor: *Dr. D. Howard Fairbrother*

- Dissertation Title: *A study on low pressure carbonaceous film growth via Extreme Ultraviolet (EUV) and Electron Beam Induced Deposition (EBID).* **GPA: 4.0**

M.A. Chemistry Degree *2013*
Johns Hopkins University, *Baltimore, MD*
Advisor: *Dr. D. Howard Fairbrother*

- Relevant Coursework: UHV System Construction and Design, Surface Analytical Techniques, Solid State Physics, Intermediate Quantum Mechanics, Chemical Kinetics, and Electrical / Optical / Magnetic Properties of Materials. **GPA: 3.50**

B.S. Chemistry Degree in Biochemistry / Biophysics *2009*
Creighton University, *Omaha, NE*

- Relevant Coursework: Nucleic Acids, Thermodynamics, Quantum Mechanics, and Particle Physics and General Relativity.

Career History & Accomplishments

National Institute of Standards and Technology (NIST), *Guest Researcher* *2013-2018*

- Collaborated with the Ultraviolet Physics Group of the Sensor Science Division at NIST to study EUV-induced carbon deposits made using the Synchrotron Ultraviolet Radiation Facility (SURF III).
- Gained experience with Single Wavelength / Spectroscopic Ellipsometry, Principle Component Analysis, and X-ray Photoelectron Spectroscopy Mapping. Constructed simple spin coating apparatus and brief experience using an experimental Extreme Ultraviolet Lithography tool.

Johns Hopkins University Surface Analytical Lab, *Lab Technician* *2011-Present*

- Provided X-ray / Ultraviolet Photoelectron Spectroscopy (XPS / UPS) and Auger Electron Spectroscopy (AES) analytical services and consulted for over a dozen research labs (on and off campus) and several corporations.
- Provided technical support, maintained, operated, and upgraded surface analytical instruments for the Materials Science Department at Johns Hopkins University

Johns Hopkins University, *Research Assistant***, Advisor:** *Dr. D. Howard Fairbrother* *2010-Present*

- Thesis Topic: *Analysis of thin film growth on Ru-capped Multilayer Mirrors via Extreme Ultraviolet Light (EUV) and Electron Beam (EB) Lithography.*
- Applied surface analytical techniques to the study of surface deposited carbon via EUV / EB radiation. Also designed, built, maintained, and improved several custom UHV apparatuses for aforementioned analyses using limited funds.
- Gained extensive experience using multiple surface analytical techniques including XPS / UPS, AES, Atomic Force Microscopy (AFM), Secondary Electron Microscopy (SEM), Energy-dispersive X-ray spectroscopy (EDS / EDX), Mass Spectrometry (MS), and Fourier Transform Infrared Spectroscopy (FTIR).

Creighton University Biochemistry Lab, *Technician / Research Assistant* *2008-2010*

- Research Topic: *Structural Studies of the Guanine Riboswitch*.
- Cultivated and prepared RNA Riboswitches for crystallography. Obtained X-ray Crystallography data to determine RNA structure.
- Optimized and refined the procedure for the growth of DNA plasmids and their transcription.

Creighton University Department of Information Technology, *Technician* *2008-2009*

- Provided technological support both student and university owned electronic devices. Repaired both hardware and software problems for a universal range of devices including cell phones, computers, and university servers. Also provided in-depth training for new personnel.
- Played a major role in revolutionizing and streamlining the customer computer repair queue. Also aided in modifying personnel training to produce more skilled technicians.

Publications

1. Koch, S.; Kaiser, C. D.; Penner, P.; Barclay, M.; Frommeyer, L.; Emmrich, D.; Stohmann, P.; Abu-Husein, T.; Terfort, A.; Fairbrother, D. H.; Ingólfsson, O.; Gölzhäuser, A., Amplified cross-linking efficiency of self-assembled monolayers through targeted dissociative electron attachment for the production of carbon nanomembranes. *Beilstein Journal of Nanotechnology* **2017,** *8*, 2562-2571
2. Spencer, J. A.; Barclay, M.; Gallagher, M. J.; Winkler, R.; Unlu, I.; Wu, Y.-C.; Plank, H.; McElwee-White, L.; Fairbrother, D. H. *Beilstein Journal of Nanotechnology* **2017**, 8, 2410–2424. doi:10.3762/bjnano.8.240
3. David Raciti, Joseph Kubal, Cheng Ma, Michael Barclay, Matthew Gonzalez, Miaofang Chi, Jeffrey Greeley, Karren L. More, Chao Wang, "Pt_3Re alloy nanoparticles as electrocatalysts for the oxygen reduction reaction", *Nano Energy*, **2016**, 20, pp 202
4. Shi, W.; Li, J.; Polsen, E. S.; Oliver, C. R.; Zhao, Y.; Meshot, E. R.; Barclay, M.; Fairbrother, D. H.; Hart, A. J.; Plata, D. L., Oxygen-promoted catalyst sintering influences number density, alignment, and wall number of vertically aligned carbon nanotubes. *Nanoscale* **2017,** *9* (16), 5222-5233
5. Julie A. Spencer, Joseph A. Brannaka, Michael Barclay, Lisa McElwee-White, and D. Howard Fairbrother, "Electron-Induced Surface Reactions of η3-Allyl Ruthenium Tricarbonyl Bromide [$(\eta3\text{-}C_3H_5)Ru(CO)_3Br$]: Contrasting the Behavior of Different Ligands", *J. Phys. Chem. C*, **2015**, 119 (27), pp 15349–15359
6. Samantha G. Rosenberg, Michael Barclay, and D. Howard Fairbrother, "Electron Induced Surface Reactions of Organometallic Metal$(hfac)_2$ Precursors and Deposit Purification", *ACS Appl. Mater. Interfaces*, **2014**, 6 (11), pp 8590–8601
7. Julie A. Spencer, Samantha G. Rosenberg, Michael Barclay, Yung-Chien Wu, Lisa McElwee White, D. Howard Fairbrother, "Understanding the electron-stimulated surface reactions of organometallic complexes to enable design of precursors for electron beam-induced deposition", *Applied Physics A*, **2014**, 117 (4), pp 1631-1644
8. Samantha G. Rosenberg, Michael Barclay, and D. Howard Fairbrother, "Electron induced reactions of surface adsorbed tungsten hexacarbonyl ($W(CO)_6$)", *Phys. Chem. Chem. Phys.*, **2013**, 15, pp 4002- 4015
9. Samantha G. Rosenberg, Michael Barclay, and D. Howard Fairbrother, "Electron Beam Induced Reactions of Adsorbed Cobalt Tricarbonyl Nitrosyl ($Co(CO)_3NO$) Molecules", *J. Phys. Chem. C*, **2013**, 117 (31), pp 16053–16064

Presentations

1. Michael Barclay, N.S. Faradzhev, S.B. Hill, T.B. Lucatorto, D.H. Fairbrother, "Comparison of Carbonaceous Thin Films Deposited on Ru-capped Multilayer Mirrors via Extreme-Ultraviolet Light and Electrons", AVS 61st International Symposium, Baltimore, MD, United States, Nov 13, **2014**

Awards & Scholarships

- Ernest M. Marks Fellowship
- Charles and Mary Heider Scholarship
- Jesuit High School Scholarship
- Ignatian Leadership and Service Scholarship
- Trondel-Zenner, Margaret Scholarship
- Wiesner Family Scholarship
- Ahmanson Foundation Scholarship
- Jesuit Higher Education Scholarship

Memberships & Affiliations

- Member, American Vacuum Society
- Member, National Chemistry Society
- Member, National Society of Collegiate Scholars